

**Quantum transport in superconducting hybrids  
Molecular devices and layered materials**

Island, Joshua

**DOI**

[10.4233/uuid:257795db-f94a-421e-80ab-fae7b8c17d4d](https://doi.org/10.4233/uuid:257795db-f94a-421e-80ab-fae7b8c17d4d)

**Publication date**

2016

**Document Version**

Final published version

**Citation (APA)**

Island, J. (2016). *Quantum transport in superconducting hybrids: Molecular devices and layered materials*. [Dissertation (TU Delft), Delft University of Technology]. <https://doi.org/10.4233/uuid:257795db-f94a-421e-80ab-fae7b8c17d4d>

**Important note**

To cite this publication, please use the final published version (if applicable).  
Please check the document version above.

**Copyright**

Other than for strictly personal use, it is not permitted to download, forward or distribute the text or part of it, without the consent of the author(s) and/or copyright holder(s), unless the work is under an open content license such as Creative Commons.

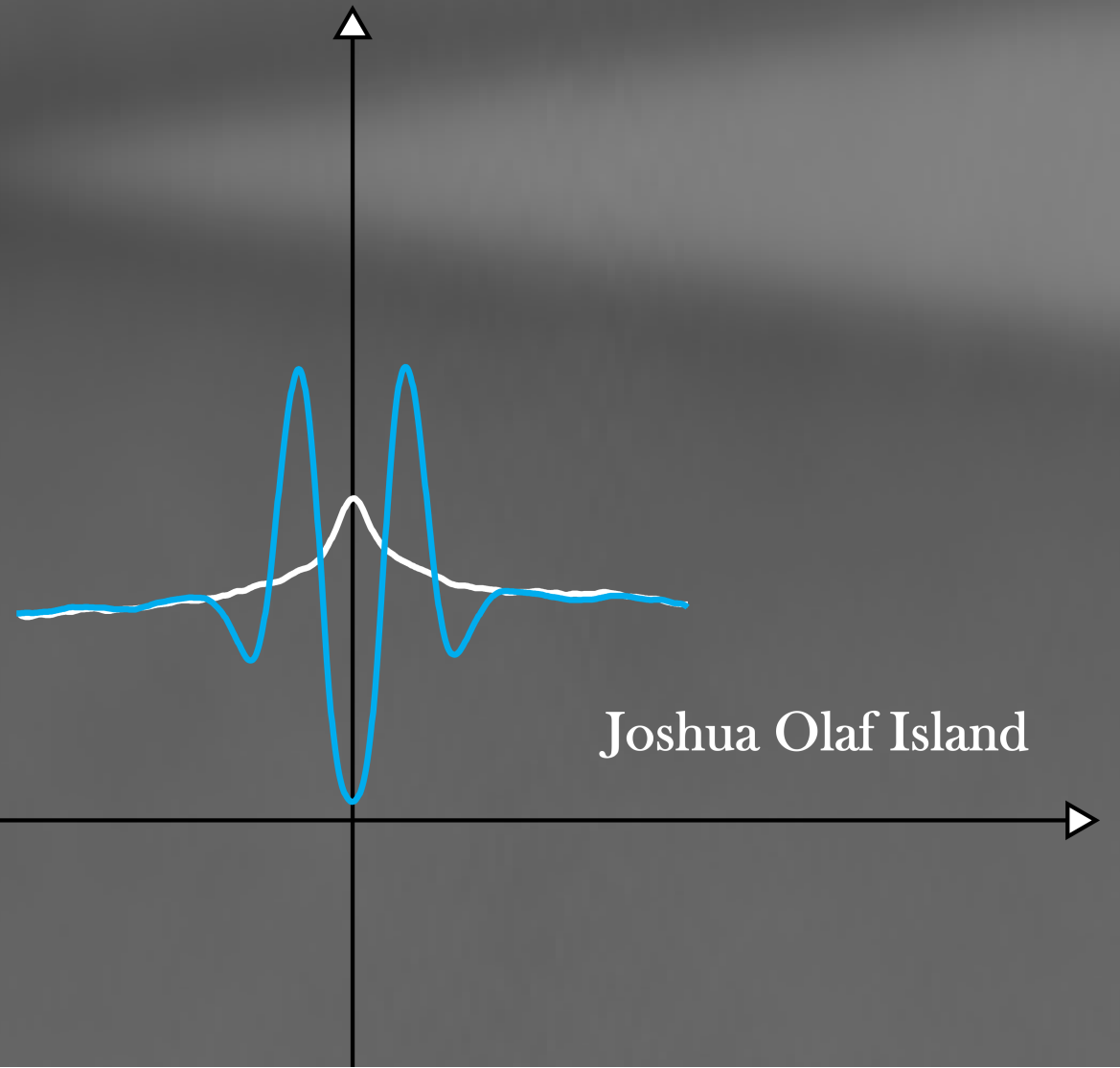
**Takedown policy**

Please contact us and provide details if you believe this document breaches copyrights.  
We will remove access to the work immediately and investigate your claim.

# Quantum Transport in Superconducting Hybrids: Molecular Devices and Layered Materials

Quantum Transport in Superconducting Hybrids

Joshua Olaf Island



# **QUANTUM TRANSPORT IN SUPERCONDUCTING HYBRIDS**

MOLECULAR DEVICES AND LAYERED MATERIALS



# **QUANTUM TRANSPORT IN SUPERCONDUCTING HYBRIDS**

MOLECULAR DEVICES AND LAYERED MATERIALS

## **Proefschrift**

ter verkrijging van de graad van doctor  
aan de Technische Universiteit Delft,  
op gezag van de Rector Magnificus prof. ir. K.C.A.M. Luyben,  
voorzitter van het College voor Promoties,  
in het openbaar te verdedigen op  
maandag 12 september 2016 om 12:30 uur

door

**Joshua Olaf ISLAND**

Master of Science in Physics, Concordia University, Montreal, Quebec, Canada  
geboren te Oregon, USA.

This dissertation has been approved by the

promotor: prof. dr. ir. H. S. J. van der Zant

Composition of the doctoral committee:

Rector Magnificus, Prof. dr. ir. H. S. J. van der Zant,	voorzitter Delft University of Technology
--	--

Independent members:

Prof. dr. Yaroslav M. Blanter,	Delft University of Technology
Prof. dr. Alexandre Champagne,	Concordia University
Prof. dr. ir. Teun M. Klapwijk,	Delft University of Technology
Prof. dr. Jens Paaske,	University of Copenhagen
Prof. dr. Jose Ignacio Pascual,	CIC nanoGUNE
Dr. Gary A. Steele	Delft University of Technology



*Keywords:* Hybrid devices, quantum dots, two-dimensional materials, layered materials, few-layer graphene break-junctions, Yu-Shiba-Rusinov states, MoS<sub>2</sub>, TaS<sub>2</sub>, superconductivity, Josephson junction.

*Printed by:* Gildeprint - Enschede

*Front & Back:* Grey-scale color-plot of the magnetic field dependence of a hybrid superconducting molecular junction. Front cover shows line-cuts in the superconducting state (blue line) and the normal state (white line).

Copyright © 2016 by J.O. Island. All rights reserved.

Casimir PhD Series, Delft-Leiden 2016-25

ISBN 978-90-8593-269-7

An electronic version of this dissertation is available at  
<http://repository.tudelft.nl/>.

For my Pop, the Icelandic Viking.





# CONTENTS

<b>1</b>	<b>Introduction</b>	<b>1</b>
1.1	The birth of the hybrid superconducting device . . . . .	1
1.2	Recent interest in hybrid devices . . . . .	2
1.3	Molecular electronics and the hybrid molecular device . . . . .	3
1.4	Two-dimensional layered materials . . . . .	6
1.5	Organization of this thesis . . . . .	7
	References . . . . .	8
<b>2</b>	<b>Superconducting proximity effect and the Josephson quantum dot</b>	<b>17</b>
2.1	The Josephson and proximity effects . . . . .	18
2.2	Bogoliubov-de Gennes equation . . . . .	19
2.3	Andreev reflection . . . . .	20
2.4	Multiple Andreev reflections . . . . .	22
2.5	The Diffusive Regime . . . . .	23
2.5.1	Parameterization. . . . .	25
2.6	The Josephson quantum dot . . . . .	27
2.6.1	Superconducting atomic limit . . . . .	28
2.6.2	The large U limit and a single classical spin . . . . .	30
	References . . . . .	32
<b>3</b>	<b>Fabrication of hybrid molecular devices using multi-layer graphene break-junctions</b>	<b>37</b>
3.1	Introduction . . . . .	38
3.2	Fabrication . . . . .	38
3.3	Results . . . . .	39
3.4	Obstacles and outlook . . . . .	47
3.5	Appendix . . . . .	47
3.5.1	Contrast profiles for a typical MLG flake . . . . .	47
3.5.2	Finite elements calculation using COMSOL . . . . .	49
	References . . . . .	50
<b>4</b>	<b>Superconducting molybdenum-rhenium electrodes for single-molecule transport studies</b>	<b>55</b>
4.1	Introduction . . . . .	56
4.2	Fabrication . . . . .	56
4.3	Conclusion . . . . .	61
4.4	Appendix . . . . .	61
4.4.1	Electromigration current-voltage characteristics and three terminal measurements . . . . .	61

4.4.2	Temperature and magnetic field dependence for a second characteristic device . . . . .	62
4.4.3	Estimation of the charging energy $U$ and electrode coupling constant $\Gamma$ . . . . .	62
	References . . . . .	65
<b>5</b>	<b>Proximity-induced Shiba states in a molecular junction</b>	<b>69</b>
5.1	Introduction . . . . .	70
5.2	Device design . . . . .	72
5.3	The normal state . . . . .	73
5.4	The superconducting state . . . . .	73
5.5	Ground state spectroscopy in the superconducting state . . . . .	76
5.6	Conclusion . . . . .	78
5.7	Appendix . . . . .	78
5.7.1	Low temperature characteristics of empty gaps . . . . .	78
5.7.2	Device overview . . . . .	79
5.7.3	Gate dependence . . . . .	79
5.7.4	Temperature dependence of the anomalous zero-bias peaks . . . . .	79
	References . . . . .	82
<b>6</b>	<b>Thickness dependent interlayer transport in vertical MoS<sub>2</sub> Josephson junctions</b>	<b>87</b>
6.1	Introduction . . . . .	88
6.2	Single-layer MoS <sub>2</sub> Josephson Junctions . . . . .	89
6.3	Thickness dependence . . . . .	90
6.4	Conclusion . . . . .	93
6.5	Appendix . . . . .	94
6.5.1	Photoluminescence (PL) and atomic force microscopy (AFM) determination of flake thickness . . . . .	94
6.5.2	Magnetic field dependence of the critical current . . . . .	94
6.5.3	Critical current densities and $I_c R_n$ products as a function of layer number . . . . .	94
	References . . . . .	98
<b>7</b>	<b>Enhanced superconductivity in atomically-thin TaS<sub>2</sub></b>	<b>103</b>
7.1	Introduction . . . . .	104
7.2	Growth and Fabrication . . . . .	105
7.3	Low temperature characterization of $T_c$ and $B_{c2}$ . . . . .	107
7.4	Thickness dependence . . . . .	109
7.5	Appendix . . . . .	113
7.5.1	Optical characterization of 2H-TaS <sub>2</sub> flakes . . . . .	113
7.5.2	Raman spectroscopy of 2H-TaS <sub>2</sub> . . . . .	115
7.5.3	Thinnest device measured . . . . .	116
7.5.4	Berezinskii–Kosterlitz–Thouless (BKT) fits to selected devices . . . . .	118
7.5.5	Residual resistance ratio vs. thickness . . . . .	120
7.5.6	Charge density wave (CDW) considerations in 2H-TaS <sub>2</sub> . . . . .	120
7.5.7	DFT band structure and tight-binding model . . . . .	120

---

7.5.8 Anderson-Morel model . . . . .	123
References . . . . .	126
<b>8 Conclusion</b>	<b>133</b>
8.1 Improvements and Outlook . . . . .	133
References . . . . .	137
<b>Summary</b>	<b>139</b>
<b>Samenvatting</b>	<b>143</b>
<b>Acknowledgments</b>	<b>147</b>
<b>Curriculum Vitae</b>	<b>151</b>
<b>List of Publications</b>	<b>153</b>



# 1

## INTRODUCTION

### 1.1. THE BIRTH OF THE HYBRID SUPERCONDUCTING DEVICE

ADVANCES in device fabrication techniques and the growth and isolation of novel materials have strongly driven recent studies of hybrid superconducting devices in which semiconductors or quantum-dots (QD) are contacted by bulk superconducting electrodes. However, combining superconductors with semiconductors to make a hybrid device finds its roots much earlier and was initially born out of the shortcomings of the basic elements of Josephson computer technology<sup>1</sup>. Following the experimental observation of the DC Josephson effect in 1963[3], IBM and a number of other laboratories started research on Josephson devices for logical circuits. The attraction of superconducting elements for a computer laid in the inherently fast switching (from the superconducting to normal state) speeds of a Josephson junction and the low dissipation of a superconducting circuit. IBM eventually dropped the research project in 1983 as progress in complimentary metal-oxide-semiconductor (CMOS) technology developed rapidly[4]. The research team cited delays in developing a high speed memory chip that would, in principle, only marginally outperform the rapidly progressing semiconductor competition. Glaring drawbacks were also becoming apparent as the need for cryogenic temperatures and the inability of the basic element, the two terminal Josephson junction, to produce a gain also required attention<sup>2</sup>. While the feasibility of a working Josephson computer diminished, several research laboratories continued work in the general direction of superconducting logic elements. The three terminal Josephson junction was born out of these advances[6]. Figure 1.1(a) shows one of the first proposals by Clark et al.[7] in 1980 of a hybrid Josephson field-effect device in which the weak-link is created by an indium arsenide (InAs) (or indium antimonide, InSb) inversion layer. Experimental observation of a gate tunable critical current in such a device was later realized in 1985 by Takayanago et al. [8]. Figure 1.1(b) shows the data reported by Takayanago et

---

<sup>1</sup>For an introduction to proposals of the Josephson computer see overviews by Anacker[1] and Hayakawa[2].

<sup>2</sup>See Klapwijk and Ryabchun for a concise account of the experimental development of hybrid devices through this time period[5].

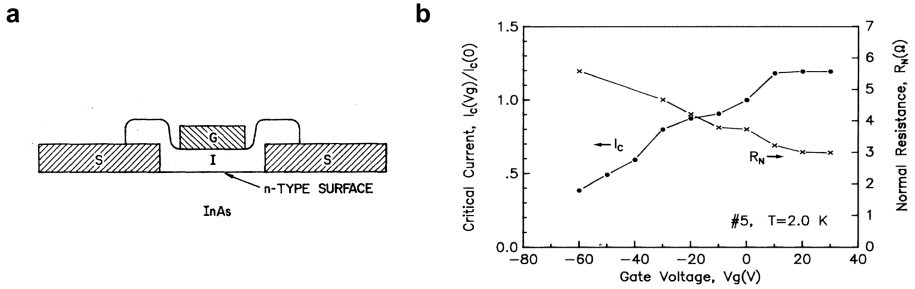


Figure 1.1: (a) One of the first proposals for a hybrid Josephson field effect device by Clark et al.[7] in 1980. Figure adapted from [6]. (b) Experimental realization of a gate tunable supercurrent based on the proposal in (a). Figure adapted from [8].

al. where the critical current and normal state resistance is plotted as a function of gate voltage. The invariance of the characteristic voltage (the  $I_c R_n$  product) of the Josephson junction can be appreciated. The essential ingredient in the fabrication of a hybrid device is the careful handling of the Schottky barrier that forms at the interface between a metal and a semiconductor. The InAs inversion layer was an ideal initial choice as Ohmic contact could be made to the conducting channel.

## 1.2. RECENT INTEREST IN HYBRID DEVICES

These types of devices spawned a great many iterations of hybrid Josephson junctions throughout the years in which the supercurrent through the junction could be tuned with a back gate. Other than the observation of a gate tunable critical current, these devices, although being perhaps more feasible elements of a Josephson computer, lacked a certain amount of fundamental appeal as the observation of supercurrent through a normal metal weak link is quite a robust feature. In fact, with the growth and isolation of novel materials (and molecules) such as carbon nanotubes, graphene,  $C_{60}$ , DNA, and various nanowires, have come many examples of tunable Josephson junctions but with different material weak links[9–14]. Even so, several recent notable experiments in hybrid devices can be differentiated from simple gate tunable weak links. In particular, ballistic supercurrent in graphene Josephson junctions[15–17], topological insulator weak links[18–21], and supercurrent carried by quantum hall edge states[22] have garnered recent attention.

Advances in clean room technology have also spurred research interests in hybrid devices in which the weak link is a zero dimensional QD. In zero-dimensional hybrid devices, portions of a nanotube or nanowire and more recently molecules are contacted with superconducting electrodes[14, 23–30]. These systems have gained interest because of access to the fundamental states (Andreev bound states) which are responsible for the general proximity effect observed in all iterations of hybrid devices.

The ground state of the coupled system of a quantum dot with superconducting electrodes is determined by an interesting competition between Coulomb charging ( $U$ ),

Cooper pairing ( $\Delta$ ), and Kondo screening ( $T_k$ ). For weak Coulomb interaction (relative to the other energies), the ground state of the system favors a BCS-like singlet superposition state of doubly occupied and unoccupied quantum dot levels. In this ground state, excitations are given by Andreev bound states. This regime has been studied in detail in carbon nanotube[24–26] and nanowire[29, 30] devices where the tunnel barriers and charging energy can be tuned weakly enough to allow the BCS-like superposition ground state.

For large charging energy however, the doublet becomes the energetically favored ground state (at temperatures above  $T_k$ ) and a competition between Kondo screening and Cooper pairing sets in (at temperatures below  $T_k$ ). This regime can also be achieved in carbon nanotube and nanowire devices with moderate charging energies by manually tuning the charge state of the quantum dot to an odd occupation and therefore actively favoring the doublet ground state[31–34]. Interestingly, Cooper pairs that pass through a junction in the doublet ground state gain a  $\pi$  phase shift which results in a negative supercurrent[35]. Depending on the relative energies of the two competing many body effects the final ground state of the coupled system at temperatures below  $T_k$  is either a Kondo-like singlet for strong screening ( $T_k > \Delta$ ) or a doublet for weak screening ( $T_k < \Delta$ ). Excitations of these ground states are given by Yu-Shiba-Rusinov (Shiba) bound states which are the central focus of this thesis. Shiba bound states were first experimentally realized in scanning tunneling microscope (STM) experiments on magnetic adatoms adsorbed on Nb[36] and have since been observed in nanotube and nanowire devices tuned to the odd occupation charge state[31–34]. Further STM studies of molecules adsorbed on a superconducting substrate have offered probing of the doublet and singlet ground states[37, 38].

### 1.3. MOLECULAR ELECTRONICS AND THE HYBRID MOLECULAR DEVICE

Molecular electronics has experienced great progress in the last few decades with the invention of the STM which can address single molecules and the realization of nanometer spaced electrodes in the form of electromigrated gold nanowires and mechanically controlled break-junctions (MCBJ). In the early 1970s Aviram and Ratner proposed the use of a single molecule as an electronic rectifier diode[39]. This essentially gave birth to the field of molecular electronics in which single molecules are the functional elements of a circuit. The attraction of using single molecules as active elements stems from the continued miniaturization of electrical components and the diverse functionality offered by molecular devices through careful chemical engineering. It took many years for the experimental ability to trap a single molecule between electrodes to catch up with the initial proposal and it was not until 2005 when the first molecular diode was experimentally realized in a MCBJ experiment[40]. Several examples of molecular diodes have since appeared and an important distinction can be made between devices in which the molecule possesses an intrinsic diode behavior[40–43] (chemically engineered donor-acceptor molecules) and devices which present diode characteristics due to an extrinsic effect[44–47] (bonding asymmetries, quantum interference, environmental control). This distinction points to the basic but growing understanding of the molecular device

which is extremely sensitive to the configuration of a molecule in a junction, the bonding between the molecule and the electrode, and environmental effects on the electronic properties of the junction.

STM and MCBJ experiments based on statistics (averaging electrical measurements of several junctions) act to alleviate some of the experimental discrepancies that appear in molecule experiments due to the large variations in molecule configurations within a junction. In addition to this, these experiments can also provide information about the chemical bond that is made between a molecule and a gold electrode by varying the anchoring groups for the same molecule[48]. However, these experiments have their drawbacks as they typically do not include an electrostatic gate electrode which can be used to tune the electronic orbitals of the molecule to investigate the dominant transport mechanism (highest occupied molecular orbital (HOMO) or lowest unoccupied molecular orbital (LUMO) transport, ON or OFF resonant transport). This makes nano-gap formation in gold nanowires and other materials on a fixed substrate an attractive option as a local gate can be easily incorporated. Also, hybrid devices are easier to fabricate because they rely on well established top-down fabrication techniques.

The added complexity in fabricating hybrid molecular devices has kept their exploration to an absolute minimum. Two studies have been performed in which aluminum[14] or lead[49] is directly electromigrated to create a nano-gap to study hybrid molecular devices. This presents several problems however as scarcely little is known about the bonding between a molecule and these superconductors. Additionally, and perhaps most importantly, the electromigration of gold nanowires has had over a decade of development and advances have been made in the form of a self-breaking technique which minimizes the creation of metallic grains. Much research is still needed to assess the prospects of directly electromigrating a superconductor and making contact to a molecule.

A solution to these obstacles presents itself in the exploitation of the proximity effect. Superconducting reservoirs can be placed in close proximity to a nano-gap in gold or another material and through the proximity effect, the superconducting properties of the molecular junction can be studied. This was accomplished using a gold nanowire contacted by aluminum electrodes and it was found that stronger coupling to a  $C_{60}$  molecule could be achieved in proximity gold junctions than in completely aluminum junctions[14]. This is important to enter the regime in which Kondo correlations compete with superconductivity and access to the competing ground state of the coupled system is reached.

This thesis discusses the development of two types of hybrid molecular systems with the aim of investigating the interesting competition between many body physics that occurs in a coupled QD-superconductor system at low temperatures. The first one presents nano-gap formation in multi-layer graphene devices with superconducting electrodes. Nano-gaps can be made in multi-layer graphene flakes which are then used as electrodes to study molecular junctions[50–53]. This offers the advantage of exploring alternative bonding chemistries such as  $\pi$ - $\pi$  stacking of aromatic rings and the advantage that graphene provides a more stable alternative to the gold-molecule junction for room temperature operation. More interestingly however, superconducting metals can be deposited on the flake and by proximity effect hybrid molecular devices can be studied. An artistic representation of such a device is shown in Figure 1.2(a). Superconducting elec-



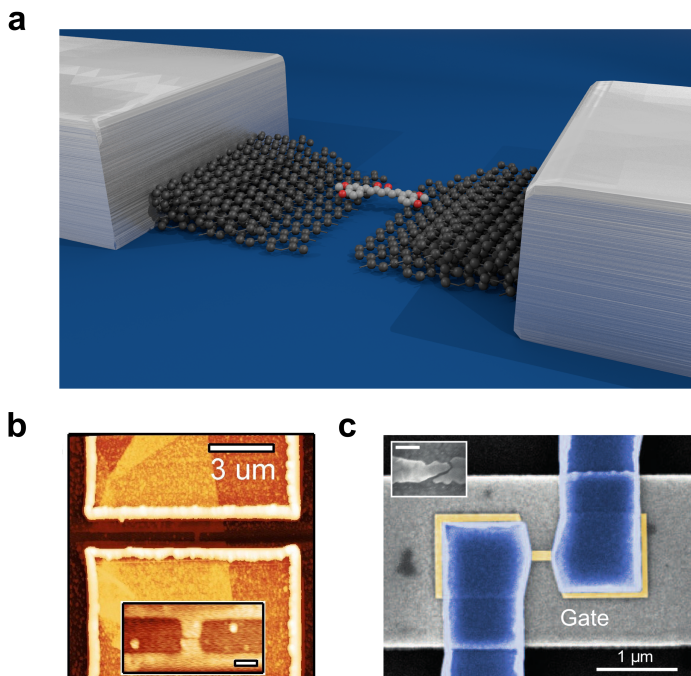


Figure 1.2: **Superconducting hybrid molecular devices.** (a) Artistic representation of a molecular device in which multi-layer graphene is used as an electrode. (b) Atomic force microscopy image of the hybrid multi-layer graphene device developed in chapter 3. The inset show a zoom of the center of the junction. The scale bar is 100 nm. (c) Scanning electron microscopy image of the hybrid gold device developed in chapter 4. The inset shows a nano-gap formed in the gold nanowire after electromigration.

trodes (grey) are contacted to a few-layer graphene flake. A high current is used to create a nano-gap in the flake (similar to electromigration techniques for gold) and molecules are deposited in the junction. Figure 1.2(b) shows an atomic force microscopy image of such a hybrid device developed in chapter 3 of this thesis. The top and bottom portions of the image show the superconducting electrodes patterned on top of a multi-layer graphene flake. The flake is barely visible between the two electrodes but the inset of Figure 1.2(b) shows a zoom on the center of the junction showing the patterned multi-layer graphene flake with a nano-gap.

The second method builds on over a decade of research in the electromigration and nano-gap formation in gold nanowires to fabricate hybrid molecular devices with superconducting electrodes in close proximity. Figure 1.2(c) shows a false-colored scanning electron microscopy image of a representative hybrid device studied in 4. Molybdenum-rhenium (a superconducting alloy) electrodes (blue) are fabricated on top of a gold nanowire (gold strip between the superconducting electrodes) and a controlled process of electromigration and self-breaking are used to gently create a nano-gap in the gold nanowire.

Using these electrodes, chapter 5 explores hybrid molecular devices incorporating all organic radical molecules in which we observe Shiba state excitations and probe the singlet and doublet ground state of the coupled system.

## 1.4. TWO-DIMENSIONAL LAYERED MATERIALS

The isolation of graphene from graphite[54] has brought about a tremendous research effort on the general class of layered materials which can be exfoliated and manipulated using scotch tape and polymer substrates. Mentioned briefly before, graphene has garnered significant attention as a high quality two dimensional system (even more so when placed between two flakes of hexagonal boron nitride[55]) and milestones include observations of the quantum hall effect[56–58], fractional quantum hall effect[59, 60], and a quantum spin Hall state in high magnetic fields[61]. While fundamental studies of the two-dimensional (2D) system have flourished, graphene has lacked direct applicability in next generation electronics due to its semi-metal nature. Several research groups worked to alleviate the drawback of a nonexistent bandgap by either patterning graphene into nanoribbons[62, 63] or by opening a bandgap in bilayer graphene[64–67]. Simultaneously work on other layered materials which can be exfoliated and isolated from bulk material progressed[68, 69]. Born out of the lack of a bandgap in graphene, the transition metal dichalcogenides (TMDC) are perhaps the second most studied layered materials as of late but research directions have moved additionally to the transition metal trichalcogenides[70, 71]. The semiconducting TMDCs have attracted attention for their use as next generation electronics[72, 73] and as the active light absorbing material in a photodetector[74, 75].

The simplicity of mechanical exfoliation and the "scotch-tape method" has brought about a rapid expansion in the research on layered materials and a thorough introduction is beyond the scope of this thesis<sup>3</sup>. However, one intriguing aspect of these materials which we also investigate here is the ability to study thickness dependence and confinement effects with atomic resolution. Mechanical exfoliation allows the isolation of not only single layers but any number of layers desired (provided one has the patience to search for the flakes). This allows fundamental studies of confinement effects on the electronic properties of the materials and collective phases of matter such as superconductivity and charge density waves.

The hallmark examples of thickness dependent studies on layered materials are on molybdenum disulfide (MoS<sub>2</sub>)[80, 81]. It has been shown that the electronic band gap of the material gradually changes with flake thickness. In bulk-like samples an indirect band gap of 1.2 eV exists but as the material is thinned down, the band gap gradually increases until reaching a maximum direct gap of 1.8 eV at the single layer limit. This thickness dependence arises from quantum confinement effects on the hybridization between the  $p_z$  orbitals of the sulfur atoms and the  $d$  orbitals of the molybdenum atoms[80, 81].

Additionally, several TMDCs present collective phases of matter such as superconductivity and charge density wave instabilities. In studies on niobium diselenide (NbSe<sub>2</sub>) it has been shown that a gradual reduction in thickness results in a decrease in the su-

<sup>3</sup>For the interested reader, thorough reviews are available[76–79]

perconducting properties of the material[82–86]. The critical temperature (7 K in bulk) gradually decreases with thickness until reaching a minimum at the single layer limit of 3 K. Earlier studies attribute this decrease to simple degradation effects (the flakes oxidize in ambient conditions) in thinner samples but recent advances in encapsulation (similar to encapsulation of graphene with boron nitride) have permitted studies of superconductivity in pristine (low disorder) single and few-layer samples for which the decrease is attributed to a reduction in interlayer Cooper pair coupling[85]. Another recent example of confinement effects on collective phases is the charge density wave instability in tantalum disulfide ( $\text{TaS}_2$ )[87, 88]. In the 1T crystal phase of  $\text{TaS}_2$ , a nearly commensurate charge density wave (NCCDW) instability occurs at room temperature and a transition to a commensurate charge density wave (CCDW) occurs at 200 K. As the flake thickness is reduced the charge density wave transition becomes suppressed and disappears below 10 nm, roughly coinciding with the out-of-plane periodicity of the CCDW (13-layers, 7.8 nm) [87].

Given the ability to study confinement effects in this interesting class of materials, in this thesis we investigate the thickness dependence of 2H-MoS<sub>2</sub> (chapter 6) and 2H-TaS<sub>2</sub> (chapter 7). In vertical hybrid MoS<sub>2</sub> Josephson junctions, we use the Josephson effect which is uniquely sensitive to the type of weak link between two bulk electrodes to study the thickness dependence of one to four layer MoS<sub>2</sub> devices. We additionally present the thickness dependent superconducting properties of 2H-TaS<sub>2</sub> which has a bulk superconducting transition temperature of 0.6 K. We observe an increase in the superconducting properties of the material with reduced thickness which we attribute to an increase in the effective electron-phonon coupling constant.

## 1.5. ORGANIZATION OF THIS THESIS

This thesis is organized starting with this introduction in chapter 1 and a review of the theoretical background aiding in the interpretation of the experimental results presented in the rest of the thesis.

In chapter 2, we start with a short historical recollection of the Josephson effect and the events that lead to its predication and confirmation. We derive the Bogoliubov de Gennes equations by constructing suitable wavefunctions and calculate the density of states of a homogeneous superconductor. This is followed by a derivation of the probability of Andreev reflection at the interface of a normal metal and a superconductor. Following this, multiple Andreev reflection is discussed which is observed in single and bilayer vertical MoS<sub>2</sub> Josephson junctions in chapter 5. Proximity effect in long junctions is reviewed which is the theoretical handling of the proximity induced density of states that occurs in the gold and few-layer graphene electrodes of the hybrid molecular devices (chapters 3, 4, and 5).

The second half of chapter 2 discusses the system of a quantum dot coupled to superconducting leads. We discuss two extremes of the phase diagram for the quantum dot-superconductor system, namely, the superconducting atomic limit (large superconducting gap) and the large charging energy limit.

In chapter 3 we discuss the first developed hybrid molecular system based on few-layer graphene electrodes. An electroburning process is developed to create a few-nanometer gap in a graphene flake. We estimate the temperatures at which the electroburning pro-

cess starts and develop constrictions to localize the gap and reduce the starting temperatures. At the end of the chapter we realize a working hybrid device using a copper curcuminoid molecule.

In chapter 4 we discuss the second hybrid molecular system based on electromigrated gold nanowires which is then used for the studies in chapter 5. We show the characterization of the empty junctions at low temperatures and present measurements on a  $\text{Fe}_4$  molecule which shows an enhancement of the conductance near the degeneracy point in the superconducting state due to Cooper pair transport.

In chapter 5 we present low temperature measurements of a model spin 1/2 molecule (all organic radical) which exhibits Yu-Shiba-Rusinov excited states. We present calculations of the modified Anderson model to further investigate the results. It is shown that we can access both the Kondo-like singlet and doublet ground states which lead to the doublet and Kondo-like singlet excitations, respectively.

Chapter 6 presents fabrication and experimental measurements on vertical 2H-Mo<sub>2</sub> junctions in which the flake is sandwiched between two molybdenum-rhenium electrodes. These junctions exhibit metallic like transport for the single and bilayer devices but present tunneling like transport for three and four layer devices. A simple model is suggested based on strong hybridization of the flake with the electrodes.

In chapter 7 we study the thickness dependent superconducting properties of 2H-TaS<sub>2</sub>. We find that the critical temperature and critical field increase with decreasing thickness. A possible mechanism for this enhancement is suggested based on calculations of a modified Anderson-Morel model which takes into account a generic density of states. The calculations suggest a renormalization of the bare Coulomb repulsion in atomically thin flakes which leads to (for strong enough bare repulsion) an increase in the effective electron-phonon coupling constant for decreased layer thicknesses.

The last chapter (chapter 8) concludes on these results and provides an outlook for future endeavors.

## REFERENCES

- [1] W. Anacker, *Josephson computer technology: an IBM research project*, IBM Journal of Research and Development **24**, 107 (1980).
- [2] H. Hayakawa, *Josephson computer technology*, Physics Today **39** (1986).
- [3] P. W. Anderson and J. M. Rowell, *Probable observation of the Josephson superconducting tunneling effect*, Physical Review Letters **10**, 230 (1963).
- [4] A. L. Robinson, *IBM drops superconducting computer project problems with a high-speed memory chip would delay a Josephson junction computer long enough for semiconductors to catch up*, Science **222**, 492 (1983).
- [5] T. M. Klapwijk and S. A. Ryabchun, *Direct observation of ballistic Andreev reflection*, Journal of Experimental and Theoretical Physics **119**, 997 (2014).
- [6] W. J. Gallagher, *Three-terminal superconducting devices*, Magnetism, IEEE Transactions on **21**, 709 (1985).

- [7] T. D. Clark, R. J. Prance, and A. D. C. Grassie, *Feasibility of hybrid Josephson field effect transistors*, *Journal of Applied Physics* **51**, 2736 (1980).
- [8] H. Takayanagi and T. Kawakami, *Superconducting proximity effect in the native inversion layer on InAs*, *Physical Review Letters* **54**, 2449 (1985).
- [9] A. Y. Kasumov, M. Kociak, S. Gueron, B. Reulet, V. T. Volkov, D. V. Klinov, and H. Bouchiat, *Proximity-induced superconductivity in DNA*, *Science* **291**, 280 (2001).
- [10] Y.-J. Doh, J. A. van Dam, A. L. Roest, E. P. A. M. Bakkers, L. P. Kouwenhoven, and S. De Franceschi, *Tunable supercurrent through semiconductor nanowires*, *Science* **309**, 272 (2005).
- [11] J. Xiang, A. Vidan, M. Tinkham, R. M. Westervelt, and C. M. Lieber, *Ge/Si nanowire mesoscopic josephson junctions*, *Nature Nanotechnology* **1**, 208 (2006).
- [12] P. Jarillo-Herrero, J. A. Van Dam, and L. P. Kouwenhoven, *Quantum supercurrent transistors in carbon nanotubes*, *Nature* **439**, 953 (2006).
- [13] H. B. Heersche, P. Jarillo-Herrero, J. B. Oostinga, L. M. K. Vandersypen, and A. F. Morpurgo, *Bipolar supercurrent in graphene*, *Nature* **446**, 56 (2007).
- [14] C. B. Winkelmann, N. Roch, W. Wernsdorfer, V. Bouchiat, and F. Balestro, *Superconductivity in a single-C<sub>60</sub> transistor*, *Nature Physics* **5**, 876 (2009).
- [15] N. Mizuno, B. Nielsen, and X. Du, *Ballistic-like supercurrent in suspended graphene Josephson weak links*, *Nature Communications* **4**, 2716 (2013).
- [16] V. E. Calado, S. Goswami, G. Nanda, M. Diez, A. R. Akhmerov, K. Watanabe, T. Taniguchi, T. M. Klapwijk, and L. M. K. Vandersypen, *Ballistic Josephson junctions in edge-contacted graphene*, *Nature Nanotechnology* **10**, 761 (2015).
- [17] M. B. Shalom, M. J. Zhu, V. I. Fal'ko, A. Mishchenko, A. V. Kretinin, K. S. Novoselov, C. R. Woods, K. Watanabe, T. Taniguchi, A. K. Geim, *et al.*, *Quantum oscillations of the critical current and high-field superconducting proximity in ballistic graphene*, *Nature Physics* **12**, 318 (2016).
- [18] I. Knez, R.-R. Du, and G. Sullivan, *Andreev reflection of helical edge modes in InAs/GaSb quantum spin Hall insulator*, *Physical Review Letters* **109**, 186603 (2012).
- [19] S. Hart, H. Ren, T. Wagner, P. Leubner, M. Mühlbauer, C. Brüne, H. Buhmann, L. W. Molenkamp, and A. Yacoby, *Induced superconductivity in the quantum spin Hall edge*, *Nature Physics* **10**, 638 (2014).
- [20] V. S. Pribiag, A. J. A. Beukman, F. Qu, M. C. Cassidy, C. Charpentier, W. Wegscheider, and L. P. Kouwenhoven, *Edge-mode superconductivity in a two-dimensional topological insulator*, *Nature Nanotechnology* **10**, 593 (2015).

- [21] J. Wiedenmann, E. Bocquillon, R. S. Deacon, S. Hartinger, O. Herrmann, T. M. Klapwijk, L. Maier, C. Ames, C. Brüne, C. Gould, *et al.*, *4 $\pi$ -periodic josephson supercurrent in HgTe-based topological josephson junctions*, *Nature Communications* **7**, 10303 (2016).
- [22] F. Amet, C. T. Ke, I. V. Borzenets, J. Wang, K. Watanabe, T. Taniguchi, R. S. Deacon, M. Yamamoto, Y. Bomze, S. Tarucha, *et al.*, *Supercurrent in the quantum Hall regime*, *Science* **352**, 966 (2016).
- [23] D. C. Ralph, C. T. Black, and M. Tinkham, *Spectroscopic measurements of discrete electronic states in single metal particles*, *Physical Review Letters* **74**, 3241 (1995).
- [24] J. D. Pillet, C. H. L. Quay, P. Morfin, C. Bena, A. L. Yeyati, and P. Joyez, *Andreev bound states in supercurrent-carrying carbon nanotubes revealed*, *Nature Physics* **6**, 965 (2010).
- [25] R. S. Deacon, Y. Tanaka, A. Oiwa, R. Sakano, K. Yoshida, K. Shibata, K. Hirakawa, and S. Tarucha, *Tunneling spectroscopy of Andreev energy levels in a quantum dot coupled to a superconductor*, *Physical Review Letters* **104**, 076805 (2010).
- [26] J.-D. Pillet, P. Joyez, M. F. Goffman, *et al.*, *Tunneling spectroscopy of a single quantum dot coupled to a superconductor: From Kondo ridge to Andreev bound states*, *Physical Review B* **88**, 045101 (2013).
- [27] G. Katsaros, P. Spathis, M. Stoffel, F. Fournel, M. Mongillo, V. Bouchiat, F. Lefloch, A. Rastelli, O. G. Schmidt, and S. De Franceschi, *Hybrid superconductor-semiconductor devices made from self-assembled SiGe nanocrystals on silicon*, *Nature Nanotechnology* **5**, 458 (2010).
- [28] S. De Franceschi, L. Kouwenhoven, C. Schönenberger, and W. Wernsdorfer, *Hybrid superconductor-quantum dot devices*, *Nature Nanotechnology* **5**, 703 (2010).
- [29] V. Mourik, K. Zuo, S. M. Frolov, S. R. Plissard, E. P. A. M. Bakkers, and L. P. Kouwenhoven, *Signatures of Majorana fermions in hybrid superconductor-semiconductor nanowire devices*, *Science* **336**, 1003 (2012).
- [30] W. Chang, S. M. Albrecht, T. S. Jespersen, F. Kuemmeth, P. Krogstrup, J. Nygård, and C. M. Marcus, *Hard gap in epitaxial semiconductor-superconductor nanowires*, *Nature Nanotechnology* **10**, 232 (2015).
- [31] E. J. H. Lee, X. Jiang, R. Aguado, G. Katsaros, C. M. Lieber, and S. De Franceschi, *Zero-bias anomaly in a nanowire quantum dot coupled to superconductors*, *Physical Review Letters* **109**, 186802 (2012).
- [32] W. Chang, V. E. Manucharyan, T. S. Jespersen, J. Nygård, and C. M. Marcus, *Tunneling spectroscopy of quasiparticle bound states in a spinful Josephson junction*, *Physical Review Letters* **110**, 217005 (2013).

- [33] B.-K. Kim, Y.-H. Ahn, J.-J. Kim, M.-S. Choi, M.-H. Bae, K. Kang, J. S. Lim, R. López, and N. Kim, *Transport measurement of Andreev bound states in a Kondo-correlated quantum dot*, Physical Review Letters **110**, 076803 (2013).
- [34] A. Kumar, M. Gaim, D. Steininger, A. L. Yeyati, A. Martín-Rodero, A. K. Hüttel, and C. Strunk, *Temperature dependence of Andreev spectra in a superconducting carbon nanotube quantum dot*, Physical Review B **89**, 075428 (2014).
- [35] J. A. Van Dam, Y. V. Nazarov, E. P. A. M. Bakkers, S. De Franceschi, and L. P. Kouwenhoven, *Supercurrent reversal in quantum dots*, Nature **442**, 667 (2006).
- [36] A. Yazdani, B. A. Jones, C. P. Lutz, M. F. Crommie, and D. M. Eigler, *Probing the local effects of magnetic impurities on superconductivity*, Science **275**, 1767 (1997).
- [37] K. J. Franke, G. Schulze, and J. I. Pascual, *Competition of superconducting phenomena and Kondo screening at the nanoscale*, Science **332**, 940 (2011).
- [38] N. Hatter, B. W. Heinrich, M. Ruby, J. I. Pascual, and K. J. Franke, *Magnetic anisotropy in Shiba bound states across a quantum phase transition*, Nature Communications **6**, 8988 (2015).
- [39] A. Aviram and M. A. Ratner, *Molecular rectifiers*, Chemical Physics Letters **29**, 277 (1974).
- [40] M. Elbing, R. Ochs, M. Koentopp, M. Fischer, C. von Hänisch, F. Weigend, F. Evers, H. B. Weber, and M. Mayor, *A single-molecule diode*, Proceedings of the National Academy of Sciences **102**, 8815 (2005).
- [41] J. Hihath, C. Bruot, H. Nakamura, Y. Asai, I. Díez-Pérez, Y. Lee, L. Yu, and N. Tao, *Inelastic transport and low-bias rectification in a single-molecule diode*, ACS Nano **5**, 8331 (2011).
- [42] E. Lortscher, B. Gotsmann, Y. Lee, L. Yu, C. Rettner, and H. Riel, *Transport properties of a single-molecule diode*, ACS Nano **6**, 4931 (2012).
- [43] M. L. Perrin, E. Galán, R. Eelkema, J. M. Thijssen, F. Grozema, and H. S. J. van der Zant, *A gate-tunable single-molecule diode*, Nanoscale **8**, 8919 (2016).
- [44] A. Batra, P. Darancet, Q. Chen, J. S. Meisner, J. R. Widawsky, J. B. Neaton, C. Nuckolls, and L. Venkataraman, *Tuning rectification in single-molecular diodes*, Nano Letters **13**, 6233 (2013).
- [45] T. Kim, Z.-F. Liu, C. Lee, J. B. Neaton, and L. Venkataraman, *Charge transport and rectification in molecular junctions formed with carbon-based electrodes*, Proceedings of the National Academy of Sciences **111**, 10928 (2014).
- [46] A. Batra, J. S. Meisner, P. Darancet, Q. Chen, M. L. Steigerwald, C. Nuckolls, and L. Venkataraman, *Molecular diodes enabled by quantum interference*, Faraday Discussions **174**, 79 (2014).

- [47] B. Capozzi, J. Xia, O. Adak, E. J. Dell, Z.-F. Liu, J. C. Taylor, J. B. Neaton, L. M. Campos, and L. Venkataraman, *Single-molecule diodes with high rectification ratios through environmental control*, *Nature Nanotechnology* **10**, 522 (2015).
- [48] R. Frisenda, M. L. Perrin, H. Valkenier, J. C. Hummelen, and H. S. J. van der Zant, *Statistical analysis of single-molecule breaking traces*, *Physica Status Solidi B* **250**, 2431 (2013).
- [49] K. Luo and Z. Yao, *Fabrication of nanometer-spaced superconducting Pb electrodes*, *Applied Physics Letters* **95**, 113115 (2009).
- [50] F. Prins, A. Barreiro, J. W. Ruitenber, J. S. Seldenthuis, N. Aliaga-Alcalde, L. M. K. Vandersypen, and H. S. J. van der Zant, *Room-temperature gating of molecular junctions using few-layer graphene nanogap electrodes*, *Nano Letters* **11**, 4607 (2011).
- [51] E. Burzurí, F. Prins, and H. S. J. van der Zant, *Characterization of nanometer-spaced few-layer graphene electrodes*, *Graphene* **1**, 26 (2016).
- [52] K. Ullmann, P. B. Coto, S. Leitherer, A. Molina-Ontoria, N. Martín, M. Thoss, and H. B. Weber, *Single-molecule junctions with epitaxial graphene nanoelectrodes*, *Nano Letters* **15**, 3512 (2015).
- [53] E. Burzurí, J. O. Island, R. Díaz-Torres, A. Fursina, A. González-Campo, O. Roubeau, S. J. Teat, N. Aliaga-Alcalde, E. Ruiz, and H. S. J. van der Zant, *Sequential electron transport and vibrational excitations in an organic molecule coupled to few-layer graphene electrodes*, *ACS Nano* **10**, 2521 (2016).
- [54] K. S. Novoselov, A. K. Geim, S. V. Morozov, D. Jiang, Y. Zhang, S. V. Dubonos, I. V. Grigorieva, and A. A. Firsov, *Electric field effect in atomically thin carbon films*, *Science* **306**, 666 (2004).
- [55] C. R. Dean, A. F. Young, I. Meric, C. Lee, L. Wang, S. Sorgenfrei, K. Watanabe, T. Taniguchi, P. Kim, K. L. Shepard, *et al.*, *Boron nitride substrates for high-quality graphene electronics*, *Nature Nanotechnology* **5**, 722 (2010).
- [56] K. S. Novoselov, A. K. Geim, S. V. Morozov, D. Jiang, M. I. Katsnelson, I. V. Grigorieva, S. V. Dubonos, and A. A. Firsov, *Two-dimensional gas of massless Dirac fermions in graphene*, *Nature* **438**, 197 (2005).
- [57] Y. Zhang, Y.-W. Tan, H. L. Stormer, and P. Kim, *Experimental observation of the quantum Hall effect and Berry's phase in graphene*, *Nature* **438**, 201 (2005).
- [58] K. S. Novoselov, Z. Jiang, Y. Zhang, S. V. Morozov, H. L. Stormer, U. Zeitler, J. C. Maan, G. S. Boebinger, P. Kim, and A. K. Geim, *Room-temperature quantum Hall effect in graphene*, *Science* **315**, 1379 (2007).
- [59] K. I. Bolotin, F. Ghahari, M. D. Shulman, H. L. Stormer, and P. Kim, *Observation of the fractional quantum Hall effect in graphene*, *Nature* **462**, 196 (2009).



- [60] X. Du, I. Skachko, F. Duerr, A. Luican, and E. Y. Andrei, *Fractional quantum Hall effect and insulating phase of Dirac electrons in graphene*, *Nature* **462**, 192 (2009).
- [61] A. F. Young, J. D. Sanchez-Yamagishi, B. Hunt, S. H. Choi, K. Watanabe, T. Taniguchi, R. C. Ashoori, and P. Jarillo-Herrero, *Tunable symmetry breaking and helical edge transport in a graphene quantum spin hall state*, *Nature* **505**, 528 (2014).
- [62] Y.-W. Son, M. L. Cohen, and S. G. Louie, *Energy gaps in graphene nanoribbons*, *Physical Review Letters* **97**, 216803 (2006).
- [63] M. Y. Han, B. Özyilmaz, Y. Zhang, and P. Kim, *Energy band-gap engineering of graphene nanoribbons*, *Physical Review Letters* **98**, 206805 (2007).
- [64] T. Ohta, A. Bostwick, T. Seyller, K. Horn, and E. Rotenberg, *Controlling the electronic structure of bilayer graphene*, *Science* **313**, 951 (2006).
- [65] E. V. Castro, K. S. Novoselov, S. V. Morozov, N. M. R. Peres, J. M. B. L. Dos Santos, J. Nilsson, F. Guinea, A. K. Geim, and A. H. C. Neto, *Biased bilayer graphene: semiconductor with a gap tunable by the electric field effect*, *Physical Review Letters* **99**, 216802 (2007).
- [66] J. B. Oostinga, H. B. Heersche, X. Liu, A. F. Morpurgo, and L. M. K. Vandersypen, *Gate-induced insulating state in bilayer graphene devices*, *Nature Materials* **7**, 151 (2008).
- [67] Y. Zhang, T.-T. Tang, C. Girit, Z. Hao, M. C. Martin, A. Zettl, M. F. Crommie, Y. R. Shen, and F. Wang, *Direct observation of a widely tunable bandgap in bilayer graphene*, *Nature* **459**, 820 (2009).
- [68] K. S. Novoselov, D. Jiang, F. Schedin, T. J. Booth, V. V. Khotkevich, S. V. Morozov, and A. K. Geim, *Two-dimensional atomic crystals*, *Proceedings of the National Academy of Sciences* **102**, 10451 (2005).
- [69] A. Ayari, E. Cobas, O. Ogundadegbe, and M. S. Fuhrer, *Realization and electrical characterization of ultrathin crystals of layered transition-metal dichalcogenides*, *Journal of Applied Physics* **101**, 14507 (2007).
- [70] A. Lipatov, P. M. Wilson, M. Shekhirev, J. D. Teeter, R. Netusil, and A. Sinitskii, *Few-layered titanium trisulfide ( $TiS_3$ ) field-effect transistors*, *Nanoscale* **7**, 12291 (2015).
- [71] J. O. Island, M. Barawi, R. Biele, A. Almazán, J. M. Clamagirand, J. R. Ares, C. Sánchez, H. S. J. van der Zant, J. V. Álvarez, R. D'Agosta, *et al.*,  *$TiS_3$  transistors with tailored morphology and electrical properties*, *Advanced Materials* **27**, 2595 (2015).
- [72] B. Radisavljevic, A. Radenovic, J. Brivio, V. Giacometti, and A. Kis, *Single-layer  $MoS_2$  transistors*, *Nature Nanotechnology* **6**, 147 (2011).
- [73] Q. H. Wang, K. Kalantar-Zadeh, A. Kis, J. N. Coleman, and M. S. Strano, *Electronics and optoelectronics of two-dimensional transition metal dichalcogenides*, *Nature Nanotechnology* **7**, 699 (2012).

- [74] Z. Yin, H. Li, H. Li, L. Jiang, Y. Shi, Y. Sun, G. Lu, Q. Zhang, X. Chen, and H. Zhang, *Single-layer MoS<sub>2</sub> phototransistors*, ACS Nano **6**, 74 (2011).
- [75] O. Lopez-Sanchez, D. Lembke, M. Kayci, A. Radenovic, and A. Kis, *Ultrasensitive photodetectors based on monolayer MoS<sub>2</sub>*, Nature Nanotechnology **8**, 497 (2013).
- [76] S. Z. Butler, S. M. Hollen, L. Cao, Y. Cui, J. A. Gupta, H. R. Gutiérrez, T. F. Heinz, S. S. Hong, J. Huang, A. F. Ismach, *et al.*, *Progress, challenges, and opportunities in two-dimensional materials beyond graphene*, ACS Nano **7**, 2898 (2013).
- [77] D. Jariwala, V. K. Sangwan, L. J. Lauhon, T. J. Marks, and M. C. Hersam, *Emerging device applications for semiconducting two-dimensional transition metal dichalcogenides*, ACS Nano **8**, 1102 (2014).
- [78] A. C. Ferrari, F. Bonaccorso, V. Fal'Ko, K. S. Novoselov, S. Roche, P. Bøggild, S. Borini, F. H. Koppens, V. Palermo, N. Pugno, *et al.*, *Science and technology roadmap for graphene, related two-dimensional crystals, and hybrid systems*, Nanoscale **7**, 4598 (2015).
- [79] M. Buscema, J. O. Island, D. J. Groenendijk, S. I. Blanter, G. A. Steele, H. S. J. van der Zant, and A. Castellanos-Gomez, *Photocurrent generation with two-dimensional van der Waals semiconductors*, Chemical Society Reviews **44**, 3691 (2015).
- [80] K. F. Mak, C. Lee, J. Hone, J. Shan, and T. F. Heinz, *Atomically thin MoS<sub>2</sub>: a new direct-gap semiconductor*, Physical Review Letters **105**, 136805 (2010).
- [81] A. Splendiani, L. Sun, Y. Zhang, T. Li, J. Kim, C.-Y. Chim, G. Galli, and F. Wang, *Emerging photoluminescence in monolayer MoS<sub>2</sub>*, Nano Letters **10**, 1271 (2010).
- [82] R. F. Frindt, *Superconductivity in ultrathin NbSe<sub>2</sub> layers*, Physical Review Letters **28**, 299 (1972).
- [83] M. S. El-Bana, D. Wolverson, S. Russo, G. Balakrishnan, D. M. Paul, and S. J. Bending, *Superconductivity in two-dimensional NbSe<sub>2</sub> field effect transistors*, Superconductor Science and Technology **26**, 125020 (2013).
- [84] Y. Cao, A. Mishchenko, G. Yu, E. Khestanova, A. P. Rooney, E. Prestat, A. V. Kretinin, P. Blake, M. B. Shalom, C. Woods, *et al.*, *Quality heterostructures from two-dimensional crystals unstable in air by their assembly in inert atmosphere*, Nano Letters **15**, 4914 (2015).
- [85] X. Xi, Z. Wang, W. Zhao, J.-H. Park, K. T. Law, H. Berger, L. Forró, J. Shan, and K. F. Mak, *Ising pairing in superconducting NbSe<sub>2</sub> atomic layers*, Nature Physics **12**, 139 (2015).
- [86] M. Yoshida, J. Ye, T. Nishizaki, N. Kobayashi, and Y. Iwasa, *Electrostatic and electrochemical tuning of superconductivity in two-dimensional NbSe<sub>2</sub> crystals*, Applied Physics Letters **108**, 202602 (2016).

- [87] Y. Yu, F. Yang, X. F. Lu, Y. J. Yan, Y.-H. Cho, L. Ma, X. Niu, S. Kim, Y.-W. Son, D. Feng, *et al.*, *Gate-tunable phase transitions in thin flakes of 1T-TaS<sub>2</sub>*, *Nature Nanotechnology* **10**, 270 (2015).
- [88] A. W. Tsen, R. Hovden, D. Wang, Y. D. Kim, J. Okamoto, K. A. Spoth, Y. Liu, W. Lu, Y. Sun, J. C. Hone, *et al.*, *Structure and control of charge density waves in two-dimensional 1T-TaS<sub>2</sub>*, *Proceedings of the National Academy of Sciences* **112**, 15054 (2015).



# 2

## SUPERCONDUCTING PROXIMITY EFFECT AND THE JOSEPHSON QUANTUM DOT

*In this chapter we review the theoretical and experimental background which aids in interpreting the results presented throughout this thesis. The chapter begins with a short historical recollection of the Josephson and proximity effects. This is followed by an introduction to the inhomogeneous superconductor which is handled by the Bogoliubov de Gennes equation. We then calculate the probability of Andreev reflection at the interface of a one-dimensional normal metal and a superconductor. Following this, multiple Andreev reflection is discussed. Proximity effect and superconducting correlations in long junctions is reviewed at the end of the first half. The second half of the chapter discusses the system of a quantum dot coupled to superconducting leads. We review the theoretical tools commonly used to approach the problem and look at two particular limits of the problem, namely, a weakly interacting dot and a strongly interacting dot.*

## 2.1. THE JOSEPHSON AND PROXIMITY EFFECTS

THIS chapter begins with a short historical recollection of the Josephson effect which is overlooked in formal publication and perhaps interesting for a general audience. Tunneling supercurrents were first predicted by Brian Josephson in 1962 while he was a PhD student at the Royal Society Mond Laboratory in Cambridge[1]. It was his fascination with broken symmetry in superconductors, introduced through lectures by Phil Anderson[2, 3], that lead him to explore the possibility of observing signatures of broken symmetry experimentally[4]. He knew that the phase angle itself would not be observable as it is a constant throughout a bulk superconductor but that if two superconductors were connected by a thin barrier they could exchange electrons and thereby perhaps give information about the phase difference. He was at first not concerned with tunneling supercurrents, as the general consensus at the time was that the probability for two electrons (a Cooper pair) to tunnel together would be too small to observe, but more about the affect that the phase difference would have on the normal current of tunneling quasiparticles. By treating the tunneling of quasiparticles as a perturbation (transparency  $\ll 1$ ) on a system of two independent subsystems between which tunneling does not occur, he was able to obtain the now well known AC and DC Josephson effects. The AC effect predicted that at finite voltages the tunneling current would have an AC component that oscillates at a frequency of  $2eV/\hbar$  where  $V$  is the voltage across the junction. The DC effect on the other hand predicted a supercurrent ( $I_s$ ) at  $V = 0$  V. The DC effect, Josephson later noted, was unexpected and quite surprising to be of the same order of magnitude as the quasiparticle current[4], for given values of the phase difference across the barrier,  $I_s = I_c \sin \Delta\phi$ . Experimental observation of the DC Josephson effect was reported a year later by Anderson and Rowell[5]. Josephson additionally noted at the end of his seminal paper on tunneling supercurrents that similar effects should be expected if the two superconductors were separated by a thin normal region[1] but this effect, later termed "the proximity effect", in heterogeneous junctions was developed independently by several people.

Early theoretical understanding of the normal metal weak link was developed by de Gennes[6] for temperatures close to the critical temperature and experimental work in SNS (superconductor-normal metal-superconductor) junctions was carried out years before by Meissner[7, 8]. The language of the early understanding of the proximity effect was indefinite as Cooper pairs were said to "spread" or "leak" into the normal metal and electrons into the superconductor in the reverse proximity effect[9]. Independently and during the development of the proximity effect, Andreev developed a particle scattering process at the interface between a superconductor and a normal metal to explain the increased thermal resistance of an NS boundary for a superconductor in the intermediate state[10]. It was not until fairly recently though that this scattering process was finally understood as the central mechanism responsible for the proximity effect in heterogeneous junctions[11–13]. In the Andreev reflection process, an incident electron at an NS interface is reflected as a phase conjugate hole allowing the creation of a Cooper pair on the superconductor side. Andreev reflection is what drives the proximity effect locally at the interface.

The rest of this chapter is structured in the following way: we start with the basic framework of an inhomogeneous superconductor and derive the density of states, we

then investigate the interface between a superconductor and a normal metal and the mechanism of Andreev reflection which mediates charge transfer at such an interface. We then discuss multiple Andreev reflections which can give rise to a dissipative current at energies below the superconducting gap. We then move away, figuratively speaking, from the interface to describe the pair correlations that take place in the normal metal far from the interface (diffusive regime). These sections sufficiently describe the hybrid superconducting electrodes which are the experimental platforms described in chapter 3 and chapter 4. We then finish the chapter with a look at the modified Anderson impurity model in the weakly and strongly interacting regimes which describes the experimental system in chapter 5. Before diving in, I would like to acknowledge several theses that I have found invaluable in writing this chapter[14–17].

## 2.2. BOGOLIUBOV-DE GENNES EQUATION

The problem of a superconducting junction with a weak link belongs to a larger class of investigation devoted to the inhomogeneous superconductor. An inhomogeneous superconductor is one in which the order parameter ( $\Delta$ ) varies in space due to, for example, an interface with another metal or a vortex core. Theory for such a system was developed by Bogoliubov and de Gennes[18, 19]. Instead of electrons paired through a virtual phonon as in BCS theory, eigenstates of the Bogoliubov de Gennes (BdG) equation are pairs of time reversed states. As an illustrative example, let us calculate the density of states of a homogeneous superconductor by building the eigenstates and eigenenergies of the BdG equation. We start with the effective Hamiltonian in the BCS mean-field approximation[19, 20]

$$H = \int dr \sum_{\sigma=\uparrow,\downarrow} \psi_{\sigma}^{\dagger} r \left[ \frac{p^2}{2m} - \mu + V_{\sigma}(r) \right] \psi_{\sigma}(r) + \int dr \left[ \Delta(r) \psi_{\uparrow}^{\dagger}(r) \psi_{\downarrow}^{\dagger}(r) + \Delta^*(r) \psi_{\uparrow}(r) \psi_{\downarrow}(r) \right] \quad (2.1)$$

where  $\psi_{\sigma}^{\dagger}(r)$  ( $\psi_{\sigma}(r)$ ) is the creation (annihilation) operator for an electron of spin  $\sigma$  at position  $r$ ,  $\Delta$  is the pair potential,  $\mu$  is the chemical potential, and  $V(r)$  is the electrostatic potential. Bagwell and Data have shown that the BdG equation can be recast into a one-particle wave equation through the introduction of a spinor[21],

$$\Psi(r) = \begin{pmatrix} \psi_{\uparrow}(r) \\ \psi_{\downarrow}^{\dagger}(r) \end{pmatrix}. \quad (2.2)$$

This can be understood as a global annihilation of a "quasiparticle" made of a superposition of a spin-up electron annihilator and a spin-down hole creator. With this change the effective Hamiltonian can be written as,

$$H = \int dr \Psi^{\dagger}(r) H_{BdG} \Psi(r), \quad (2.3)$$

where

$$H_{BdG} = \begin{pmatrix} \frac{p^2}{2m} - \mu + V_{\uparrow}(r) & \Delta(r) \\ \Delta^*(r) & -\frac{p^2}{2m} - \mu + V_{\downarrow}(r) \end{pmatrix} \quad (2.4)$$

To diagonalize 2.3, we must first solve the one particle Schrödinger equation,

$$H_{bdG} \begin{pmatrix} u_k(r) \\ v_k(r) \end{pmatrix} = E_k \begin{pmatrix} u_k(r) \\ v_k(r) \end{pmatrix}. \quad (2.5)$$

This is known as the Bogoliubov de Gennes equation and one looks for an orthonormal basis of solutions which can decompose  $\Psi = \sum_k \gamma_k \varphi_k$ . The wave function for a quasiparticle described by this Hamiltonian is a two-dimensional vector composed of a "spin-up electron" part and a "spin-down hole" part.

In the case of a completely homogeneous superconductor with a constant pair potential  $\Delta(r) = \Delta_0 e^{i\phi}$  and with  $V(r) = 0$ , the eigenfunctions of the BdG equation are quasiparticle plane waves of the form:

$$\begin{aligned} \varphi_{k-} &= \begin{pmatrix} u_k \\ v_k \end{pmatrix} e^{ikr} \\ \varphi_{k+} &= \begin{pmatrix} u_k^* \\ -v_k^* \end{pmatrix} e^{ikr} \end{aligned} \quad (2.6)$$

with coefficients and excitation energies given by,

$$\begin{aligned} u_k(r, \phi) &= e^{-i\phi/2} \sqrt{\frac{1}{2} \left( 1 + \frac{\hbar^2 k^2 / 2m - \mu}{\sqrt{\Delta_0^2 + (\hbar^2 k^2 / 2m - \mu)^2}} \right)} \\ v_k(r, \phi) &= -e^{i\phi/2} \sqrt{\frac{1}{2} \left( 1 - \frac{\hbar^2 k^2 / 2m - \mu}{\sqrt{\Delta_0^2 + (\hbar^2 k^2 / 2m - \mu)^2}} \right)} \\ E_{k\pm} &= \pm \sqrt{\Delta_0^2 + (\hbar^2 k^2 / 2m - \mu)^2}. \end{aligned} \quad (2.7)$$

The DOS is then directly calculated by equating the normal state and superconducting state DOS,  $N_s(E)dE = N_n(\epsilon)d\epsilon/2$ , where  $N_n$  is the normal state DOS assumed to be constant and equal to the density of states at the Fermi level  $N_n(\epsilon) = N_n(0)$  and  $\epsilon = \hbar^2 k^2 / 2m - \mu$ . We thus have,

$$N_s(E) = \frac{N_n(0)}{2} \begin{cases} \frac{|E|}{\sqrt{E^2 - \Delta^2}} & |E| > \Delta \\ 0 & |E| < \Delta. \end{cases} \quad (2.8)$$

Figure 2.1 shows the calculated DOS for a homogeneous superconductor using Equation 2.8. In Figure 2.1(b) we show the DOS in the one particle picture where the states below the chemical potential are filled (black area) and the states above the chemical potential are empty.

### 2.3. ANDREEV REFLECTION

Andreev reflection is the charge transfer process at the interface between a normal metal and a superconductor which converts a dissipative current to a dissipation-less current.



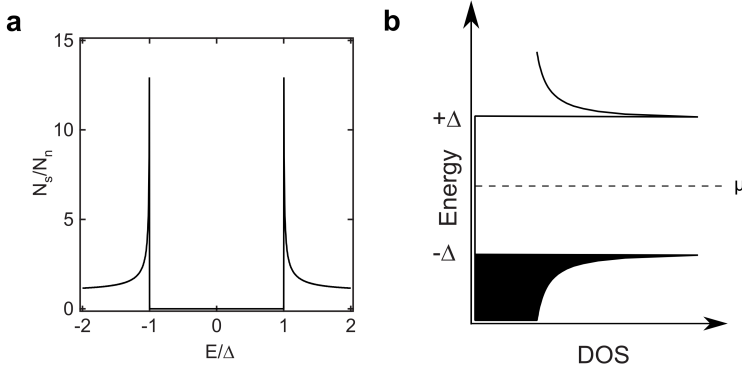


Figure 2.1: (a) Calculated density of states of a homogeneous superconductor. (b) DOS in the "one-particle" picture where the states below the Fermi level are filled and the states above are empty.

An electron incident on an interface between a superconductor and a normal metal has a certain probability to be normally reflected, reflected as a hole (Andreev reflection, Figure 2.2), or transmitted through the barrier. In the event of an Andreev reflection, two electrons are transferred to the superconductor: one from the incident electron and one from the reflected hole. The process is phase coherent; the reflected hole carries the phase of the incident electron with the addition of a phase shift given by the macroscopic phase of the superconductor,  $\phi$ , and an energy dependent phase shift, derived below.

As Andreev reflection is the central mechanism in the proximity effect, as an instructive example, we calculate the probability for Andreev reflection by constructing suitable wavevectors that solve the BdG equation. In one dimension, a suitable choice is four types of quasiparticle waves for a given energy:

$$\psi_{\pm k_e} = \begin{pmatrix} u_e \\ v_e \end{pmatrix} e^{\pm i k_e x} \quad (2.9)$$

and

$$\psi_{\pm k_h} = \begin{pmatrix} u_h \\ v_h \end{pmatrix} e^{\pm i k_h x} \quad (2.10)$$

where  $\psi$  is the position space representation of the BCS quasiparticles. In the spin-degenerate case, the coefficients and wavevectors are given by:

$$\begin{aligned} u_{e,h}(E, \phi) &= e^{i\phi/2} \left[ \frac{1}{2} (1 + \sigma_{e,h} \sqrt{1 - \frac{\Delta_0^2}{E^2}}) \right]^{1/2} \\ v_{e,h}(E, \phi) &= e^{-i\phi/2} \text{sgn}(E) \left[ \frac{1}{2} (1 - \sigma_{e,h} \sqrt{1 - \frac{\Delta_0^2}{E^2}}) \right]^{1/2} \\ k_{e,h} &= k_F \left( 1 + \sigma_{e,h} \text{sgn}(E) \frac{\sqrt{E^2 - \Delta_0^2}}{\mu} \right)^{1/2} \end{aligned} \quad (2.11)$$

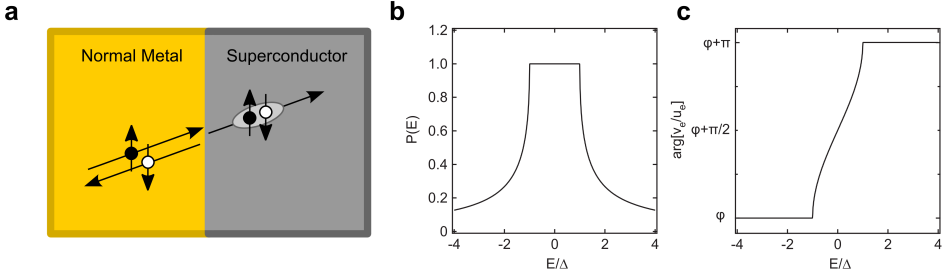


Figure 2.2: (a) Andreev reflection process at the interface of a superconductor and a normal metal. (b) Probability of Andreev reflection as a function of energy. (c) Phase shift acquired by a reflected hole.

where  $\sigma_{e,h} = \pm 1$  and  $E$  is the excitation energy given in Equation 2.7. The wavefunction describing the Andreev reflection process can now be constructed from these results. The interface is positioned at  $x = 0$  and the pairing potential is set to zero in the normal region.

$$\begin{aligned} \psi_E(x) = & \left[ A_E \begin{pmatrix} 1 \\ 0 \end{pmatrix} \exp(ik_e^N x) + B_E \begin{pmatrix} 0 \\ 1 \end{pmatrix} \exp(ik_h^N x) \right] \theta(-x) \\ & + \left[ C_E \begin{pmatrix} u_e \\ v_e \end{pmatrix} \exp(ik_e x) \right] \theta(x) \end{aligned} \quad (2.12)$$

where  $\theta(x)$  is the Heaviside function. Using the continuity condition that the derivative be equal at  $x = 0$ , we have that  $A_E = C_E u_e$  and  $B_E = C_E v_e$ . The probability for Andreev reflection is then  $\alpha(E, \phi) = B_E / A_E = v_e / u_e$ . Using Equation 2.11, one finds that the probability is then given by:

$$\alpha(E, \phi) = \begin{cases} \frac{E - \text{sgn}(E)\sqrt{E^2 - \Delta^2}}{E - i\sqrt{\Delta^2 - E^2}} & |E| > \Delta \\ E - i\sqrt{\Delta^2 - E^2} & |E| < \Delta \end{cases} \quad (2.13)$$

and the phase shift is given by:

$$\arg(v_e / u_e) = \begin{cases} \phi & E < -\Delta \\ \phi + \arccos(E/\Delta) & |E| < \Delta \\ \phi + \pi & E > \Delta. \end{cases} \quad (2.14)$$

The modulus of the probability ( $P(E)$ ) and the phase shift are plotted in Figure 2.2. For an electron with energy less than the gap, the Andreev reflection is perfect and it acquires an energy dependent phase shift.

## 2.4. MULTIPLE ANDREEV REFLECTIONS

Multiple Andreev reflections were first proposed by Blonder, Tinkham, and Klapwijk in 1982 to explain experimental observations of sub-gap structure and excess current in Josephson junctions[22, 23]. At finite voltages the AC Josephson effect produces an oscillating current which does not contribute to the total DC current through the junction at bias voltages less than the gap. However, a dissipative current can flow which is due

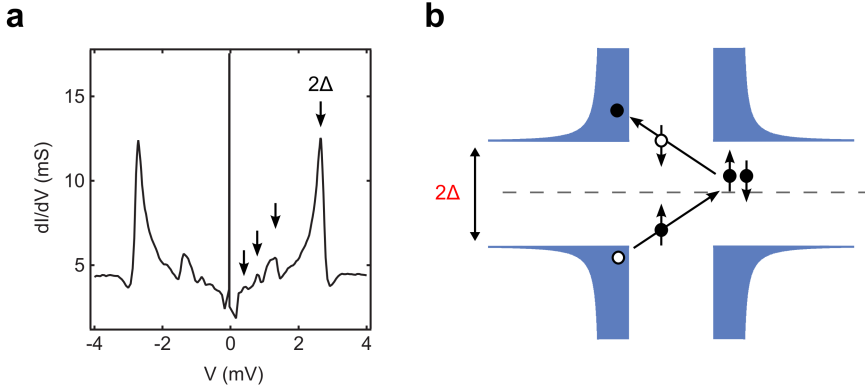


Figure 2.3: (a) Multiple Andreev reflection in a molybdenum disulfide - molybdenum rhenium SNS junction. (b) 2nd order MAR process with three Andreev reflections.

to multiple Andreev processes occurring at both interfaces of an SNS junction. These multiple reflections can lead to resonant peaks in the conductance spectra at voltages below the bulk superconducting gap such as those in Figure 2.3. The largest side peaks are at energies of twice the superconducting gap and the smaller peaks within the gap are from resonant MAR processes. These peaks lie at energies given by:

$$eV_b = \frac{2\Delta}{n} \quad (2.15)$$

where the  $n^{\text{th}}$  order corresponds to  $(n - 1)$  Andreev reflections. Figure 2.3 shows a 2nd order MAR process in a scattering picture that corresponds to three Andreev reflections. The electron (hole) gain an energy of  $eV$  where  $V$  is the bias voltage with each trip across the junction.

## 2.5. THE DIFFUSIVE REGIME

In this section we explore the diffusive regime which describes the proximity induced electrodes that are incorporated in chapters 4 and 5. Observable quantities in this regime can be calculated from the quasi-classical theory<sup>1</sup> developed by Gor'kov[26] and simplified by Eilenberger[27] and later developed for dirty superconductors by Usadel[28]. As opposed to the BdG equation, this formalism does not require solving the Schrödinger equation with suitable microscopic wavefunctions but instead directly leads to diffusion-like equations which are related to physical quantities. In the quasi-classical theory, the energy dependent correlations between time-conjugate electron states are described by the retarded ( $G^R$ ), advanced ( $G^A$ ), and Keldysh ( $G^K$ ) Green's functions given by:

$$G^R(r, \epsilon) = \mathcal{F}[-i\theta(t - t') \left( \begin{array}{cc} \langle \{\Psi_{\uparrow}(r, t), \Psi_{\uparrow}^{\dagger}(r, t')\} \rangle & \langle \{\Psi_{\uparrow}(r, t), \Psi_{\downarrow}(r, t')\} \rangle \\ -\langle \{\Psi_{\uparrow}^{\dagger}(r, t), \Psi_{\uparrow}^{\dagger}(r, t')\} \rangle & -\langle \{\Psi_{\uparrow}^{\dagger}(r, t), \Psi_{\downarrow}(r, t')\} \rangle \end{array} \right) ] \quad (2.16)$$

<sup>1</sup>Thorough reviews are available for the interested reader[24, 25].

$$G^A(r, \epsilon) = \mathcal{F}[-i\theta(t-t') \left( \begin{array}{cc} \langle \{\Psi_{\uparrow}(r, t), \Psi_{\uparrow}^{\dagger}(r, t')\} \rangle & \langle \{\Psi_{\uparrow}(r, t), \Psi_{\downarrow}(r, t')\} \rangle \\ -\langle \{\Psi_{\uparrow}^{\dagger}(r, t), \Psi_{\uparrow}^{\dagger}(r, t')\} \rangle & -\langle \{\Psi_{\uparrow}^{\dagger}(r, t), \Psi_{\downarrow}(r, t')\} \rangle \end{array} \right) ] \quad (2.17)$$

$$G^K(r, \epsilon) = \mathcal{F} \left[ -i \left( \begin{array}{cc} \langle \{\Psi_{\uparrow}(r, t), \Psi_{\uparrow}^{\dagger}(r, t')\} \rangle & \langle \{\Psi_{\uparrow}(r, t), \Psi_{\downarrow}(r, t')\} \rangle \\ -\langle \{\Psi_{\downarrow}(r, t), \Psi_{\uparrow}^{\dagger}(r, t')\} \rangle & -\langle \{\Psi_{\downarrow}(r, t), \Psi_{\downarrow}(r, t')\} \rangle \end{array} \right) \right] \quad (2.18)$$

where  $\mathcal{F}$  denotes a Fourier transform,  $\Psi_{\uparrow}^{\dagger}(r, t)$  and  $\Psi_{\downarrow}(r, t)$  are the creation and annihilation operators of an electron with spin  $\uparrow$  at position  $r$ ,  $\theta$  is the Heaviside function, and where we denote an average by  $\langle \dots \rangle$ , and the commutator and anticommutator by  $\{ \dots \}$  and  $[ \dots ]$ , respectively. A more compact form can be attained following the general relations  $(G^R)^2 = \hat{1}$ ,  $(G^A)^2 = \hat{1}$ , and  $G^R G^K + G^K G^A = 0$ ,

$$G(r, \epsilon) = \begin{pmatrix} G^R & G^K \\ 0 & G^A \end{pmatrix} \quad (2.19)$$

which obeys the Usadel equation:

$$\hbar D \nabla (G \nabla G) + i [\hat{H}_0, G] - \frac{1}{\Gamma_{sf}} [\hat{\sigma}_z G \hat{\sigma}_z, G] = 0 \quad (2.20)$$

where

$$\hat{H}_0 = \begin{pmatrix} H_0 & 0 \\ 0 & H_0 \end{pmatrix}; \hat{\sigma}_z = \begin{pmatrix} \sigma_z & 0 \\ 0 & \sigma_z \end{pmatrix} \quad (2.21)$$

with

$$H_0 = \begin{pmatrix} E & \Delta \\ -\Delta^* & E \end{pmatrix} \quad (2.22)$$

where  $E$  is the energy,  $\Delta(r)$  is the position dependent effective pair potential of BCS theory,  $\Gamma_{sf}$  is the spin flip scattering rate, and  $\sigma_z$  is the third Pauli matrix. With the Green's functions defined, the self consistent equation for the pair potential is then given by:

$$\Delta = n_0 V_{eff} \int_0^{\hbar w_D} dE \frac{1}{4i} \text{Tr}[(\sigma_x + i\sigma_y) G^K] \quad (2.23)$$

where  $n_0$  is the normal state density of states,  $V_{eff}$  is the phonon-mediated interaction potential, and  $w_D$  is the Debye frequency. This is what makes solving the Usadel equations, and therefore calculating some physical quantity, a hard task as the solutions to the Green's functions at some energy depend on a pair potential which depends on all energies. Typically observables are calculated using iterative numerical methods by first imposing boundary conditions on the Green's functions. Then, one solves the Usadel equation starting with the simplest guess for the pair potential (a simple step function). The Green's functions are then solved for a large range of energies (from  $E=0$  to several times  $\Delta$ ) and the results are used to calculate the new estimate for the pair potential. This process is iterated until self-consistency is reached.

### 2.5.1. PARAMETERIZATION

For calculations, it is common to use a parametrization ( $\theta$  parameterization) which has proved to be useful that describes angles on a complex unit sphere. The parameters are  $\theta(x, E)$  which is the complex superconducting order angle and  $\phi(x, E)$  which is the real superconducting phase. Using this parameterization, the Green's functions can be written as:

$$G^R = \begin{pmatrix} \cos\theta & \sin\theta e^{i\phi} \\ \sin\theta e^{-i\phi} & -\cos\theta \end{pmatrix}$$

and

$$G^A = \begin{pmatrix} -\cos\theta^* & \sin\theta^* e^{i\phi^*} \\ \sin\theta^* e^{-i\phi} & -\cos\theta^* \end{pmatrix}$$

where  $\theta(x, E)$  represents the complex superconducting order and  $\phi(x, E)$  is an energy dependent superconducting phase. The Keldysh function, at equilibrium, is given by

$$G^K = G^R \hat{h} - \hat{h} G^A$$

with the distribution  $\hat{h}$  matrix defined as:

$$\hat{h} = \begin{pmatrix} 1 - 2f_e & 0 \\ 0 & 2f_h - 1 \end{pmatrix}$$

with  $f_e$  and  $f_h$  the distribution functions for electrons and holes.

With this parametrization, the Usdael equation becomes:

$$\frac{\hbar D}{2} \nabla^2 + [iE - \frac{\hbar}{\Gamma_{sf}} \cos\theta \sin\theta + \Delta \cos\theta] = 0, \quad (2.24)$$

and the self consistency equation becomes:

$$\Delta = n_0 V_{eff} \int_0^{\hbar w_D} dE \tanh\left(\frac{E}{2k_B T}\right) \text{Im}[\sin\theta(x, E)] e^{i\phi(x, E)} \quad (2.25)$$

The parameters are solved self-consistently and once they are known several characteristic quantities can be calculated. The density of states, for instance, can be calculated from

$$n(x, E) = N(0) \text{Re}[\cos(\theta(x, E))]$$

with  $N(0)$  the normal metal density of states.

Figure 2.4 shows the modified DOS calculated from the Usadel equation for the 1D heterostructure shown in Figure 2.4(a). The modified DOS is calculated at  $x = L$  (for  $L = 1$  to 300 nm) which is at the end of the gold 1D wire near a vacuum interface<sup>2</sup>. The shorter the 1D wire, the more the DOS resembles the bulk BCS DOS. A mini-gap (a term signifying the smaller quasiparticle gap in the modified DOS) can be seen for all the curves. The red curve in 2.4(b) is for  $L = 100$  nm and is close to the length of the gold electrodes in the experimental systems in chapter 4 and chapter 5.

<sup>2</sup>The interface between the superconductor and the gold wire is assumed to be transparent. This calculation is made using python code developed by Virtanen and Heikkila in Ref. [29]

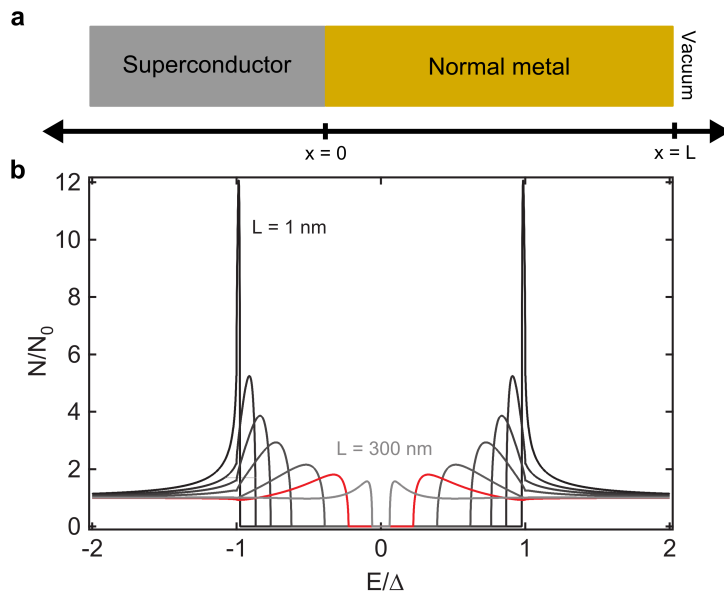


Figure 2.4: (a) Superconductor-normal geometry used for calculations.  $L$  is the length of the normal metal and the position at which the local DOS is given in panel (b). (b) Normalized modified density of states as a function of energy for different lengths of normal metal given at the position of  $x = L$ . The red curve shows the modified DOS at  $x = 100 \text{ nm}$ . Calculations courtesy Joeri de Bruijckere using Python code developed by Virtanen and Heikkilä in Ref. [29].

## 2.6. THE JOSEPHSON QUANTUM DOT

A superconducting (or modified) Anderson impurity model captures the physics of a single quantum level coupled to superconducting leads (colloquially, the Josephson quantum dot) which begins to describe the hybrid experimental systems studied in chapters 4 and 5. The Josephson quantum dot belongs to a larger class of study that began in the late 50s with Anderson's theory for dirty superconductors (with non-magnetic impurities)[30]. He showed that by pairing time reversed states all the equilibrium properties for a superconductor, such as  $T_c$ ,  $H_c$ , and  $\Delta$ , are essentially independent of the electronic mean free path. Subsequently, Abrikosov and Gor'kov showed that if the impurities are magnetic, i.e. time reversal symmetry is violated, a strong reduction in  $T_c$  would be expected and for large enough concentrations, gap-less superconductivity would exist[31]. These studies led to further investigations at the single impurity limit<sup>3</sup> independently by Yu, Shiba, and Rusinov in the late 60s where it was shown that sub-gap states exist locally near an impurity[33–35]. Continuing, we first discuss the modified Anderson model and the large-gap limit which leads to the well-known Andreev bound states. We then discuss the large  $U$  (charging energy) limit which pertains to the molecular hybrid systems discussed in this thesis.

The single level Anderson model is given by,

$$H_d = \sum_{\sigma} \epsilon_d d_{\sigma}^{\dagger} d_{\sigma} + U n_{\uparrow} n_{\downarrow}, \quad (2.26)$$

where  $\epsilon_d$  is the single-particle energy of the localized state with spin  $\sigma$ ,  $n_{\sigma}$  is the occupation,  $d_{\sigma}^{\dagger}$  ( $d_{\sigma}$ ) is the creation (annihilation) operator of an electron on the dot, and  $U$  is the on-site Coulomb interaction. The superconducting leads are built in through the BCS Hamiltonian of the form:

$$H_{R,L} = \sum_{\vec{k},\sigma} \epsilon_{\vec{k}} c_{\vec{k},\sigma}^{\dagger} c_{\vec{k},\sigma} - \sum_{\vec{k}} (\Delta_i c_{\vec{k},1,i}^{\dagger} c_{-\vec{k},1,i}^{\dagger} + H.c.), \quad (2.27)$$

where  $c_{\vec{k},\sigma,i}^{\dagger}$  ( $c_{\vec{k},\sigma,i}$ ) is the creation (annihilation) operator for an electron with spin  $\sigma$  and wavevector  $\vec{k}$  in the  $i = L, R$  leads,  $\Delta_i = \Delta e^{i\phi_i}$  is the superconducting gap, and  $\epsilon_{\vec{k},i}$  is the kinetic energy measured from the Fermi-level. The tunneling to the leads is modeled in the usual way,

$$H_{T,R,L} = \sum_{\vec{k},\sigma} (t d_{\sigma}^{\dagger} c_{\vec{k},\sigma,i} + H.c.). \quad (2.28)$$

where  $\Gamma = 2\pi t^2 \rho_0$ .

The relevant energy scales of the system are the charging energy ( $U$ ), the level broadening (or hybridization) ( $\Gamma$ ), and the superconducting gap ( $\Delta$ ). Figure 2.5(a) shows an energy diagram of the coupled system in which a quantum dot is coupled to superconducting electrodes.

The phase diagram for this system is also shown in Figure 2.5(b), given the characteristic energy scales. The ground state of the coupled system can be a BCS-like singlet, and Kondo singlet, or a degenerate doublet depending on the relative energies.

<sup>3</sup>For the interested reader, an accessible review on single impurities in superconducting hosts has been provided by Balatsky, Vekhter, and Zhu[32].

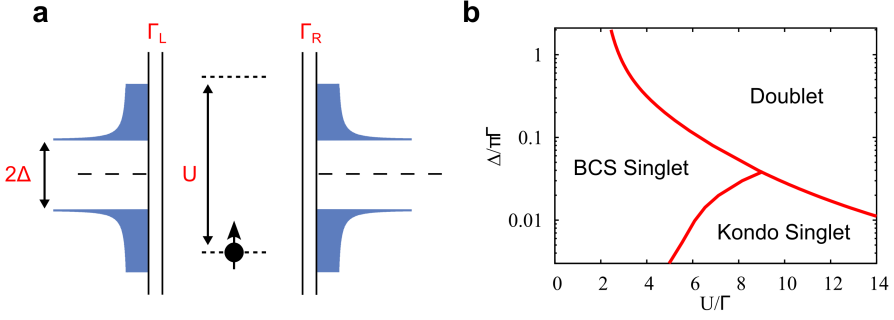


Figure 2.5: Relevant energy scales of the system. (a) Schematic of the relevant energy scales in the semiconductor picture. (b) Phase diagram of the ground states given the relevant energy scales of the system. This panel is adapted from Ref. [36].

An exact solution to the modified Anderson model is only possible if the Coulomb interaction is neglected. For an arbitrary range of parameters, powerful numerical methods are required such as numerical renormalization group theory[37–45] and quantum Monte Carlo calculations[46–50]. These methods tend to agree quantitatively with experimental observations [46, 47, 51]. Both methods are time consuming and require heavy computational resources so several analytic schemes have been developed over the years to deal with the modified Anderson model. For example, in the limiting case of an infinitely large gap  $\Delta \rightarrow \infty$ , the model is analytically solvable and results in the well known Andreev bound states. In the limit of large charging energy  $U \rightarrow \infty$ , the case concerning single molecule junctions, the model again requires computational methods but we will discuss the relevant literature on the subject and the possible ground states for the system.

### 2.6.1. SUPERCONDUCTING ATOMIC LIMIT

An analytical approach to the modified Anderson model is the superconducting atomic limit. In this limit the electronic bandwidth ( $D$ ) is taken to infinity before the superconducting gap. This order is important because if the  $\Delta \rightarrow \infty$  is taken first the dot would be completely decoupled from the leads. In this limit, one arrives at an effective Hamiltonian which describes a sort of superconducting molecule[52].

$$H_{eff} = \sum_{\sigma} \xi_d a_{\sigma}^{\dagger} d_{\sigma} - |\Gamma| (d_{\uparrow}^{\dagger} d_{\downarrow}^{\dagger} + H.c.) + \frac{U}{2} (\sum_{\sigma} a_{\sigma}^{\dagger} d_{\sigma} - 1)^2, \quad (2.29)$$

where  $\xi_d = \epsilon_d + \frac{U}{2}$ ,  $|\Gamma_{\phi}|$  is the coupling to the left and right lead which now also carries the phases of each superconductor. This effective Hamiltonian can be diagonalized using the Bogoliubov-Valatin transformation which allows one to arrive at the four eigenstate and eigenenergies of the system. The eigenstates are the doublet  $|\uparrow\rangle, |\downarrow\rangle$  and two BCS like states given by:



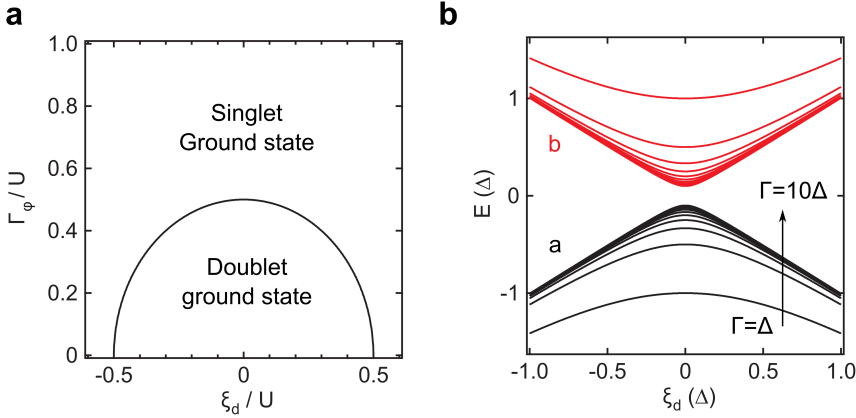


Figure 2.6: (a) Phase diagram of the singlet and doublet ground state in the superconducting atomic limit. (b) Energy of the resonant bound states as a function of the level energy ( $\xi$ ).

$$\begin{aligned} |+\rangle &= u |\uparrow\downarrow\rangle + v^* |0\rangle, \\ |-\rangle &= -v^* |\uparrow\downarrow\rangle + u |0\rangle, \end{aligned} \quad (2.30)$$

where  $|0\rangle$  is the empty dot state and  $|\uparrow\downarrow\rangle$  is the doubly occupied dot state. The amplitudes  $u$  and  $v$  are given by:

$$\begin{aligned} u &= 1/2 \sqrt{1 + \xi_d / \sqrt{\xi_d^2 + \Gamma_\phi^2}}, \\ v &= 1/2 \sqrt{1 - \xi_d / \sqrt{\xi_d^2 + \Gamma_\phi^2}}. \end{aligned} \quad (2.31)$$

The energies of the spin doublet are given by  $E_{\pm}^0 = E_{\downarrow}^0 = \xi_d$  and the energies of the BCS-like singlets are given by  $E_{\pm}^0 = U/2 \pm \sqrt{\xi_d^2 + \Gamma_\phi^2} + \xi_d$ . The ground state for the system is the BCS-like state,  $|-\rangle$ , or the degenerate doublet depending on the phase difference between the bulk superconducting leads. A quantum phase transition occurs at  $\xi_d^2 + \Gamma_\phi^2 = U^2/4$ . This boundary is plotted in Figure 2.6(a) as a function of coupling and energy level.

Spectroscopy is a measure of the energy difference between the ground state and the first excited state (so always either the doublet or low energy singlet). The energy for the bound states and thus the resonances that appear in transport measurements are given by this energy difference which can be written as:

$$\begin{aligned} a_0 &= E_-^0 - E_\sigma^0 = \frac{U}{2} - \sqrt{\xi_d^2 - \Gamma_\phi^2}, \\ b_0 &= E_+^0 - E_\sigma^0 = \frac{U}{2} + \sqrt{\xi_d^2 - \Gamma_\phi^2}. \end{aligned} \quad (2.32)$$

In the case of zero charging energy, the states can be easily visualized in Figure 2.6(b). Here we plot the bound state resonance for different coupling energies,  $\Gamma_\phi$ . The energy of the bound state moves toward the gap edge for stronger coupling.

## 2

### 2.6.2. THE LARGE U LIMIT AND A SINGLE CLASSICAL SPIN

For larger charging energies, compared with the gap, the effective Hamiltonian becomes again unsolvable and numerical methods must be used. For example, in chapter 5 we calculate conductance curves using the non-crossing approximation[53, 54]. Nonetheless, it is perhaps instructive to look at the case of bound states from a classical spin (ignoring Kondo correlations,  $T \gg T_K$ ) in a superconductor which was the starting point by Yu, Shiba, and Rusinov[33–35].

An impurity can be built into the BCS Hamiltonian with a combination of potential scattering,  $U_{pot}(r) = V(r)\tau_3$ , and a magnetic scattering term given by:

$$H_{int} = \frac{1}{2N} \sum_{k,k',\alpha,\beta} J(k-k') c_{k,\alpha}^\dagger \sigma_{\alpha\beta} \cdot \mathbf{S}_{k'\beta} \quad (2.33)$$

where  $\tau_i$  are the Pauli matrices in particle-hole space,  $\sigma_i$  are the Pauli matrices in spin space, and  $J$  is the exchange constant. Including the unperturbed BCS Hamiltonian, the complete system describes an impurity with potential and magnetic scattering embedded in a superconductor.

In order to calculate the bound states, a Bogoliubov transformation is performed which leads to the following coupled equations[33, 35]:

$$Eu_\alpha(r) = \epsilon(k)u_\alpha(r) + i\Delta\sigma_{\alpha\beta}^y v_\beta(r) + U_{\alpha\beta}(r)u_\beta(r), \quad (2.34)$$

$$Ev_\alpha(r) = -\epsilon(k)v_\alpha(r) + i\Delta\sigma_{\alpha\beta}^y u_\beta(r) - U_{\alpha\beta}(r)v_\beta(r). \quad (2.35)$$

This can be solved using a Fourier transform and expanding the impurity potentials in spherical harmonics in k-space,  $J_l$  and  $V_l$ . An elegant solution can be arrived at by using the phase shift  $\delta_l$  of the scattering for up and down electrons. The final result of the bound state energy is then given by:

$$E_b = \cos(\delta_l^+ - \delta_l^-) \quad (2.36)$$

with

$$\tan(\delta_l^\pm) = (\pi N_0)(V_l \pm J_l S/2). \quad (2.37)$$

$E_b$  is the bound state (sub-gap excited state) first proposed by Yu, Shiba, and Rusinov. The bound state energy starts near the gap edge ( $E_b \approx \Delta$ ) for weak scattering and moves to lower energy with stronger scattering.

Figure 2.7 shows the first numerical renormalization group calculations for the superconducting Anderson model performed by Satori *et al.* in 1992[55]. These calculations show a continuous transition of the bound state energy ( $y$ ) as a function of Kondo energy ( $T_K$ ). In the top half of the plot, the ground state is the doublet as the superconducting gap prevents screening of the impurity. This is depicted in Figure 2.7(b). Excited states for this ground state are Kondo-like singlets in which the impurity spin couples

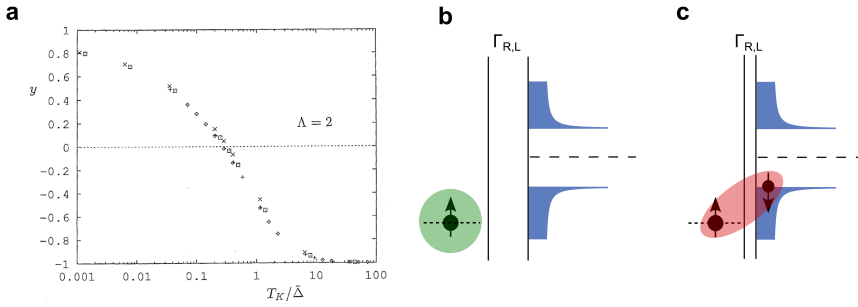


Figure 2.7: (a) Numerical renormalization group theory for the modified Anderson model. Panel modified from [55] (b) Model of the doublet ground state. (c) Model of the Kondo-singlet ground state.

with a broken Copper pair. As the coupling is increased (stronger  $T_K$ ), a phase transition occurs from the doublet ground state to a Kondo-like singlet (depicted in Figure 2.7(c)). In this regime the Kondo energy is strong enough to screen the impurity spin even in the superconducting state. Excited states for the singlet ground state are a doublet.

## REFERENCES

- [1] B. D. Josephson, *Possible new effects in superconductive tunnelling*, Physics Letters **1**, 251 (1962).
- [2] P. W. Anderson, *Random-phase approximation in the theory of superconductivity*, Physical Review **112**, 1900 (1958).
- [3] P. W. Anderson, *Concepts in solids: lectures on the theory of solids*, Vol. 58 (World Scientific, 1997).
- [4] B. D. Josephson, *The discovery of tunnelling supercurrents*, Reviews of Modern Physics **46**, 251 (1974).
- [5] P. W. Anderson and J. M. Rowell, *Probable observation of the Josephson superconducting tunneling effect*, Physical Review Letters **10**, 230 (1963).
- [6] P. G. De Gennes, *Boundary effects in superconductors*, Reviews of Modern Physics **36**, 225 (1964).
- [7] H. Meissner, *Measurements on superconducting contacts*, Physical Review **109**, 686 (1958).
- [8] H. Meissner, *Superconductivity of contacts with interposed barriers*, Physical Review **117**, 672 (1960).
- [9] J. Clarke, *The proximity effect between superconducting and normal thin films in zero field*, Le Journal de Physique Colloques **29**, C2 (1968).
- [10] A. F. Andreev, *Thermal conductivity of the intermediate state of superconductors*, Zh. Eksperim. i Teor. Fiz. **46**, 1823 (1964).
- [11] A. Furusaki and M. Tsukada, *A unified theory of clean Josephson junctions*, Physica B: Condensed Matter **165**, 967 (1990).
- [12] B. Pannetier and H. Courtois, *Andreev reflection and proximity effect*, Journal of low temperature physics **118**, 599 (2000).
- [13] T. M. Klapwijk, *Proximity effect from an Andreev perspective*, Journal of Superconductivity **17**, 593 (2004).
- [14] H. Le Sueur, *Cryogenic AFM-STM for mesoscopic physics*, Ph.D. thesis, Université Pierre et Marie Curie-Paris VI (2007).
- [15] J.-D. Pillet, *Tunneling spectroscopy of the Andreev Bound States in a Carbon Nanotube*, Ph.D. thesis, Université Pierre et Marie Curie-Paris VI (2011).
- [16] L. Bretheau, *Localized excitations in superconducting atomic contacts: Probing the Andreev doublet*, Ph.D. thesis, Ecole Polytechnique X (2013).
- [17] W. Chang, *Superconducting proximity effect in InAs nanowires*, Ph.D. thesis, Harvard University (2014).

- [18] N. N. Bogoljubov, *A new method in the theory of superconductivity. I*, Soviet Physics, JETP **7**, 41 (1958).
- [19] P.-G. De Gennes, *Superconductivity of metals and alloys* (Perseus Books Group, 1999).
- [20] M. Tinkham, *Introduction to superconductivity* (Dover, 2004).
- [21] S. Datta and P. F. Bagwell, *Can the Bogoliubov-de Gennes equation be interpreted as a 'one-particle' wave equation?* Superlattices and Microstructures **25**, 1233 (1999).
- [22] G. E. Blonder, M. Tinkham, and T. M. Klapwijk, *Transition from metallic to tunneling regimes in superconducting microconstrictions: Excess current, charge imbalance, and supercurrent conversion*, Physical Review B **25**, 4515 (1982).
- [23] M. Octavio, M. Tinkham, G. E. Blonder, and T. M. Klapwijk, *Subharmonic energy-gap structure in superconducting constrictions*, Physical Review B **27**, 6739 (1983).
- [24] D. Estève, H. Pothier, S. Guéron, N. O. Birge, and M. H. Devoret, *The proximity effect in mesoscopic diffusive conductors*, in *Mesoscopic Electron Transport* (Springer, 1997) pp. 375–406.
- [25] W. Belzig, F. K. Wilhelm, C. Bruder, G. Schön, and A. D. Zaikin, *Quasiclassical Green's function approach to mesoscopic superconductivity*, Superlattices and Microstructures **25**, 1251 (1999).
- [26] L. P. Gor'kov, *Microscopic derivation of the Ginzburg-Landau equations in the theory of superconductivity*, Sov. Phys. JETP **9**, 1364 (1959).
- [27] G. Eilenberger, *Transformation of Gorkov's equation for type II superconductors into transport-like equations*, Zeitschrift für Physik **214**, 195 (1968).
- [28] K. D. Usadel, *Generalized diffusion equation for superconducting alloys*, Physical Review Letters **25**, 507 (1970).
- [29] P. Virtanen and T. T. Heikkilä, *Thermoelectric effects in superconducting proximity structures*, Applied Physics A **89**, 625 (2007).
- [30] P. W. Anderson, *Theory of dirty superconductors*, Journal of Physics and Chemistry of Solids **11**, 26 (1959).
- [31] A. A. Abrikosov and L. Gor'kov, *Contribution to the theory of superconducting alloys with paramagnetic impurities*, Zhur. Eksptl'. i Teoret. Fiz. **39** (1960).
- [32] A. V. Balatsky, I. Vekhter, and J.-X. Zhu, *Impurity-induced states in conventional and unconventional superconductors*, Reviews of Modern Physics **78**, 373 (2006).
- [33] L. Yu, *Bound state in superconductors with paramagnetic impurities*, Acta Phys. Sin **21**, 75 (1965).

- [34] H. Shiba, *Classical spins in superconductors*, Progress of Theoretical Physics **40**, 435 (1968).
- [35] A. I. Rusinov, *Superconductivity near a paramagnetic impurity*, Soviet Journal of Experimental and Theoretical Physics Letters **9**, 85 (1969).
- [36] M. Žonda, V. Pokorný, V. Janiš, and T. Novotný, *Perturbation theory for an Anderson quantum dot asymmetrically attached to two superconducting leads*, Physical Review B **93**, 024523 (2015).
- [37] T. Yoshioka and Y. Ohashi, *Numerical renormalization group studies on single impurity Anderson model in superconductivity: a unified treatment of magnetic, nonmagnetic impurities, and resonance scattering*, Journal of the Physical Society of Japan **69**, 1812 (2000).
- [38] M.-S. Choi, M. Lee, K. Kang, and W. Belzig, *Kondo effect and Josephson current through a quantum dot between two superconductors*, Physical Review B **70**, 020502 (2004).
- [39] J. Bauer, A. Oguri, and A. C. Hewson, *Spectral properties of locally correlated electrons in a Bardeen-Cooper-Schrieffer superconductor*, Journal of Physics: Condensed Matter **19**, 486211 (2007).
- [40] T. Hecht, A. Weichselbaum, J. von Delft, and R. Bulla, *Numerical renormalization group calculation of near-gap peaks in spectral functions of the Anderson model with superconducting leads*, Journal of Physics: Condensed Matter **20**, 275213 (2008).
- [41] A. Oguri, Y. Tanaka, and A. C. Hewson, *Quantum phase transition in a minimal model for the Kondo effect in a Josephson junction*, Journal of the Physical Society of Japan **73**, 2494 (2004).
- [42] A. Martín-Rodero and A. L. Yeyati, *The Andreev states of a superconducting quantum dot: Mean field versus exact numerical results*, Journal of Physics: Condensed Matter **24**, 385303 (2012).
- [43] A. Oguri, Y. Tanaka, and J. Bauer, *Interplay between Kondo and Andreev-Josephson effects in a quantum dot coupled to one normal and two superconducting leads*, Physical Review B **87**, 075432 (2013).
- [44] C. Karrasch, A. Oguri, and V. Meden, *Josephson current through a single Anderson impurity coupled to BCS leads*, Physical Review B **77**, 024517 (2008).
- [45] R. Zitoko, J. S. Lim, R. López, and R. Aguado, *Shiba states and zero-bias anomalies in the hybrid normal-superconductor Anderson model*, Physical Review B **91**, 045441 (2015).
- [46] R. Delagrangé, D. J. Luitz, R. Weil, A. Kasumov, V. Meden, H. Bouchiat, and R. Deblock, *Manipulating the magnetic state of a carbon nanotube Josephson junction using the superconducting phase*, Physical Review B **91**, 241401 (2015).

- [47] D. J. Luitz, F. F. Assaad, T. Novotný, C. Karrasch, and V. Meden, *Understanding the Josephson current through a Kondo-correlated quantum dot*, Physical Review Letters **108**, 227001 (2012).
- [48] D. J. Luitz and F. F. Assaad, *Weak-coupling continuous-time quantum Monte Carlo study of the single impurity and periodic Anderson models with s-wave superconducting baths*, Physical Review B **81**, 024509 (2010).
- [49] F. Siano and R. Egger, *Josephson current through a nanoscale magnetic quantum dot*, Physical Review Letters **93**, 047002 (2004).
- [50] K. Kusakabe, Y. Tanaka, and Y. Tanuma, *Numerical study of unconventional superconductor/a quantum dot/unconventional superconductor junction*, Physica E: Low-dimensional Systems and Nanostructures **18**, 50 (2003).
- [51] J.-D. Pillet, P. Joyez, M. F. Goffman, *et al.*, *Tunneling spectroscopy of a single quantum dot coupled to a superconductor: From Kondo ridge to Andreev bound states*, Physical Review B **88**, 045101 (2013).
- [52] T. Meng, S. Florens, and P. Simon, *Self-consistent description of Andreev bound states in Josephson quantum dot devices*, Physical Review B **79**, 224521 (2009).
- [53] A. A. Clerk and V. Ambegaokar, *Loss of  $\pi$ -junction behavior in an interacting impurity Josephson junction*, Physical Review B **61**, 9109 (2000).
- [54] G. Sellier, T. Kopp, J. Kroha, and Y. S. Barash,  *$\pi$  junction behavior and Andreev bound states in Kondo quantum dots with superconducting leads*, Physical Review B **72**, 174502 (2005).
- [55] K. Satori, H. Shiba, O. Sakai, and Y. Shimizu, *Numerical renormalization group study of magnetic impurities in superconductors*, Journal of the Physical Society of Japan **61**, 3239 (1992).





# 3

## FABRICATION OF HYBRID MOLECULAR DEVICES USING MULTI-LAYER GRAPHENE BREAK-JUNCTIONS

*In this chapter we present the first of two platforms developed in this thesis for the study of superconducting phenomena in hybrid molecular devices. We first report on improvements on yield and stability of multi-layer graphene (MLG) electrodes with gold electrodes by patterning a constriction using a helium ion microscope (HIM) or an oxygen plasma etch to fabricate break-junctions. The patterning step allows for the localization of a few-nanometer gap, created by electroburning, that can host single molecules or molecular ensembles. By controlling the width of the sculpted constriction, we regulate the critical power at which the electroburning process begins. We estimate the flake temperature given the critical power and find that at low powers it is possible to electroburn MLG with superconducting contacts in close proximity. In the second part of this chapter, we demonstrate the fabrication of hybrid devices with superconducting contacts and anthracene-functionalized copper curcuminoid molecules as a proof-of-principle for hybrid molecular devices.*

---

Parts of this chapter have been published in *Journal of Physics: Condensed Matter* **26**, 474205 (2014)[1]

### 3.1. INTRODUCTION

IN recent years, molecular electronics has greatly benefited from the fabrication of nanometer spaced gold electrodes in the form of electromigrated and mechanically controllable break-junctions [2–8]. While these advances have led to a wealth of new physics in molecular devices, there are improvements to be made and a continuing focus in the field is toward making robust and reliable contact to single molecules [9]. One recent direction is the use of graphene or multi-layer graphene (MLG) as an electrode and contacting molecules by covalent bonding or  $\pi - \pi$  stacking of aromatic rings [10–13]. This method recently resulted in observation of the gating of a single molecule device at room temperature [14]. While gold atoms are mobile at room temperature [15, 16], MLG can be used as a stable intermediary material to contact molecules. In addition, two-dimensional MLG bridges better the size discrepancy between single molecules and bulky 3D electrodes where screening of the gate can reduce coupling to the molecule. Using MLG as an intermediary material also allows the option of contacting superconducting or ferromagnetic metals without changing the anchoring chemistry of the molecules. This opens the door to the fabrication of hybrid devices to study superconductivity and spintronics in single molecules. Up to now, the added complexity in fabricating hybrid superconducting - molecular devices has kept their exploration to a minimum [17].

In the first part of this chapter we present further steps in the development of MLG electrodes, building on recent reports with gold contacts [14, 18] and improve yield and stability through the localization of a constriction in an exfoliated flake. A predefined constriction using a helium ion microscope (HIM) to mill the flake or an oxygen plasma to etch the flake allows the flexibility to choose the location of a few-nm gap created by a process of electroburning. In comparison with as-exfoliated devices (without a constriction), MLG break-junctions (with a constriction) show a 15% increase in yield due to a reduction in abrupt breaks and reconnected junctions after electroburning [18]. The key to using MLG as opposed to graphene or even few-layer graphene is two-fold: the conductance of MLG is independent of back-gate voltage making electron-transport measurements solely a study of the molecular characteristics of the device and not of the MLG electrodes, and we have found, as detailed in Ref. [18], that the highest yield for nanogap formation is in devices having a resistance of 500  $\Omega$ -1 k $\Omega$  corresponding to devices with a MLG flake of 10 nm thickness with a variation of approximately 5 nm.

In the second part of this chapter we explore the possibility of fabricating hybrid superconducting-molecular devices. The constriction results in a significant reduction in the power required to start the burning process making it possible to fabricate MLG break-junctions with superconducting contacts. We use the superconducting alloy, molybdenum-rhenium (MoRe 60/40) which has a higher melting temperature ( $T_M = 1150$  °C) as compared with commonly used superconductors such as aluminum ( $T_M = 660$  °C) [19]. Out of 26 fabricated MLG break-junctions with MoRe contacts, 16 junctions resulted in tunnel gaps with an average low bias ( $V_b = 10$  mV) resistance of  $17 \pm 11$  G $\Omega$ .

### 3.2. FABRICATION

The fabrication of the devices is accomplished following recent reports [14, 18]. MLG devices are fabricated starting with heavily-doped Si wafers with a 285 nm-thick SiO<sub>2</sub> film.

The Si substrate is used as a gate electrode for three-terminal devices. MLG flakes are deposited by mechanical exfoliation onto the SiO<sub>2</sub> and flakes with a thickness of approximately 10 nm are chosen by their color contrast under an optical microscope. Typical flakes have a deep purple color under white light illumination and a red channel contrast of about 16% (see Appendix). Gold contacts, or MoRe contacts in the case of hybrid devices, are created by patterning with e-beam lithography and thin-film metal deposition.

Electroburning is performed at room temperature and in air. A bias voltage up to 10 V, corresponding to an electric field of more than 10<sup>6</sup> V/m for typical devices, is ramped up across the flake. At large current densities, removal of carbon atoms in the MLG flake occurs due to the interaction with oxygen triggered by the high temperatures of Joule self heating [14, 18]. Feedback controlled software is used to control the voltage across the flake. When the conductance drops by 10% the voltage is swept down at a rate of 0.1 V/ $\mu$ s to arrest the burning process and prevent the formation of a large gap. This cycle continues until the low bias ( $V_b = 10$  mV) resistance is greater than 10 G $\Omega$ , independent of sample geometry. This resistance ensures the electroburning of any last remaining nanometer-sized graphene islands which have been shown to act as large addition energy quantum dots [20]. By controlling the voltage in this way, a gap is burned across the entire flake with a width of a few nanometers at its closest point.

### 3.3. RESULTS

In Figure 3.1 we show the electroburning results of as-exfoliated MLG flakes (without patterning). Figure 3.1(a) shows an atomic force microscopy (AFM) image of a few-micron-wide MLG flake before electroburning. Without localization of a constriction, the electroburning process is believed to most frequently start along the edge of the flake at an unsaturated carbon atom site where a lower displacement energy (7 eV) is required to remove an atom from the lattice as compared to removing a saturated atom from the flake center (30 eV) [21, 22]. In Figure 3.1(b) the resulting few-nm gap is shown near the top of the electrode (white arrow). Electroburning of as-exfoliated flakes often results in gaps with unpredictable locations. Here, the close proximity of the gap to the gold electrode could result in screening of an applied gate field. Ideal devices should have gaps located near the center of the flake where the gate coupling to the molecule is less affected.

In Figure 3.1(c), the critical power required to start the electroburning process for the flake shown in Figure 3.1(a) is plotted along with several other flakes (red circles). Critical powers reach hundreds of mW for the widest flakes and decrease with the flake width. Assuming comparable flake width ( $W$ ) and length ( $L$ ), the critical power as a function of width can be estimated by  $P_c = I_c^2 R = (j_c W t)^2 R_s L / W \approx (j_c t)^2 R_s W^2$ , where we take  $j_c = 5.8 \times 10^7$  A/cm<sup>2</sup> as the average critical current density in these devices [14] and  $R_s = 100$   $\Omega$ /sq as the sheet resistance for MLG [23]. Using these values and an average flake thickness of  $t = 10$  nm, we plot this critical power relation as a dashed line in Figure 3.1(c) where the scatter in the data is mostly due to differences in flake geometry and thickness.

The electroburning is triggered by the high temperatures from Joule heating of the MLG flake. It is interesting to estimate the temperatures reached given the critical power

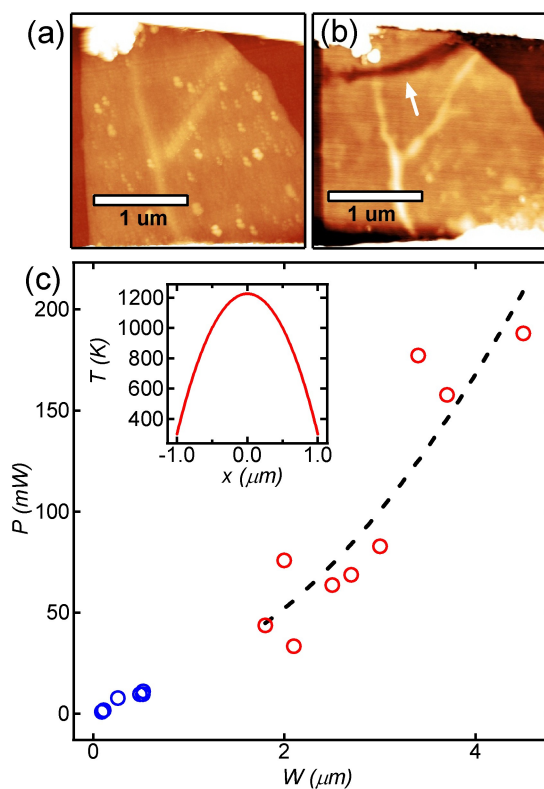


Figure 3.1: (a) AFM image of a MLG device before electroburning. The saturated white regions at the top and bottom are gold electrodes. (b) AFM image of the same MLG flake after electroburning. The gap is seen near the top electrode indicated by a white arrow. (c) Critical power required to start the electroburning vs. the width of the MLG flake. Red circles show the critical powers for as-exfoliated devices. Blue circles show the critical power for pre-patterned break-junction devices using the HIM. The dashed line shows the calculated critical power as a function of width (see text). Inset shows the calculated temperature profile for the widest flake of 4.5 μm.

of the electroburning process for as-exfoliated MLG devices. An estimate of the temperature distribution along the flake (in the direction of current) can be made using the 1D heat equation [24–26]:

$$A \frac{\delta}{\delta x} \left( k \frac{\delta T}{\delta x} \right) + p'_x - g(T - T_0) = 0, \quad (3.1)$$

where  $A = Wt$  is the cross-sectional area of the flake,  $k$  is the thermal conductivity of the MLG flake,  $p'_x$  is the Joule heating rate in watts per unit length, and  $g$  is the thermal conductance to the substrate per unit length and is calculated given the thermal resistance of the SiO<sub>2</sub> and Si substrate beneath the MLG flake ( $g \approx 1/[L(R_{ox} + R_{Si})]$ ), where  $L$  is the length of the flake (in the direction of current),  $R_{ox} = t_{ox}/(k_{ox}WL)$ , where  $k_{ox} = 1.4 \text{ WK}^{-1}\text{m}^{-1}$  and  $R_{Si} = 1/(2k_{Si}(WL)^{1/2})$ , where  $k_{Si} = 50 \text{ WK}^{-1}\text{m}^{-1}$ [25]. Heat convection to air is neglected as the heat convection coefficient for air ( $10 - 100 \text{ Wm}^{-2}\text{K}^{-1}$ ) is four orders of magnitude smaller than the coefficient for heat conduction to the substrate (calculated below).

An analytic solution to the 1D heat equation is arrived at by assuming that  $k$  is constant and that there is a uniform heat generation along the flake given by  $p'_x \approx I^2R/L$ . The temperature in the flake at a position  $x$  along the flake is then given by:

$$T(x) = T_0 + \frac{p'_x}{g} \left( 1 - \frac{\cosh(x/L_H)}{\cosh(L/2L_H)} \right). \quad (3.2)$$

Here,  $T_0 = 300 \text{ K}$ , is the temperature of the electrodes and  $L_H = (kA/g)^{1/2}$  is the characteristic healing length along the flake and is a measure of lateral heat dissipation in the flake. Using Eqn. 3.2, we estimate the critical temperature distribution for the widest as-exfoliated flake in Figure 3.1(c) ( $W = 4.5 \text{ }\mu\text{m}$ ,  $L = 2 \text{ }\mu\text{m}$ ) with a critical power of nearly 190 mW. We take the thermal conductivity of MLG ( $k = 1000 \text{ WK}^{-1}\text{m}^{-1}$ ) which is found for flakes of 8 layers [27]. From the length and width of the flake, we calculate the thermal resistance of the Si substrate  $R_{Si} \approx 3 \times 10^3 \text{ K/W}$ , the thermal resistance of the oxide layer  $R_{ox} \approx 2 \times 10^4 \text{ K/W}$ , the thermal conductance per unit length  $g \approx 19 \text{ WK}^{-1}\text{m}^{-1}$ , and the characteristic healing length for this device,  $L_H = (kA/g)^{1/2} = 1.5 \text{ }\mu\text{m}$ . The healing length is larger than estimates for graphene ( $L_H \approx 0.2 \text{ }\mu\text{m}$  on SiO<sub>2</sub>) due to the thicker cross sectional area[25]. The temperature distribution is plotted in the inset of Figure 3.1(c). The center of the flake is expected to reach temperatures of  $\approx 1200 \text{ K}$ . Typical device dimensions are larger but comparable to the healing length making the 1D diffusion equation a sufficient estimate of the temperature distribution in the flake[25]. A more accurate calculation can be made using finite element methods with COMSOL MULTIPHYSICS v4.3b to account for the small lateral heat dissipation (see Appendix). The high flake temperatures prove detrimental to the fabrication of MLG electrodes with MoRe contacts, demonstrated below. These temperatures can be reduced by pre-patterning the flake to make MLG break-junctions with decreased widths.

The electroburning of MLG break-junctions is first demonstrated with gold contacts in Figure 3.2. Patterning of the MLG devices before electroburning is achieved using a HIM or by oxygen plasma etch. For oxygen plasma etching, we use a pressure of  $50 \text{ }\mu\text{Bar}$  with a flow of  $25 \text{ sccm O}_2$  at  $20 \text{ W}$  power for  $30 \text{ secs}$ . The HIM is well suited for high resolution nanofabrication and unlike oxygen plasma etching, HIM patterning does not re-

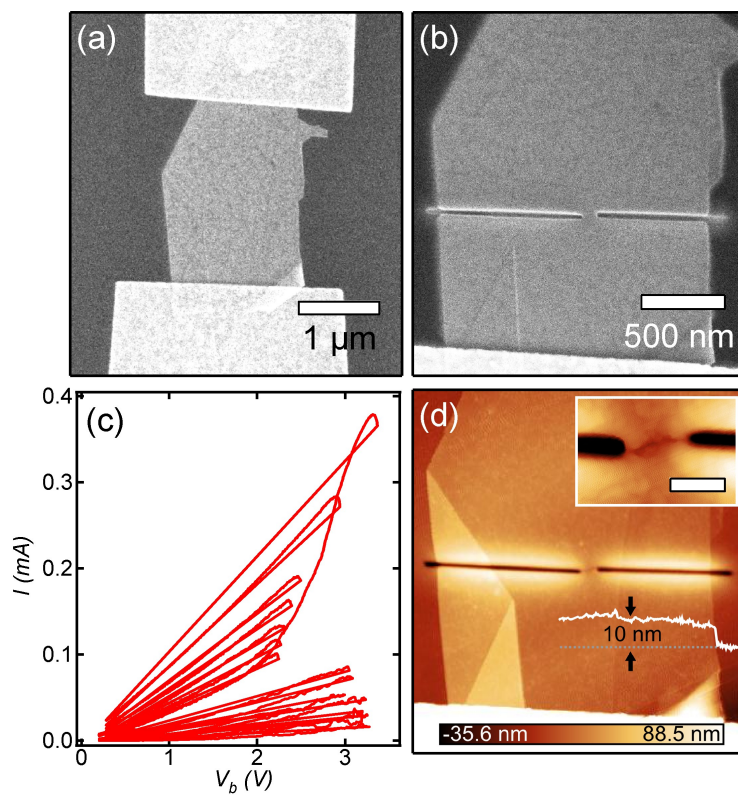


Figure 3.2: (a) Helium ion microscopy (HIM) image of a MLG device before milling between two Au electrodes. (b) HIM image of the same device after milling. The resulting constriction is 100 nm wide. (c)  $I - V_b$  characteristics for the electroburning of the constriction in (b). (d) AFM image of the same device after electroburning. The inset shows the final gap across the constriction. The scale bar is 100 nm.

quire an e-beam lithography step which makes the fabrication process cleaner and faster [28]. In comparison with gallium ion beam milling, HIM patterning allows higher resolution and results in less damage to the Si/SiO<sub>2</sub> substrate [29]. Patterning of graphene using a HIM has been achieved in several forms [30–32]. Here, we use the HIM to position the location of the final few nm gap and reduce the critical power required to burn the remaining constriction. In order to minimize particle contamination of the chip during the milling process, the sample chamber is cleaned overnight with an integrated oxygen plasma cleaner. Imaging of the flake is made with lower magnification in order to prevent damage before milling.

Figure 3.2(a) is a HIM image of a MLG flake with gold electrodes (top and bottom) before milling. This image is used to pattern rectangles that define the areas where the flake will be milled. After defining the milling area, the beam is focused on the edge of the flake and moved to the pattern. For ion beam milling an acceleration voltage of 25 kV is used with a beam current of 1 pA. Typical line doses are about 120 nC/cm. Two rectangular patterns, one on each side of the flake, become 10 nm-wide trenches after direct helium ion beam writing forming the final constriction in the center of the flake. In Figure 3.2(b) we show the device after milling with the HIM. The resulting constriction is about 100 nm wide. The trench width and depth ( $\approx 40$  nm from AFM scan in Figure 3.2(d)) ensure no residual connection between the milled multi-layer graphene edges. While the trench does extend into the oxide, we find no evidence for substrate damage or gate leakage after milling.

After pre-patterning with the HIM, electroburning is performed as before but the constriction results in a significant reduction of the critical power required to start the process. Figure 3.2(c) shows the  $I - V_b$  characteristics of the electroburning process for the patterned device in Figure 3.2(b). The critical power is  $\approx 1$  mW which is more than an order of magnitude smaller than the narrowest as-exfoliated MLG device in Figure 3.1(c). Critical powers for devices with wider pre-patterned constrictions are also shown in Figure 3.1(c) (blue circles). Critical powers steadily increase to 11 mW for constriction widths up to 500 nm. In Figure 3.2(d) we show an AFM image of the device after electroburning. The inset shows the gap formed across the constriction.

We perform electrical measurements at room temperature and in vacuum to characterize the tunnel gap of the MLG break-junctions. In Figure 3.3 we show the  $I - V_b$  and  $I - V_g$  characteristics for two typical devices after electroburning. A tunneling current is measured through the vacuum barrier and shown in Figure 3.3(a) (red and blue circles for devices 1 and 2, respectively). From the tunneling current, we estimate the gap distance using the Simmons model for tunneling through a thin insulating film [14, 33].

$$I_{A,\phi,d}(V) = A \frac{e}{2\pi\hbar d^2} \left( (\phi - \mu_L) e^{-2d \frac{\sqrt{2m(\phi - \mu_L)}}{\hbar}} - (\phi - \mu_R) e^{-2d \frac{\sqrt{2m(\phi - \mu_R)}}{\hbar}} \right) \quad (3.3)$$

Here,  $\phi$  is the potential barrier height,  $A$  is the cross sectional tunneling area,  $d$  is the gap distance, and  $\mu_L = +eV/2$  ( $\mu_R = -eV/2$ ) are the chemical potentials in the left (right) lead. The fit using the Simmons model is plotted (black dashed line) along with the data in Figure 3.3(a) where we have set  $A = 1000$  nm<sup>2</sup> given the cross sectional area of the fabricated constriction ( $W = 100$  nm,  $t = 10$  nm). From the fit, we extract a tunnel gap distance of  $d \approx 2.1$  nm and a barrier height of  $\phi \approx 0.52$  eV for device 1 ( $d \approx 2.1$  nm and  $\phi \approx$

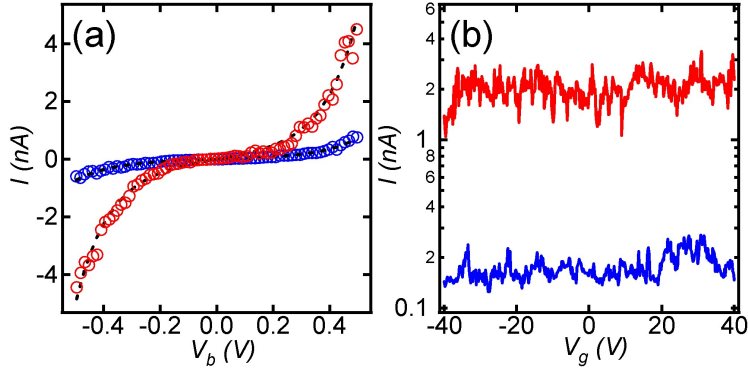


Figure 3.3: Electrical characterization after electroburning for two typical MLG break-junction devices. (a) A characteristic tunneling curve is measured for the device after electroburning (red circles for device 1, blue circles for device 2). The Simmons model fit is plotted along with the tunnel current (black dashed line). (b)  $I - V_g$  characteristics for the devices after electroburning at a bias voltage of 500 mV.

0.65 eV for device 2). The low barrier height, as compared with that of graphene (4.5 eV), is common for the Simmons model when applied to small junctions (e.g. Au nanogaps) but could also include a barrier lowering due to water or OH groups adsorbed at the gap edge [34–36]. While the barrier height has been found to deviate from the expected value, scanning tunneling microscopy studies of Au nanogaps have shown a consistency between the extracted gap size from the Simmons fit and the actual electrode separation [37]. We expect that this is the case for MLG nanogaps as well but further SEM studies should be carried out to verify this. In Figure 3.3(b) we plot the  $I - V_g$  characteristics for the empty tunnel gap at a bias voltage of 500 mV. The current is independent of back-gate voltage.

The high temperatures from electroburning as-exfoliated flakes similar to those in Figure 3.1 are detrimental to the fabrication of MLG break-junctions with superconducting contacts. Moreover, to achieve proximity effect in MLG for hybrid devices, channel lengths of  $< 0.5 \mu\text{m}$  are needed [38]. The combination of high flake temperature and short channel length result in melting of the MoRe alloy for the wider ( $> 3 \mu\text{m}$ ) as-exfoliated devices. This can be seen in Figure 3.4(a) which is an AFM image of an as-exfoliated flake device after electroburning. Deformation of the lower contact can be seen which is near the gap shown in the inset of Figure 3.4(a). By pre-patterning the MLG flake, the electroburning process can be started at much lower critical powers. In Figure 3.4(b) we show an example of an electroburned MLG break-junction patterned by oxygen plasma etch with MoRe contacts. The MoRe contacts are unaffected and the gap can be seen located at the defined constriction in the inset of Figure 3.4(b). In Figures 3.4(c) and 3.4(d) we show the  $I - V_b$ ,  $I - V_g$  characteristics for the MLG electrodes with MoRe contacts shown in Figure 3.4(b). Again, the Simmons model is fit to the tunnel current setting  $A = 800 \text{ nm}^2$  given the cross sectional area of the constriction ( $W = 80 \text{ nm}$ ,  $t = 10 \text{ nm}$ ) and extract a gap distance of  $d \approx 1.6 \text{ nm}$ , a barrier height of  $\phi \approx 1.4 \text{ eV}$ . For the 16 break-junction devices that resulted in tunnel gaps after electroburning, the



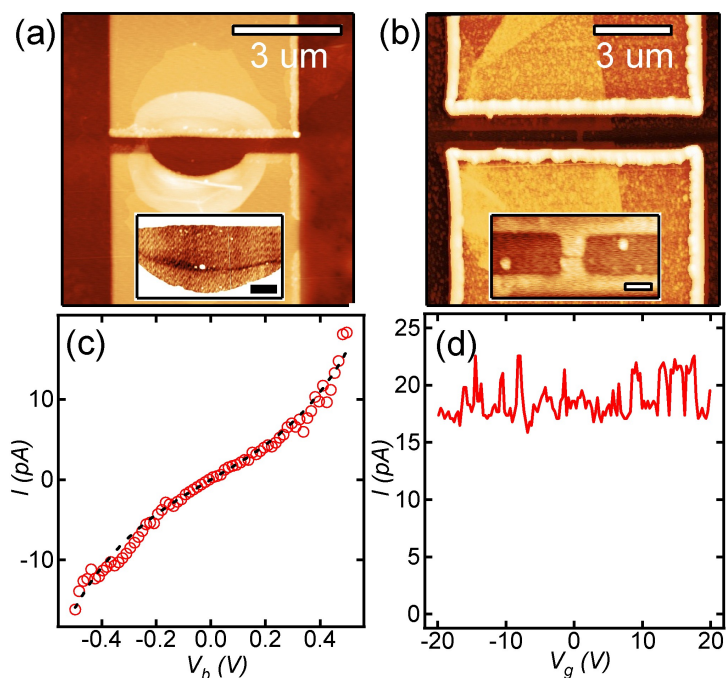


Figure 3.4: Comparison between unpatterned and patterned flakes after electroburning. (a) AFM image of a device without pre patterning. The high temperature of the electroburning process deforms the lower electrode. Inset shows the location of the nanogap near the deformed electrode (scale bar 500 nm). (b) AFM image of an electroburned MLG break-junction pre-patterned using an oxygen plasma etch. The inset shows the resulting constriction from etching (scale bar 100 nm). The width is  $\approx 80$  nm. (c)  $I - V_b$  characteristics of the device in (b) (red circles) as well as a fit of the Simmons model (black dashed line). (d)  $I - V_g$  characteristics of the device in (b) at a bias voltage of 500 mV.

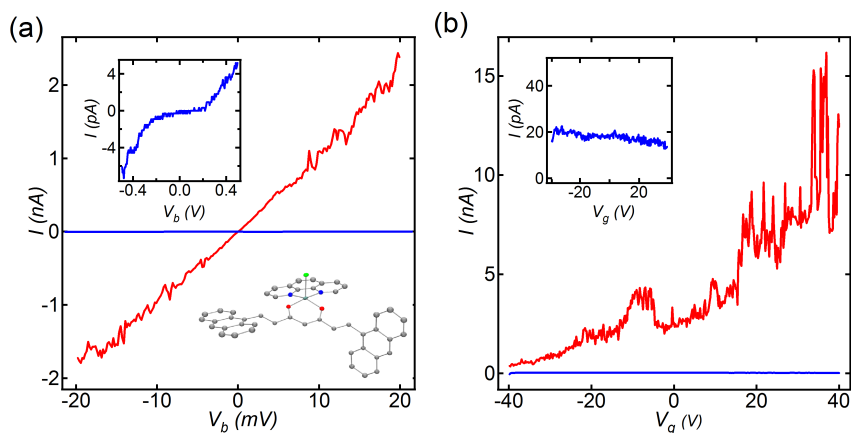


Figure 3.5: MoRe MLG break-junction before and after molecule deposition. (a)  $I - V_b$  characteristics before (top inset) and after molecule deposition. Bottom inset shows the Ortep representation of the copper curcuminoid molecule [(Phen)CuCl(9Accm)]. Phen stands for phenantroline and 9Accm corresponds to the curcuminoid ligand that contains anthracene groups. In the picture the copper atom is in light blue, the carbon atoms are grey, the oxygen atoms are red, the N atoms are blue and the Cl atom is green. Hydrogen atoms are not shown for simplification. (b)  $I - V_g$  characteristics before (inset) and after molecule deposition. The  $I - V_b$  and  $I - V_g$  characteristics before deposition are also plotted in the main panel of (b) and (c) (blue lines) for comparison.

average tunnel gap from the Simmons fit is  $2.1 \pm 0.3$  nm and the average barrier height is  $0.89 \pm 0.3$  eV.

To demonstrate the fabrication of hybrid devices, we have performed deposition of anthracene-functionalized copper curcuminoid molecules ((Phen)CuCl(9Accm)) on the MoRe MLG break-junctions [39]. The bottom inset of Figure 3.5(a) shows a scheme of the molecule. Contact to the molecule is mediated through the interaction of two  $\pi$ -systems; the  $\pi$ -conjugated system of the anthracene groups on the molecule and that of the MLG flake. For deposition, a powder of synthesized molecules is dissolved in dichloromethane ( $\text{CH}_2\text{Cl}_2$ ) at a concentration of 0.1 mM. The electroburned junctions are kept in the solution for 30 mins which results in a sub-monolayer of molecules on the surface of the Si/SiO<sub>2</sub> substrate [14]. Of the remaining sixteen tunnel junctions after electroburning, one junction showed a significant change in the  $I - V_b$  and  $I - V_g$  characteristics after deposition. The top inset of Figure 3.5(a) shows the tunneling characteristics of the junction (low bias resistance of 14 G $\Omega$ ) and the inset of Figure 3.5(b) shows that the current is virtually independent of gate voltage before deposition. After deposition, the  $I - V_b$  characteristics become linear and the low bias resistance is 9 M $\Omega$ . In addition, the current shows a strong dependence on gate voltage, changing by two orders of magnitude over 80 Volts applied to the back-gate. To ascertain the presence of a single molecule or a few molecules in the junction, further transport measurements can be performed at low temperature.

In conclusion, we have studied the yield and stability of MLG break-junctions with gold electrodes and extended the fabrication for use in hybrid molecular devices. Using

HIM milling or an oxygen plasma etch to localize a constriction in the MLG flake, we control the position of a few nm gap created by electroburning. The critical power needed to start the electroburning process can be controlled by the width of the constriction. For lower powers ( $\approx 1$  mW), we fabricate MLG break-junctions with MoRe contacts and present a proof-of-principle hybrid device using anthracene-functionalized copper curcuminoid molecules.

### 3.4. OBSTACLES AND OUTLOOK

As this hybrid device architecture was not pursued after initial investigations it seems appropriate to document several obstacles that slowed further progress and comment on possible directions for advancement.

Low temperature transport measurements of unpatterned and unburned multi-layer graphene flakes revealed that a significant fraction (30%) of the devices did not present a supercurrent. This is most likely due to an interfacial barrier between the flake and the MoRe electrodes which could be reduced with a high temperature anneal. For the devices that did present Josephson supercurrents at low temp, the supercurrent was gate tunable. Figure 3.6 shows ( $I - V$ ) characteristics as a function of back gate for two representative devices. In the Figures 3.6(a) and (b) we show low temperature (700 mK) measurements for a unpatterned multi-layer flake with MoRe electrodes. A critical current of  $\approx 200$  nA is observed. The supercurrent is gate tunable, see 3.6, which is not expected for a 10 nm flake as the screening length in few-layer flakes is roughly 2 to 3 layers[40, 41]. It is hypothesized in similar experiments that the supercurrent flows through the bottom layers of the flake[42–44]. This points to the added complexity involved in creating hybrid devices from multi-layer graphene flakes.

Further complications arose as all devices patterned with a constriction did not show the presence of a supercurrent at low temperatures. Figure 3.6(c) shows an  $I - V$  curve for a patterned device (without a nanogap) at a temperature of 50 mK. Even with modulation of the carrier density with a gate voltage, no supercurrent was apparent in any device, see 3.6(d). Furthermore, all patterned devices show a periodic modulation of the conductance through the flake which is reminiscent of gate modulated Fabry-Perot oscillations in 1D systems and constrictions in graphene[45–47].

Around the time of these experiments, progress on the second device platform incorporating gold nanowires (chapter 4 advanced quickly. For these reasons, the graphene devices were not further explored but it is clear from these initial low temperature results on patterned devices, further measurements are required to elucidate the low temperature properties of the multi-layer graphene junctions. In particular detailed measurements of the voltage carrying state (similar to those performed in chapter 6 would help better understand the proximity effect in these devices.

## 3.5. APPENDIX

### 3.5.1. CONTRAST PROFILES FOR A TYPICAL MLG FLAKE

In Figure 3.7 we show an optical image of a typical flake along with the respective green, blue and red channel data. Figure 3.7(e) shows the contrast profiles for each channel. Flakes of 10 nm thickness typically have red channel contrasts of about 16%.

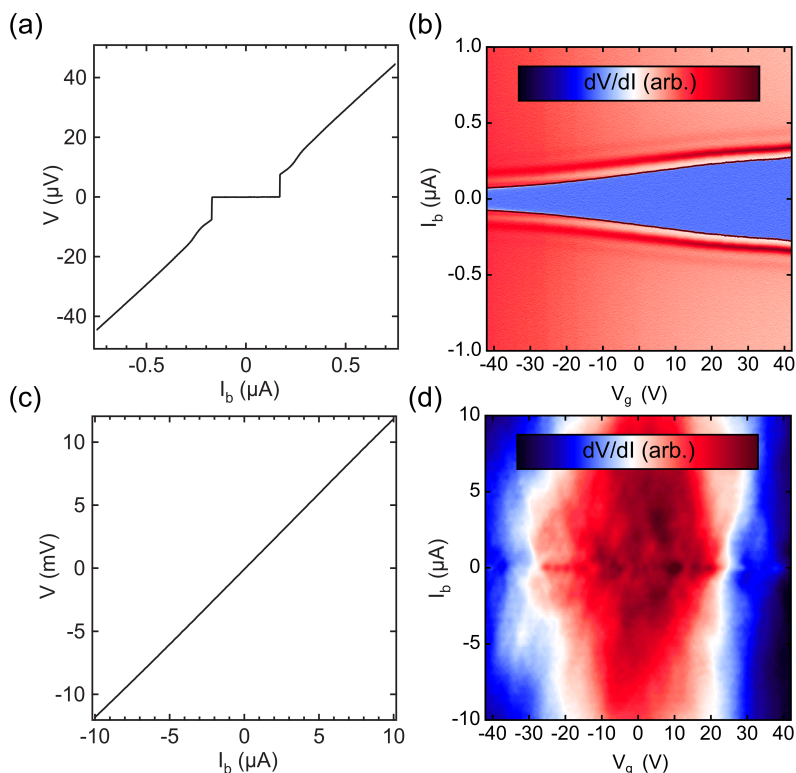


Figure 3.6: (a) Low temperature (700 mK), four terminal measurement of a multi-layer graphene flake with MoRe electrodes. (b) Low temperature (700 mK), four terminal measurement of the same device in (a) as a function of gate. (c) Low temperature (50 mK), four terminal measurement of an oxygen plasma etched flake. (d) Low temperature (50 mK), four terminal measurement of the same device in (a) as a function of gate.

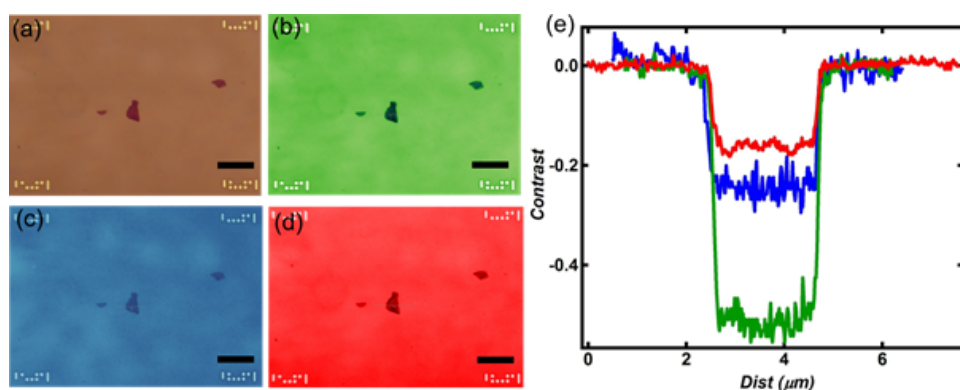


Figure 3.7: (a) Optical image of a typical flake on Si/SiO<sub>2</sub> substrate. Green (b), blue (c), and red (d) channel images of the optical image in (a). (e) Contrast profiles taken from line cuts in panels (b), (c), and (d) corresponding to the green, blue, and red channels respectively.

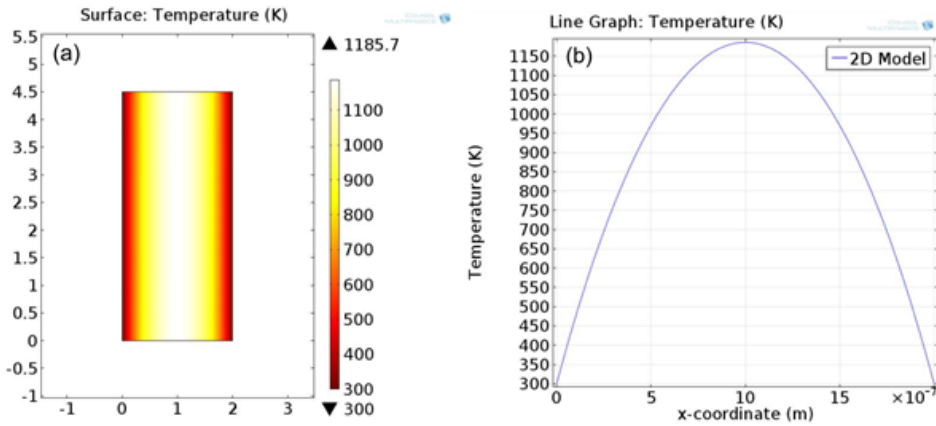


Figure 3.8: (a) 2D temperature distribution across flake. (b) line profile taken across the length of the flake.

### 3.5.2. FINITE ELEMENTS CALCULATION USING COMSOL

Using the heat transfer in solids module, we estimate the maximum temperature for the widest as-exfoliated device during electroburning in the main text. We use a uniform heat source and out-of-plane convection to simulate heat dissipation to the substrate. Figure 3.8(a) shows the 2D temperature distribution across the flake ( $W=4.5 \mu\text{m}$ ,  $L=2 \mu\text{m}$ ). Figure S1(b) shows a line profile taken across the length of the flake. Using COMSOL we estimate a maximum temperature of 1186 K while the 1D heat equation in the main text estimates a maximum temperature of 1227 K, a 3% difference.

## REFERENCES

- [1] J. O. Island, A. Holovchenko, M. Koole, P. F. A. Alkemade, M. Menelaou, N. Aliaga-Alcalde, E. Burzuri, and H. S. J. van der Zant, *Fabrication of hybrid molecular devices using multi-layer graphene break junctions*, *Journal of Physics: Condensed Matter* **26**, 474205 (2014).
- [2] M. A. Reed, C. Zhou, C. J. Muller, T. P. Burgin, and J. M. Tour, *Conductance of a molecular junction*, *Science* **278**, 252 (1997).
- [3] H. Park, A. K. L. Lim, A. P. Alivisatos, J. Park, and P. L. McEuen, *Fabrication of metallic electrodes with nanometer separation by electromigration*, *Applied Physics Letters* **75**, 301 (1999).
- [4] C. Kergueris, J.-P. Bourgoin, S. Palacin, D. Esteve, C. Urbina, M. Magoga, and C. Joachim, *Electron transport through a metal-molecule-metal junction*, *Physical Review B* **59**, 12505 (1999).
- [5] H. Park, J. Park, A. K. Lim, E. H. Anderson, A. P. Alivisatos, and P. L. McEuen, *Nanomechanical oscillations in a single-C<sub>60</sub> transistor*, *Nature* **407**, 57 (2000).
- [6] R. H. M. Smit, Y. Noat, C. Untiedt, N. D. Lang, M. C. Van Hemert, and J. M. Van Ruitenbeek, *Measurement of the conductance of a hydrogen molecule*, *Nature* **419**, 906 (2002).
- [7] J. Park, A. N. Pasupathy, J. I. Goldsmith, C. Chang, Y. Yaish, J. R. Petta, M. Rinkoski, J. P. Sethna, H. D. Abruña, P. L. McEuen, *et al.*, *Coulomb blockade and the Kondo effect in single-atom transistors*, *Nature* **417**, 722 (2002).
- [8] N. J. Tao, *Electron transport in molecular junctions*, *Nature Nanotechnology* **1**, 173 (2006).
- [9] E. Lörtscher, *Wiring molecules into circuits*, *Nature Nanotechnology* **8**, 381 (2013).
- [10] S. Bailey, D. Visontai, C. J. Lambert, M. R. Bryce, H. Frampton, and D. Chappell, *A study of planar anchor groups for graphene-based single-molecule electronics*, *The Journal of Chemical Physics* **140**, 054708 (2014).
- [11] V. M. García-Suárez, R. Ferradás, D. Carrascal, and J. Ferrer, *Universality in the low-voltage transport response of molecular wires physisorbed onto graphene electrodes*, *Physical Review B* **87**, 235425 (2013).
- [12] G. Wang, Y. Kim, M. Choe, T.-W. Kim, and T. Lee, *A new approach for molecular electronic junctions with a multilayer graphene electrode*, *Advanced Materials* **23**, 755 (2011).
- [13] Y. Cao, S. Dong, S. Liu, L. He, L. Gan, X. Yu, M. L. Steigerwald, X. Wu, Z. Liu, and X. Guo, *Building high-throughput molecular junctions using indented graphene point contacts*, *Angewandte Chemie* **124**, 12394 (2012).

- [14] F. Prins, A. Barreiro, J. W. Ruitenber, J. S. Seldenthuis, N. Aliaga-Alcalde, L. M. K. Vandersypen, and H. S. J. van der Zant, *Room-temperature gating of molecular junctions using few-layer graphene nanogap electrodes*, Nano Letters **11**, 4607 (2011).
- [15] F. Prins, T. Hayashi, B. J. A. de Vos van Steenwijk, B. Gao, E. A. Osorio, K. Muraki, and H. S. J. van der Zant, *Room-temperature stability of Pt nanogaps formed by self-breaking*, Applied Physics Letters **94**, 123108 (2009).
- [16] D. R. Strachan, D. E. Smith, M. D. Fischbein, D. E. Johnston, B. S. Guiton, M. Drndić, D. A. Bonnell, and A. T. Johnson, *Clean electromigrated nanogaps imaged by transmission electron microscopy*, Nano Letters **6**, 441 (2006).
- [17] C. B. Winkelmann, N. Roch, W. Wernsdorfer, V. Bouchiat, and F. Balestro, *Superconductivity in a single-C<sub>60</sub> transistor*, Nature Physics **5**, 876 (2009).
- [18] E. Burzurí, F. Prins, and H. S. van der Zant, *Characterization of nanometer-spaced few-layer graphene electrodes*, Graphene **1**, 26 (2012).
- [19] M. J. Witcomb and D. Dew-Hughes, *The  $\sigma$ -phase in molybdenum-rhenium; microstructure and superconducting hysteresis*, Journal of the Less Common Metals **31**, 197 (1973).
- [20] A. Barreiro, H. S. J. van der Zant, and L. M. K. Vandersypen, *Quantum dots at room temperature carved out from few-layer graphene*, Nano Letters **12**, 6096 (2012).
- [21] A. Barreiro, F. Börrnert, M. H. Rummeli, B. Büchner, and L. M. K. Vandersypen, *Graphene at high bias: Cracking, layer by layer sublimation, and fusing*, Nano Letters **12**, 1873 (2012).
- [22] J. H. Warner, M. H. Rummeli, L. Ge, T. Gemming, B. Montanari, N. M. Harrison, B. Büchner, and G. A. D. Briggs, *Structural transformations in graphene studied with high spatial and temporal resolution*, Nature Nanotechnology **4**, 500 (2009).
- [23] J.-U. Park, S. Nam, M.-S. Lee, and C. M. Lieber, *Synthesis of monolithic graphene-graphite integrated electronics*, Nature Materials **11**, 120 (2012).
- [24] E. Pop, *Energy dissipation and transport in nanoscale devices*, Nano Research **3**, 147 (2010).
- [25] M.-H. Bae, Z.-Y. Ong, D. Estrada, and E. Pop, *Imaging, simulation, and electrostatic control of power dissipation in graphene devices*, Nano Letters **10**, 4787 (2010).
- [26] S. Yiğen, V. Tayari, J. O. Island, J. M. Porter, and A. R. Champagne, *Electronic thermal conductivity measurements in intrinsic graphene*, Phys. Rev. B **87**, 241411 (2013).
- [27] S. Ghosh, W. Bao, D. L. Nika, S. Subrina, E. P. Pokatilov, C. N. Lau, and A. A. Balandin, *Dimensional crossover of thermal transport in few-layer graphene*, Nature Materials **9**, 555 (2010).

- [28] P. F. A. Alkemade, E. M. Koster, E. van Veldhoven, and D. J. Maas, *Imaging and nanofabrication with the helium ion microscope of the Van Leeuwenhoek Laboratory in Delft*, Scanning **34**, 90 (2012).
- [29] D. C. Bell, M. C. Lemme, L. A. Stern, J. R. Williams, and C. M. Marcus, *Precision cutting and patterning of graphene with helium ions*, Nanotechnology **20**, 455301 (2009).
- [30] S. Boden, Z. Moktadir, D. Bagnall, H. Mizuta, and H. Rutt, *Focused helium ion beam milling and deposition*, Microelectronic Engineering **88**, 2452 (2011).
- [31] M. C. Lemme, D. C. Bell, J. R. Williams, L. A. Stern, B. W. H. Baugher, P. Jarillo-Herrero, and C. M. Marcus, *Etching of graphene devices with a helium ion beam*, ACS Nano **3**, 2674 (2009).
- [32] Y. Zhou and K. P. Loh, *Making patterns on graphene*, Advanced Materials **22**, 3615 (2010).
- [33] J. G. Simmons, *Generalized formula for the electric tunnel effect between similar electrodes separated by a thin insulating film*, Journal of Applied Physics **34**, 1793 (1963).
- [34] A. Mangin, A. Anthore, M. L. Della Rocca, E. Boulat, and P. Lafarge, *Reduced work functions in gold electromigrated nanogaps*, Physical Review B **80**, 235432 (2009).
- [35] K. S. Curtis, C. J. Ford, D. Anderson, H. E. Beere, I. Farrer, D. A. Ritchie, and G. A. C. Jones, *Reduced tunnel-barrier height in sub-10 nm Au nanoelectrodes*, in *Nanotechnology (IEEE-NANO), 2012 12th IEEE Conference on* (IEEE, 2012) pp. 1–9.
- [36] W. Wang and Z. Li, *Potential barrier of graphene edges*, Journal of Applied Physics **109**, 114308 (2011).
- [37] P. Steinmann and J. M. R. Weaver, *Fabrication of sub-5nm gaps between metallic electrodes using conventional lithographic techniques*, Journal of Vacuum Science & Technology B **22**, 3178 (2004).
- [38] A. Kanda, T. Sato, H. Goto, H. Tomori, S. Takana, Y. Ootuka, and K. Tsukagoshi, *Dependence of proximity-induced supercurrent on junction length in multilayer-graphene Josephson junctions*, Physica C: Superconductivity **470**, 1477 (2010).
- [39] N. Aliaga-Alcalde, P. Marqués-Gallego, M. Kraaijkamp, C. Herranz-Lancho, H. den Dulck, H. Gorner, O. Roubeau, S. J. Teat, T. Weyhermüller, and J. Reedijk, *Copper curcuminoids containing anthracene groups: fluorescent molecules with cytotoxic activity*, Inorganic Chemistry **49**, 9655 (2010).
- [40] F. Guinea, *Charge distribution and screening in layered graphene systems*, Physical Review B **75**, 235433 (2007).
- [41] H. Miyazaki, S. Odaka, T. Sato, S. Tanaka, H. Goto, A. Kanda, K. Tsukagoshi, Y. Ootuka, and Y. Aoyagi, *Inter-layer screening length to electric field in thin graphite film*, Applied Physics Express **1**, 034007 (2008).



- [42] T. Sato, A. Kanda, T. Moriki, H. Goto, S. Tanaka, Y. Ootuka, H. Miyazaki, S. Odaka, K. Tsukagoshi, and Y. Aoyagi, *A different type of reentrant behavior in superconductor/thin graphite film/superconductor Josephson junctions*, *Physica C: Superconductivity* **468**, 797 (2008).
- [43] T. Sato, T. Moriki, S. Tanaka, A. Kanda, H. Goto, H. Miyazaki, S. Odaka, Y. Ootuka, K. Tsukagoshi, and Y. Aoyagi, *Gate-controlled superconducting proximity effect in ultrathin graphite films*, *Physica E: Low-dimensional Systems and Nanostructures* **40**, 1495 (2008).
- [44] A. Kanda, T. Sato, H. Goto, H. Tomori, S. Takana, Y. Ootuka, and K. Tsukagoshi, *Dependence of proximity-induced supercurrent on junction length in multilayer-graphene josephson junctions*, *Physica C: Superconductivity* **470**, 1477 (2010).
- [45] W. Liang, M. Bockrath, D. Bozovic, J. H. Hafner, M. Tinkham, and H. Park, *Fabry-Perot interference in a nanotube electron waveguide*, *Nature* **411**, 665 (2001).
- [46] A. V. Kretinin, R. Popovitz-Biro, D. Mahalu, and H. Shtrikman, *Multimode fabry-perot conductance oscillations in suspended stacking-faults-free InAs nanowires*, *Nano Letters* **10**, 3439 (2010).
- [47] P. Gehring, H. Sadeghi, S. Sangtarash, C. S. Lau, J. Liu, A. Ardavan, J. H. Warner, C. J. Lambert, G. A. D. Briggs, and J. A. Mol, *Quantum interference in graphene nanoconstrictions*, *Nano Letters* **16**, 4210 (2016).



# 4

## SUPERCONDUCTING MOLYBDENUM-RHENIUM ELECTRODES FOR SINGLE-MOLECULE TRANSPORT STUDIES

*In this chapter we present the second platform developed for the study of superconducting phenomena in hybrid molecular devices. We first demonstrate that electronic transport through single molecules or molecular ensembles, commonly based on gold (Au) electrodes, can be performed with superconducting electrodes by combining gold with molybdenum-rhenium (MoRe). This combination induces proximity-effect superconductivity in the gold to temperatures of at least 4.6 Kelvin and magnetic fields of 6 Tesla, improving on previously reported aluminum based superconducting nanojunctions. As a proof of concept, we show three-terminal superconducting transport measurements through an individual Fe<sub>4</sub> single-molecule magnet.*

---

Parts of this chapter have been published in Applied Physics Letters **106**, 222602 (2015)[1]

## 4.1. INTRODUCTION

RECENT advances in nanoscale fabrication techniques have made it possible to couple superconducting electrodes with confined systems of electrons. From this combination, interesting phenomena like Andreev reflections [2] and Yu-Shiba-Rusinov states [3–6] emerge where superconductivity can be used alternatively as a probe to characterize a mesoscopic system [7] or as a tool to influence it [8–10]. When the confined system is an individual molecule or a nanocrystal, additional internal degrees of freedom like spin and vibrations are predicted to have an effect on the Cooper pair transport. For instance, supercurrent can be employed as a probe for isotropic and anisotropic spinful molecules [11, 12].

So far, only a handful of studies have investigated superconducting transport through individual molecules. Two recent examples are scanning tunneling microscopy studies using lead [10, 13] and two-terminal devices using tungsten [14]. However, due to the absence of a gate, these studies are limited to the off-resonant transport regime and a single fixed charge state. Further studies, involving a combination of resonant transport and superconductivity, are based on electromigrated gold break junctions [15]. These junctions are equipped with a gate electrode in close proximity to the molecule thereby forming a single-molecule transistor. Due to the difficulty of electromigrating materials other than gold, superconductivity is typically induced by proximity to a superconducting material like aluminum [16]. The small superconducting gap of aluminum ( $\Delta \approx 0.18$  meV,  $T_c \approx 1.2$  K,  $B_c \approx 10$  mT), however, limits the range of operation in magnetic field and temperature. In particular, the conditions for attaining the intermediate coupling transport regime ( $\Gamma \sim \Delta \sim k_B T_K$ ) restrict the range of molecular couplings  $\Gamma$  and Kondo energy scales  $k_B T_K$ . As a consequence limited room is left for the investigation of this intriguing regime where single-electron and many-body physics are directly competing [8, 9, 17, 18].

In this chapter, we present a three-terminal hybrid electromigrated break-junction, a SN-I-NS junction, that employs molybdenum-rhenium [19] (MoRe) as the superconducting material (S) and gold as the normal metal (N). Gold allows for the creation of nanogaps (I) by electromigration and is commonly used for contacting single molecules due to its nearly ideal Fermi gas-like density of states (DOS), as well as inertness and compatibility with organic ligand terminations. When in contact with MoRe (60/40 alloy,  $\Delta_{BCS} \approx 1.4$  meV,  $\xi \approx 20$  nm [19]), we find that the gold junction exhibits a proximitized gap of about 0.7 meV. We characterize transport through these hybrid electromigrated junctions as a function of temperature and magnetic field. We demonstrate superconducting behavior up to at least a temperature of 4.6 K and a magnetic field of 6T. We show preliminary transport measurements resulting from coupling a fabricated superconducting junction to an individual  $\text{Fe}_4$  single molecule magnet (SMM).

## 4.2. FABRICATION

The fabrication of the three-terminal device follows the procedure by Osorio *et al.* [20] and only the relevant differences are described here. Conventional e-beam lithography and evaporation techniques are employed to fabricate the nanostructure. A scanning electron microscope (SEM) image of the device is shown in Figure 4.1(a) and a corre-

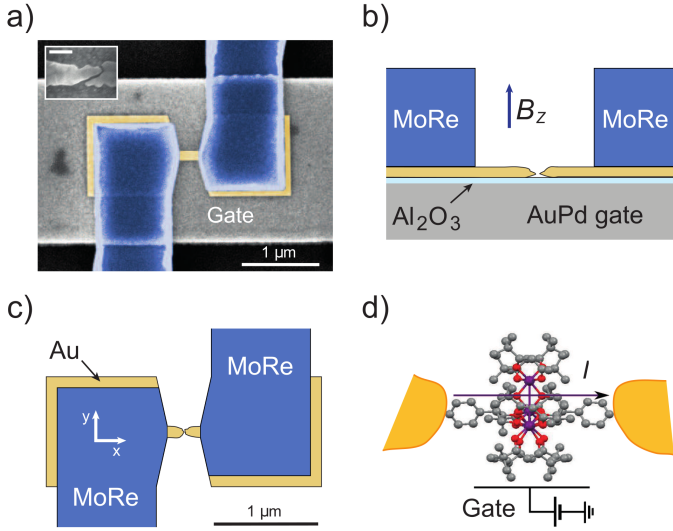


Figure 4.1: **The three-terminal hybrid MoRe-Au superconducting nanojunction.** (a) Scanning electron microscope (SEM) image of a three-terminal superconducting SNS junction (false colored) before electromigration. The two MoRe patches (blue), acting as source and drain superconducting reservoirs, are in contact with the Au nanoribbon (yellow). The narrow part of the nanoribbon forms the nanowire to be electromigrated. An SEM image of an electromigrated junction is shown in the inset (100 nm scale bar). The z-axis is along the out-of-plane direction. (b) Side view schematics of an electromigrated junction. (c) Top view of (b). The x and y-axes are indicated. (d) Ideal arrangement of Fe<sub>4</sub> molecule between source and drain electrodes forming the three-terminal superconducting molecular transistor.

sponding side-view schematic is shown in Figure 4.1(b). The stack consists of a 75 nm gold-palladium (AuPd) gate coated with 7 nm of atomic layer deposition-grown aluminum oxide (Al<sub>2</sub>O<sub>3</sub>) on top of which the thin gold wire is deposited. Two MoRe superconducting contacts (110 nm-thick) partially overlap the gold wire, leaving a narrow, rectangular portion uncovered. This 260 nm-long and 100 nm-wide bridge forms the nanowire in which a nanogap is subsequently produced by room-temperature electromigration [21] and self-breaking [20]. In this method, a real-time feedback-controlled current of electrons is passed through the nanowire and used to displace the gold atoms (for the electromigration curve of a characteristic device see the section 4.4.1 of the Appendix). This process allows the formation of the SN-I-NS junctions, where the vacuum nanogap corresponds to the insulator sandwiched between the two gold portions of the normal wire and the MoRe superconducting patches. In the inset of Figure 4.1(a) a SEM image of an electromigrated nanowire is shown.

The electromigrated SN-I-NS junctions are cooled down in a dilution fridge ( $T \approx 20$  mK) equipped with a vector magnet. Temperature and magnetic field measurements are performed in a two-probe voltage-bias scheme, i.e. by applying a source-drain DC bias voltage ( $V$ ) and measuring the resulting current ( $I$ ). The differential conductance

spectrum  $dI/dV$  versus  $V$  is then obtained by taking a numerical derivative. A three-terminal measurement as a function of gate voltage ( $V_{\text{gate}}$ ) and bias voltage is carried out to check for the absence of any gating and/or Coulomb blockade effect, see Appendix section 4.4.1 for an example plot.

In Figure 4.2(a)  $dI/dV$  spectra as a function of temperature are shown. The low-temperature  $dI/dV$  trace ( $T = 100 \text{ mK} \ll T_c$ ) shows a V-shaped dip between two symmetric peaks at bias voltages  $2V_{\text{gap}} = \pm 1.4 \text{ mV}$ . At higher biases, the conductance smoothly decreases to a plateau value, which we interpret as the normal state resistance regime. Increasing the temperature up to about 1.2 K is seen to only slightly affect the conductance at low voltage. In contrast, an increase in temperature from 2 K up to 3.1 K and further, results in a softening of the dip and a lowering of the two peaks, leaving the higher bias conductance unchanged throughout. Prominently, a residual dip is maintained up to the highest measured temperature of 4.6 K.

The presence of a reduced gap-like structure in bias voltage with characteristic energy  $E_{\text{gap}} < \Delta_{\text{BCS}}$  is a well-known signature of proximity-induced superconductivity [22]. This effect has been already experimentally observed, among others, in Scheer *et al.* [16], Gueron *et al.* [23] and theoretically investigated in detail by several authors [24, 25]. In these previous experiments as well as in the one discussed here, the superconducting coherence length  $\xi$  compares with the characteristic lengths of the gold normal metal portion as  $\xi, L \gg l_e \gg \lambda_F$ , where  $L$  is the length of the bridge,  $l_e$  and  $\lambda_F$  are the elastic scattering length and Fermi wavelength respectively. This situation is called the quasi-classical diffusive limit for which the theory has been formulated by Usadel [26]. A spatially-dependent density of states along with a reduced gap  $E_{\text{gap}}(L) < \Delta$  arises from an application of the model to a N film of finite length  $L$  connected to a superconductor. Within this framework, the peaks and the dip in the  $dI/dV$  spectra observed in this experiment result from the convolution of the superconducting peaks and the reduced gap in the proximity-induced DOS at the two N-I interfaces.

We also investigate the persistence of superconductivity upon application of an external magnetic field for different spatial directions. Figure 4.2(b) shows the differential conductance spectra as a function of a field along the  $z$ -axis, i.e. perpendicular to the plane of the nanostructure (see Figure 4.1(b)). A gradual decrease of the characteristic features is observed up to 1 T. For higher magnetic field values a further decrease is accompanied by a complete suppression of the peaks at  $\pm 1.4 \text{ mV}$ . A dip is present at the highest  $B$ -field value of 6 T signaling the presence of a residual superconducting DOS. Measurements with equivalent magnetic field intensities but along the  $y$ -axis, i.e. in-plane and perpendicular to the transport direction, are performed and the results displayed in Figure 4.2(c). The softening of the dip and the coherence peaks for increasing magnetic fields is also observed. However, the spectra for the  $y$ -axis field maintain stronger superconducting features as compared to those of Figure 4.2(b) for corresponding magnetic field values. Equivalently, the magnetic field  $B_y$  acts comparatively weaker than  $B_z$  in suppressing the proximity-effect superconductivity. In analogy with the temperature-dependent measurements, we note that the high-bias regions ( $eV > 2E_{\text{gap}}$ ) of the spectra are not affected by variations of the magnetic field.

The experimental magnetic field dependences can also be qualitatively explained within the diffusive Usadel framework. As shown in Belzig *et al.* [25], the applied mag-

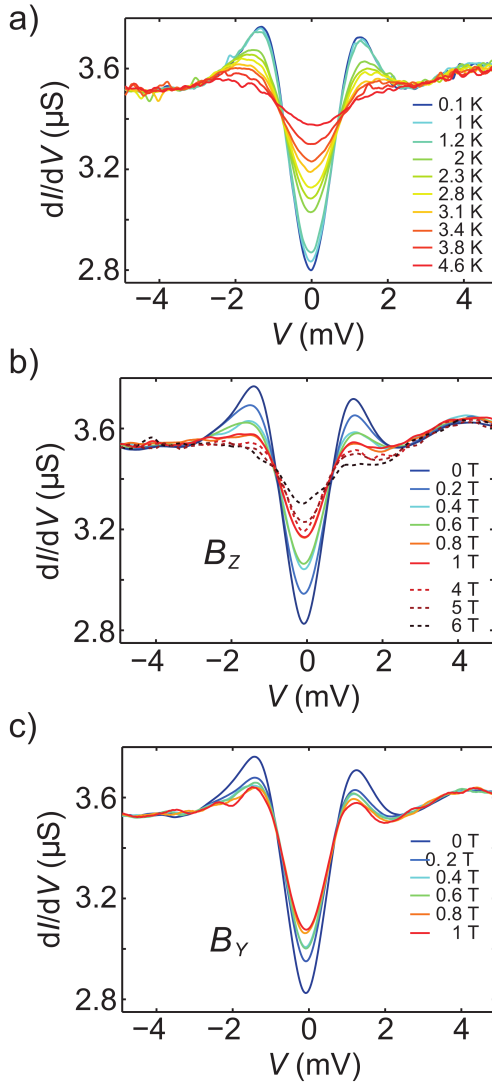


Figure 4.2: **Temperature and magnetic field voltage-bias characterization of the superconductivity.** (a) Differential conductance spectra measured as a function of temperature ranging from 100 mK to 4.6 K. The characteristic gapped structure of the superconductive DOS persists up to above liquid-He temperature. (b) Differential conductance traces measured as a function of the magnetic field along the z-axis at base temperature  $T \approx 22$  mK. The dashed lines indicate the high magnetic field measurements. The signature of the superconducting gap is evident up to above a magnetic field  $B_z = 6$  T. (c) Same as (b) but with the magnetic field pointing along the y-axis. The solid lines indicate magnetic fields ranging from  $B_y = 0$  T to  $B_y = 1$  T. The characteristic peaks and the gap softens comparatively slower than in (b). Note that the vector magnet that we employed is limited to a magnetic field of 1 T along the y-axis.

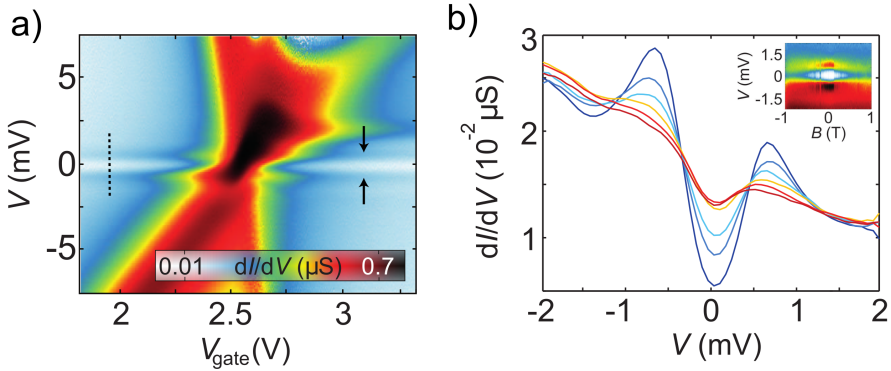


Figure 4.3: **The superconducting single-molecule transistor.** (a) Differential conductance map as a function of gate and bias voltages measured at  $B = 0$  T and  $T = 0.6$  K. Superconductivity and Coulomb blocked transport superimpose in the two stable charged states. The horizontal lines of increased conductance (marked by black arrows) and the low-bias dip indicate the superconducting DOS of the leads. At the charge degeneracy point ( $V_g \approx 2.5$  V) the superconducting gap is lifted and the conductance greatly increases. (b) Differential conductance spectra as a function of magnetic field and bias voltage at fixed gate voltage  $V_{\text{gate}} = 1.95$  V (dashed line in the left stable charge state of (a)). The spectra are extracted from the map in the inset, starting from  $B = 0$  T (blue line) to  $B = 1$  T (red line) at a regular spacing  $\Delta B = 0.2$  T. A weak trace of the gapped DOS is still visible at  $B = 1$  T.

netic field can be incorporated into an effective pair breaking rate  $\Gamma_{\text{eff}}$  that affects the magnitude of the coherence peaks and the reduced gap energy. This pair breaking mechanism is proportional to the intensity of the magnetic field vector,  $|B|$ , as well as the dimension of the nanowire transverse to it,  $W$ , ( $\Gamma_{\text{eff}} \sim B^2 W^2$ ). In the present situation, the transverse directions corresponding to the magnetic fields  $B_z$  and  $B_y$  are the nanowire width and thickness, respectively. This would result in a stronger pair breaking effect along the  $z$ -axis as compared to the  $y$ -axis ( $\Gamma_{\text{eff}}^z / \Gamma_{\text{eff}}^y \sim 100$ ), qualitatively consistent with the experimental observations (for an additional sample see the Appendix section 4.4.2). We note that the persistence to high-magnetic fields can be partially ascribed to junction shape and/or geometry effects.

Envisioning the use of our hybrid junctions as a superconducting molecular transistor, we present here preliminary results obtained from coupling an individual  $\text{Fe}_4$  single-molecule magnet [27] (SMM) to superconducting leads (schematically shown in Figure 4.1(d)). Figure 4.3(a) displays the differential conductance map of an individual  $\text{Fe}_4$ -SMM as a function of gate and bias voltages for an external magnetic field  $B = 0$  T. The standard features of sequential electron tunneling and Coulomb-blockade are seen. Each of the two low-conductance regions on either side of the charge degeneracy point ( $V_{\text{gate}} \approx 2.5$  V,  $V \approx 0$  V) corresponds to a stable charge state. Within these regions, the dip and the horizontal lines of increased conductance centered around zero-bias (black arrows) signal the expected superconducting density of states of the two leads. At the degeneracy point, the superconducting gap-like structure is lifted and a significant increase in zero-bias conductance occurs. In order to compare these observations with those on bare junctions, the differential conductance was measured as a function of magnetic



field  $B_z$ , Figure 4.3(b), at  $V_{\text{gate}} = 1.95$  V, far into the off-resonant regime (dashed line in Figure 4.3(a)). A reduced gap  $2E_{\text{gap}} \approx 0.7$  meV appears. Gradual suppression of the superconducting features takes place from zero magnetic field to about 0.6 T, leaving a residual gap structure weakly evolving from 0.6 T to 1T. In the inset of Figure 4.3(b) the differential conductance map from which the spectra are extracted is shown. The magnetic field ranges from -1 T to +1 T. The smoothing of the superconducting features is symmetric for negative and positive field values.

In the present example, the charging energy  $U \geq 100$  meV and the tunneling rate  $\Gamma \approx 1$  meV<sup>1</sup>, characteristic energies of single-electron transport, are related to  $E_{\text{gap}}$  by  $U \gg \Gamma \gtrsim E_{\text{gap}}$ . The first condition,  $U \gg \Gamma$ , guarantees Coulomb blockade and single-electron-transistor behavior [28]. The second condition,  $\Gamma \gtrsim E_{\text{gap}}$ , allows for the off-resonant inelastic quasiparticle tunneling and would theoretically enable the on-resonant transport of both single electrons and Cooper pairs [29]. The off-resonant transport and the strong increase in zero-bias conductance observed in Figure 4.3(a) are consistent with this picture and will be the subject of further study.

### 4.3. CONCLUSION

In this chapter, we have presented a three-terminal hybrid electromigrated break-junction with high-critical field superconducting electrodes for single-molecule studies. In this SN-I-NS junction, superconductivity is induced in the gold by proximitizing it with MoRe. Gold as a normal metal allows for the creation of nanogaps by controlled electromigration and preserves the advantage of molecule-gold chemistry. The use of MoRe as a superconductor guarantees an induced gap larger than the previously reported Al-based designs. We characterize induced superconductivity as a function of temperature and magnetic field intensity and direction and demonstrate superconducting behavior up to 4.6 K and a critical magnetic field of 6 T. We finally show preliminary transport measurements through an individual Fe<sub>4</sub> single molecule magnet. Coexistence of Coulomb blockade and superconducting transport is observed. Low-bias on- and off-resonant conductance behavior suggests that, owing to the relatively high gap energy  $E_{\text{gap}}$ , the condition  $U \gg \Gamma \gtrsim E_{\text{gap}}$  for intermediate coupling transport is satisfied. This intermediate coupling transport regime appears to be promising for investigating the interaction between confined electrons and superconductivity. Moreover, it constitutes the prerequisite - with the additional condition  $k_B T_K \sim E_{\text{gap}}$  - for the investigation of the interplay between Kondo screening and superconducting pairing.

### 4.4. APPENDIX

#### 4.4.1. ELECTROMIGRATION CURRENT-VOLTAGE CHARACTERISTICS AND THREE TERMINAL MEASUREMENTS

Feedback controlled software is used to monitor and adjust the voltage across the gold wire to steadily create a constriction at room temperature. Figure 4.4 shows the typical current voltage characteristics recorded during the creation of a constriction. The volt-

<sup>1</sup>The value of  $\Gamma$  is extracted from the FWHM of the Lorentzian fit of the Coulomb peak at a magnetic field of 8T, in order to minimize the influence of superconductivity on transport. The lower bound value for  $U$  is estimated from the full  $V$  vs  $V_{\text{gate}}$  conductance map (See also section 4.4.3 of the Appendix).

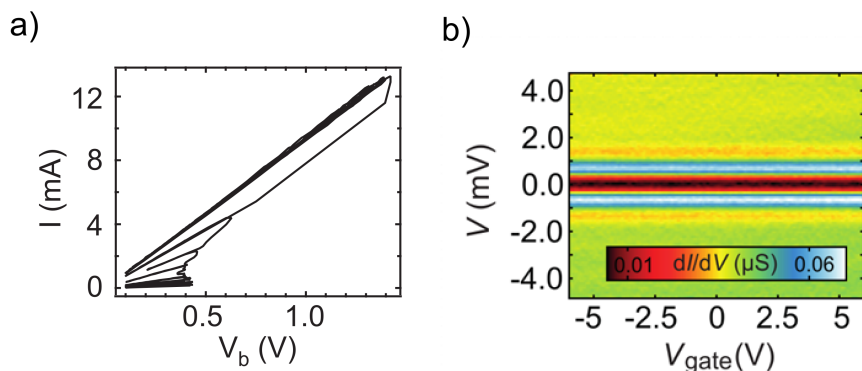


Figure 4.4: (a) Current-voltage characteristics for the electromigration of a typical device. (b) Three terminal measurement of an SN-I-NS junction at low temperature (100 mK). Current is measured as a function bias voltage and back-gate voltage. A numerical derivative is taken to plot  $dI/dV$ - $V_b$ - $V_g$ .

4

age is ramped up to  $> 1\text{V}$  at which point the resistance of the junction starts to change and the feedback software decreases the voltage to arrest an avalanche breaking of the wire. This continues to create a final constriction which is left to self-break at room temperature leaving a few-nanometer gap.

Figure 4.4 shows a three terminal measurement of an SN-I-NS junction taken at 100 mK after the electromigration and self-breaking process. A numerical derivative is taken to plot  $dI/dV$  versus bias and gate voltage. The conductance does not change over the accessible gate voltage range ( $\pm 7\text{V}$ ) indicating tunneling through a gate independent vacuum barrier.

#### 4.4.2. TEMPERATURE AND MAGNETIC FIELD DEPENDENCE FOR A SECOND CHARACTERISTIC DEVICE

Figure 4.5 shows the complete characteristics for a second device. This SN-I-NS junction shows the same characteristics as the main text device. The softening of the proximity induced gap with temperature is shown in Figure 4.5(a). Again, a residual gap is present at 4.5K. Figures 4.5(b) and 4.5(c) for the magnetic field dependence in the z and y-axis. Greater modulation of the gap is found for fields in the z-axis direction.

#### 4.4.3. ESTIMATION OF THE CHARGING ENERGY $U$ AND ELECTRODE COUPLING CONSTANT $\Gamma$

An estimation of the charging energy  $U$  can be obtained from the  $V$  vs.  $V_{\text{gate}}$  differential conductance map according to  $U = \beta \Delta V_{\text{gate}}$ , where  $\beta$  is the gate coupling, obtained from the slopes of the Coulomb edges of the same conductance maps, and  $\Delta V_{\text{gate}}$  is the distance in gate voltage between two charge degeneracy points. From figure 4.6,  $\beta = 13$  meV/V and  $\Delta V_{\text{gate}} \geq 7.5$  V, so that  $U \geq 100$  meV.

The molecule-electrode coupling constant  $\Gamma$  is obtained from fitting the charge de-

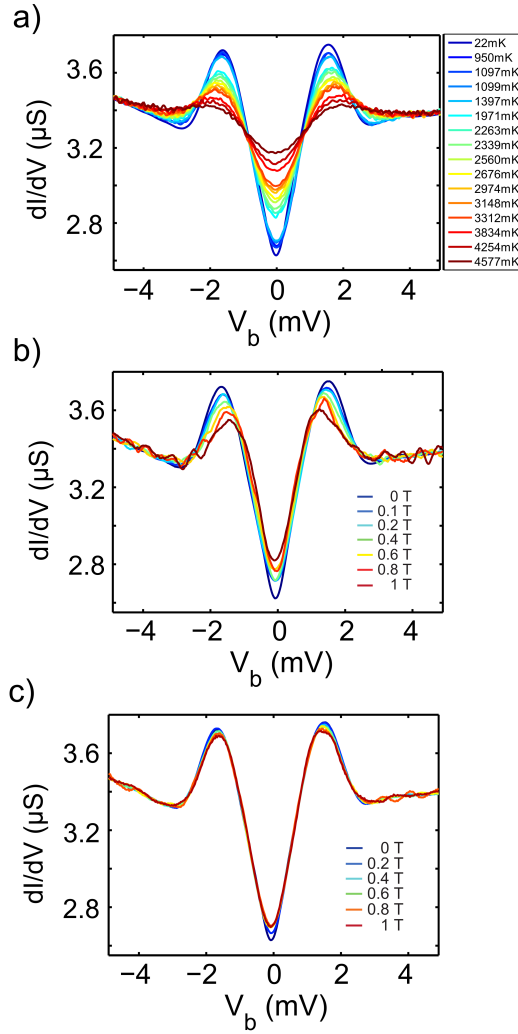


Figure 4.5: (a) Temperature dependence of the SN-I-NS junctions. A numerical derivative is plotted versus the applied bias voltage. (b) Magnetic field dependence of the junction with the external field in the z-axis direction. (c) Magnetic field dependence of the junctions with the external field in the y-axis direction.

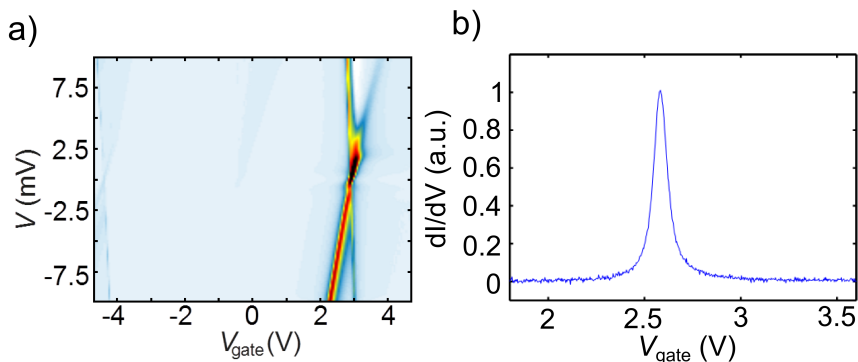


Figure 4.6: (a) Coarse differential conductance map of an individual Fe<sub>4</sub>-SMM as a function of gate and bias voltages. The selected voltage range is the maximum allowed by the gate oxide. (b) Normalized differential conductance zero-bias trace (charge degeneracy point) as a function of gate voltage obtained at a magnetic field of 8T. At this field superconductivity is completely lifted so that regular quasiparticle transport is restored. The molecule-electrode coupling constant is obtained by fitting the trace to a Lorentzian.

generacy peak ( $V = 0\text{V}$ ,  $B = 8\text{T}$ ) shown in figure S5 to a Lorentzian function. The FWHM of the Lorentzian extracted from the fit multiplied by the gate coupling yields  $\Gamma \approx 1$  meV. The high magnetic field ensures a negligible influence of superconductivity on transport.

## REFERENCES

- [1] R. Gaudenzi, J. O. Island, J. De Bruijckere, E. Burzurí, T. M. Klapwijk, and H. S. J. Van der Zant, *Superconducting molybdenum-rhenium electrodes for single-molecule transport studies*, Applied Physics Letters **106**, 222602 (2015).
- [2] G. E. Blonder, M. Tinkham, and T. M. Klapwijk, *Transition from metallic to tunneling regimes in superconducting micro-constrictions - excess current, charge imbalance, and super-current conversion*, Physical Review B **25**, 4515 (1982).
- [3] T. Soda, T. Matsuura, and Y. Nagaoka, *S-D exchange interaction in a superconductor*, Progress of Theoretical Physics **38**, 551 (1967).
- [4] H. Shiba and T. Soda, *Superconducting tunneling through barrier with paramagnetic impurities*, Progress of Theoretical Physics **41**, 25 (1969).
- [5] H. Shiba, *Classical spins in superconductors*, Progress of Theoretical Physics **40**, 435 (1968).
- [6] A. I. Rusinov, *Superconductivity near a paramagnetic impurity*, Soviet Journal of Experimental and Theoretical Physics Letters **9**, 85 (1969).
- [7] E. Scheer, P. Joyez, D. Esteve, C. Urbina, and M. H. Devoret, *Conduction channel transmissions of atomic-size aluminum contacts*, Physical Review Letters **78**, 3535 (1997).
- [8] V. Koerting, B. M. Andersen, K. Flensberg, and J. Paaske, *Nonequilibrium transport via spin-induced subgap states in superconductor/quantum dot/normal metal cotunnel junctions*, Physical Review B **82**, 245108 (2010).
- [9] B. M. Andersen, K. Flensberg, V. Koerting, and J. Paaske, *Nonequilibrium transport through a spinful quantum dot with superconducting leads*, Physical Review Letters **107**, 256802 (2011).
- [10] K. J. Franke, G. Schulze, and J. I. Pascual, *Competition of superconducting phenomena and kondo screening at the nanoscale*, Science **332**, 940 (2011).
- [11] I. A. Sadovskyy, D. Chevallier, T. Jonckheere, M. Lee, S. Kawabata, and T. Martin, *Josephson effect through an anisotropic magnetic molecule*, Physical Review B **84**, 184513 (2011).
- [12] M. Lee, T. Jonckheere, and T. Martin, *Josephson effect through an isotropic magnetic molecule*, Physical Review Letters **101**, 146804 (2008).
- [13] J. Bauer, J. I. Pascual, and K. J. Franke, *Microscopic resolution of the interplay of Kondo screening and superconducting pairing: Mn-phthalocyanine molecules adsorbed on superconducting Pb(111)*, Physical Review B **87**, 075125 (2013).
- [14] A. Y. Kasumov, K. Tsukagoshi, M. Kawamura, T. Kobayashi, Y. Aoyagi, K. Senba, T. Kodama, H. Nishikawa, I. Ikemoto, K. Kikuchi, V. T. Volkov, Y. A. Kasumov,

- R. Deblock, S. Gueron, and H. Bouchiat, *Proximity effect in a superconductor-metallofullerene-superconductor molecular junction*, Physical Review B **72**, 033414 (2005).
- [15] C. B. Winkelmann, N. Roch, W. Wernsdorfer, V. Bouchiat, and F. Balestro, *Superconductivity in a single-C<sub>60</sub> transistor*, Nature Physics **5**, 876 (2009).
- [16] E. Scheer, W. Belzig, Y. Naveh, M. H. Devoret, D. Esteve, and C. Urbina, *Proximity effect and multiple Andreev reflections in gold atomic contacts*, Physical Review Letters **86**, 284 (2001).
- [17] M. R. Buitelaar, T. Nussbaumer, and C. Schonenberger, *Quantum dot in the Kondo regime coupled to superconductors*, Physical Review Letters **89**, 256801 (2002).
- [18] S. De Franceschi, L. Kouwenhoven, C. Schonenberger, and W. Wernsdorfer, *Hybrid superconductor-quantum dot devices*, Nature Nanotechnology **5**, 703 (2010).
- [19] J. Talvacchio, M. A. Janocko, and J. Gregg, *Properties of evaporated Mo-Re thin-film superconductors*, Journal of Low Temperature Physics **64**, 395 (1986).
- [20] K. O'Neill, E. A. Osorio, and H. S. J. van der Zant, *Self-breaking in planar few-atom Au constrictions for nanometer-spaced electrodes*, Applied Physics Letters **90**, 133109 (2007).
- [21] H. Park, A. K. L. Lim, A. P. Alivisatos, J. Park, and P. L. McEuen, *Fabrication of metallic electrodes with nanometer separation by electromigration*, Applied Physics Letters **75**, 301 (1999).
- [22] T. M. Klapwijk, *Proximity effect from an Andreev perspective*, Journal of Superconductivity **17**, 593 (2004).
- [23] S. Gueron, H. Pothier, N. O. Birge, D. Esteve, and M. H. Devoret, *Superconducting proximity effect probed on a mesoscopic length scale*, Physical Review Letters **77**, 3025 (1996).
- [24] A. A. Golubov, E. P. Houwman, J. G. Gijsbertsen, V. M. Krasnov, J. Flokstra, H. Rogalla, and M. Y. Kupriyanov, *Proximity effect in superconductor-insulator-superconductor Josephson tunnel-junctions - theory and experiment*, Physical Review B **51**, 1073 (1995).
- [25] W. Belzig, C. Bruder, and G. Schon, *Local density of states in a dirty normal metal connected to a superconductor*, Physical Review B **54**, 9443 (1996).
- [26] K. D. Usadel, *Generalized diffusion equation for superconducting alloys*, Physical Review Letters **25**, 507 (1970).
- [27] S. Accorsi, A. L. Barra, A. Caneschi, G. Chastanet, A. Cornia, A. C. Fabretti, D. Gatteschi, C. Mortalo, E. Olivieri, F. Parenti, P. Rosa, R. Sessoli, L. Sorace, W. Wernsdorfer, and L. Zobbi, *Tuning anisotropy barriers in a family of tetrairon(III) single-molecule magnets with an S=5 ground state*, Journal of the American Chemical Society **128**, 4742 (2006).

- [28] J. M. Thijssen and H. S. J. Van der Zant, *Charge transport and single-electron effects in nanoscale systems*, Physica Status Solidi B **245**, 1455 (2008).
- [29] L. I. Glazman and K. A. Matveev, *Resonant Josephson current through Kondo impurities in a tunnel barrier*, JETP Letters **49**, 659 (1989).





# 5

## PROXIMITY-INDUCED SHIBA STATES IN A MOLECULAR JUNCTION

*Superconductors containing magnetic impurities exhibit intriguing phenomena derived from the competition between Cooper pairing and Kondo screening. At the heart of this competition are the Yu-Shiba-Rusinov (Shiba) states which arise from the pair breaking effects a magnetic impurity has on a superconducting host. Hybrid superconductor-molecular junctions offer unique access to these states but the added complexity in fabricating such devices has kept their exploration to a minimum. Here, we report on the successful integration of a model spin 1/2 impurity, in the form of a neutral and stable all organic radical molecule, in proximity-induced superconducting break-junctions. Our measurements reveal excitations which are characteristic of a spin-induced Shiba state due to the radical's unpaired spin strongly coupled to a superconductor. By virtue of a variable molecule-electrode coupling, we access both the singlet and doublet ground states of the hybrid system which give rise to the doublet and singlet Shiba excited states, respectively. Our results show that Shiba states are a robust feature of the interaction between a paramagnetic impurity and a proximity-induced superconductor where the excited state is mediated by correlated electron-hole (Andreev) pairs instead of Cooper pairs.*

---

Parts of this chapter have been submitted for publication.

## 5.1. INTRODUCTION

A quantum dot (QD) or impurity coupled to a superconductor constitutes a rich physical system in which many-body effects compete for the ground state[1–9]. The ground state can take the form of a BCS-like singlet, a spin degenerate doublet, or a Kondo-like singlet depending on the relative strengths of the characteristic energies of the competing phenomena (charging energy,  $U$ , superconducting gap,  $\Delta$ , Kondo energy,  $T_K$ ). For weak Coulomb interaction ( $U \ll \Delta$ ), the BCS singlet, composed of the superposition of unoccupied and doubly occupied states of the dot, prevails. Subgap excitations of this ground state are the well-known Andreev bound states. This regime has been explored in carbon nanotube[10, 11] and nanowire[12, 13] devices where  $\Delta$  can be large enough relative to  $U$  to allow the BCS superposition state. For larger charging energy however, the doublet becomes the energetically favored ground state (at temperatures above  $T_K$ ) and a competition between Kondo screening and Cooper pairing sets in at temperatures below  $T_K$ [8, 14]. For weak Kondo energy ( $T_K \ll \Delta$ ) the ground state is the degenerate doublet as screening is incomplete due to a lack of quasiparticles at the Fermi level. For strong Kondo energy ( $T_K \gg \Delta$ ), quasiparticles screen the spin and the Kondo singlet becomes the ground state. Excitations on top of these ground states are the Yu-Shiba-Rusinov (or simply Shiba) states[15–18]. First experimentally observed in tunneling spectra of magnetic adatoms adsorbed on Nb[19], these states were recently shown to lead to topological Shiba bands required for the observation of Majorana end modes in atomic chains adsorbed on a superconducting surface[20–22].

Besides early tunneling experiments on Kondo alloys producing conventional Shiba bands[23], the great majority of investigations of superconductor-QD systems are with magnetic impurities[2, 7, 19, 24], nanowires[3, 4] or nanotubes[25–27] coupled directly to a bulk superconductor. In these systems the singlet Shiba excited state is created by breaking a Cooper pair which allows a quasiparticle to pair with the localized spin in the quantized system. A similar interaction may occur through proximity induced superconductivity but has not been explored and requires attention as proposals and investigations of Majorana bound states engineered through proximity induced systems grow[12, 28–33].

The hybrid superconductor-molecule device grants a unique exploration of the superconductor-QD phase diagram as the energy spacing between molecular orbitals of a molecule is typically orders of magnitude larger than the other energy scales completely suppressing the formation of the BCS-like singlet ground state and offering investigation of the large- $U$  regime. The added difficulty in fabricating such devices has limited their investigation to only a few studies[34, 35]. Additionally, direct contact to a superconductor leads to only weak coupling (relatively small  $\Gamma$ ) leaving access to the Kondo regime (and competing phenomena) unattainable[34]. Instead, gold can be used as an intermediate material allowing stronger coupling through the sulfur-gold bond but is not superconducting itself and thus requires exploitation of the proximity effect.

Here we report on investigations of the large- $U$  regime of the superconductor-QD system and the observation of Shiba states in a completely proximitized superconducting junction hosting a model spin 1/2 impurity. As opposed to direct coupling to a bulk superconductor with a phase coherent condensate giving rise to spin induced Shiba states, Shiba states in our system are supported by correlated electron-hole (Andreev)

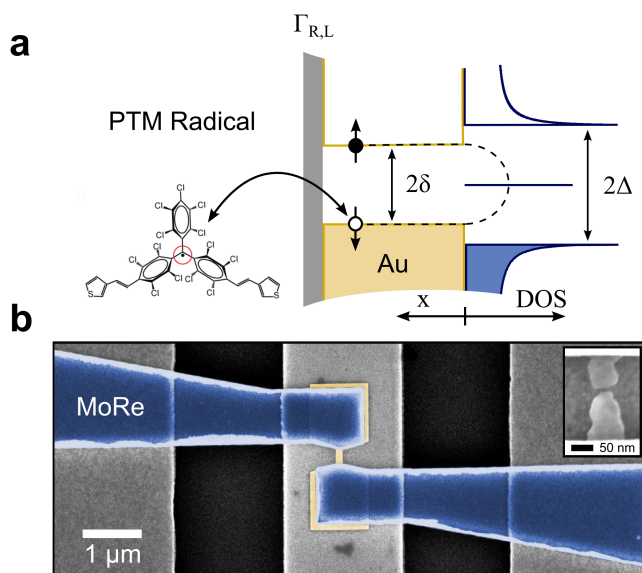


Figure 5.1: **Proximity induced interaction with an all organic radical molecule and device design.** (a) Schematic representation of a radical molecule coupled to a proximity induced superconducting gold electrode. The red circle represents the unpaired spin at the center of the molecule. (b) False-colored scanning electron microscopy (SEM) image of a lithographically identical junction with superconducting electrodes colored blue and gold nanowire colored gold. The inset shows a SEM image of an electromigrated junction after measurement, scale bar 50 nm.

pairs. Figure 5.1(a) depicts this situation in which a magnetic impurity (in our case a molecule with an unpaired spin at its center signified by a red circle) on the left side is tunnel coupled to a proximity-induced superconductor on the right side. The proximity effect in the gold is mediated by the well-known Andreev reflection process that occurs at the interface between the normal metal (gold region) and the superconductor (blue region) giving rise to Andreev pairs in the gold leads[36] which can interact with the molecule through an exchange coupling. As a result of a variable molecule-electrode coupling for different devices, we access both the singlet and doublet ground states (and their corresponding Shiba excited states) of the large- $U$  superconductor-QD phase diagram. We further corroborate these results through calculations based on the Anderson impurity model while taking into account the proximity induced nature of the gold electrodes.

As a prototypical spin 1/2 impurity for this study, we have judiciously selected a neutral and stable all organic radical (polychlorotriphenylmethyl, PTM) which we have shown produces a robust Kondo effect in gold break-junctions[37]. The chemical structure of the molecule is shown on the left side of fig. 5.1(a). Three chlorinated phenyl rings are connected to the central carbon atom through  $sp^2$  hybridization[38]. A single unpaired electron, giving the molecule an intrinsic paramagnetic ground state, is mainly localized at the central carbon atom and protected from the environment by the more

bulky chlorine atoms. This protection gives the radical its high chemical and thermal stability. Additionally, this stability has been shown to result in Kondo correlations at low temperatures in gold break junctions which are stable against mechanical and electrostatic variations[37]. Density functional theory (DFT) calculations show that the Fermi energy (with gold electrodes) of the molecule sits within a sizable energy gap (2 eV) between the singly occupied molecular orbital (SOMO) and the lowest unoccupied molecular orbital (LUMO) creating a stable electronic configuration with a large "charging energy" in the ground state. This is further verified by the absence of resonant transport at low bias in the whole range of gate voltages that can be applied in our electromigrated break junctions[37]. This makes the PTM radical an ideal molecule to explore the large  $U$  limit of the superconductor-QD phase diagram which favors Shiba excited states for both the singlet and doublet ground states.

## 5.2. DEVICE DESIGN

The junction fabrication and characterization has been detailed in Refs. [39, 40] which we briefly summarize here. Fig. 5.1(b) shows a false colored scanning electron microscopy (SEM) image of a representative junction. The blue colored electrodes are the bulk superconducting banks created by sputtering molybdenum-rhenium (60/40,  $T_c \approx 8.5K$ ). The gold colored nanowire and contact pads are created by electron-beam evaporation of gold (thickness, 12 nm). The gray vertical strip under the junction is a  $AlO_x/AuPd$  back gate which can be used to electrostatically gate the junction. A combination of electromigration and a self-breaking technique is used to open a nanogap in the gold nanowire. The inset shows an SEM image of a typical nanogap.

Several empty nanogaps are measured at low temperatures in order to characterize the superconducting proximity effect in the gold electrodes without molecules. In fig. 5.2(a) we show the low temperature (100 mK) differential conductance ( $dI/dV_b$ ) as a function of voltage bias ( $V_b$ ) for an empty junction (no molecule). The two conductance peaks at voltages of  $\approx \pm 1.6$  mV signal the overlap of the induced quasiparticle peaks in the two gold leads (see schematic in fig. 5.2(b)) and gives us a rough estimate of the induced mini-gap. A mini-gap ( $\delta$ , see fig. 5.1(a)) exists in the proximity-induced superconductor with a magnitude related to the Thouless energy,  $E_{th} = \hbar D/L^2$ , where  $D = 0.026 \text{ m}^2/\text{s}$  is the diffusion constant for gold[41] and  $L$  is the electrode length[42]. If we assume a symmetric left and right gold electrode with a tunnel barrier in between, the length of each electrode is  $L \approx 140$  nm. This gives an estimate of  $\delta = 0.87$  meV which agrees roughly with the value obtained from fig. 5.2(a),  $\delta \approx 0.8$  meV. The position of the nanogap depends on the electromigration process and is not always symmetrically created at the center of the nanoribbon which leads to asymmetric proximity induced density of states (DOS) (see section 5.7.1 for details). As opposed to coupling directly to the bulk and having a BCS like DOS, our gold leads offer external tuning of the induced gap through application of a magnetic field. This allows *in-situ* tuning of  $\delta$  relative to the Kondo energy,  $T_K$ , and exploration of the phase transition between the singlet and doublet ground states.

In order to carry out measurements on the PTM molecule, a solution of molecules (concentration 1 mM) is drop-cast onto an array of 24 junctions before electromigration. After the electromigration and self-breaking of all junctions, the solution is evapo-

rated leaving behind roughly a monolayer of molecules and the sample is cooled down in a dilution refrigerator (base temperature 100 mK). All low temperature measurements are performed using a two-terminal voltage bias and numerical differentiation of the measured current/applied voltage to obtain the differential conductance. Detailed measurements were performed on 7 junctions (labeled A through G, see section 5.7.2 for an overview).

### 5.3. THE NORMAL STATE

We now turn to the low temperature characteristics of our radical molecular junctions where we first show the results for the normal-state measurements. By applying a small finite perpendicular magnetic field (200 mT, directed out of the page in fig. 5.1(b)) to the junctions, the proximity effect in the normal leads can be completely suppressed. The curve in the inset of fig. 5.2(c) shows the differential conductance ( $dI/dV_b$ ) as a function of bias voltage in the normal state for device C. A zero-bias Kondo peak is observed which closely resembles measurements of the same molecule in all-gold junctions[37]. This peak is characterized as a function of temperatures up to 4 K (fig. 5.2(c)) and magnetic fields up to 8 T (fig. 5.2(d)). We observe the typical exponential decrease of the Kondo peak height with increasing temperature and its splitting in high magnetic fields. From the temperature dependence of the peak height we estimate a Kondo temperature of 4.4 K and from the splitting we estimate a  $g$ -factor of 2.4, all consistent with Kondo correlations observed in all-gold junctions. As reported previously[37], we also observe little modulation of the peak in the normal state with electrostatic gating due to the sizable SOMO-LUMO gap (see section 5.7.3).

### 5.4. THE SUPERCONDUCTING STATE

Moving now to the characteristics in the superconducting state, the black curve in fig. 5.3(a) shows the differential conductance as a function of voltage bias in the superconducting state ( $B = 0$  T) for device D. The red curve in the same panel is the measurement in the normal state ( $B = 200$  mT) showing the zero bias peak arising from the Kondo effect discussed previously. In the superconducting state two peaks are discernible, symmetric in bias, accompanied by side dips at higher bias which are qualitatively distinctive from the empty junction curves in fig. 5.2(a) and in section 5.7.1. These peaks signal excitations of the coupled superconductor-QD system and have been shown to be associated with (multiple) Andreev reflections (MAR) and spin induced Yu-Shiba-Rusniov states. Conductance peaks due to MAR however are not accompanied by side dips and become less probable as the asymmetry between the left and right leads is increased[3, 25]. Asymmetries of  $\Gamma_L/\Gamma_R \approx 10^{-2} - 10^{-3}$  in nanowire experiments are enough to completely suppress MAR contributions[3]. With the built in high asymmetry of the couplings and given the spin 1/2 Kondo effect in the normal state, a natural explanation for the excitation peaks in our hybrid molecular devices is that they originate from spin induced Shiba states.

Figure 5.3(c) shows a schematic of the coupling situation and density of states. The blue colored electrode and corresponding DOS represent the hybridization of the radical with the more strongly coupled electrode resulting in Shiba excited states. Micro-

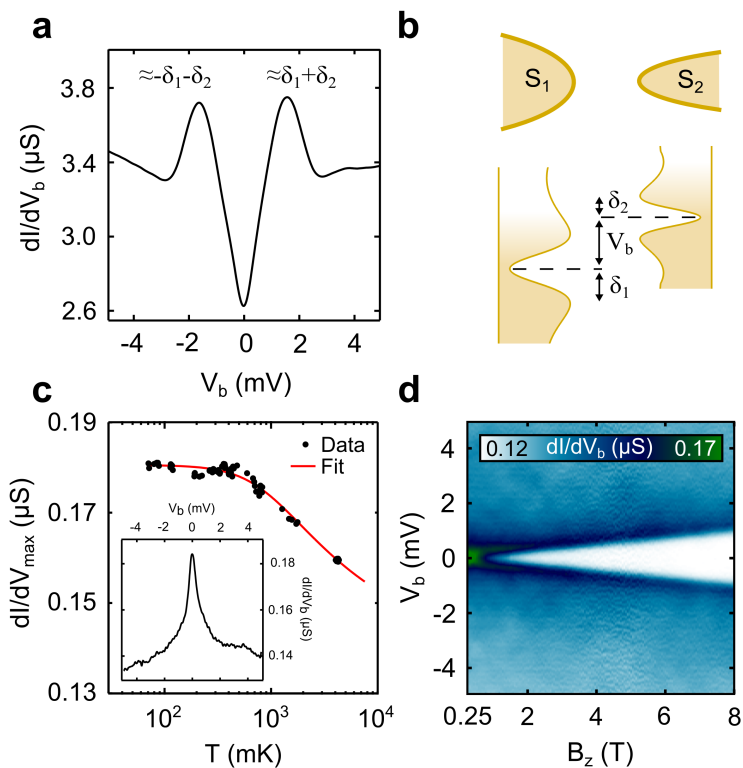


Figure 5.2: **Low temperature characterizations of an empty junction and a molecular junction in the normal state.** (a) Low temperature (100 mK) measurement of the differential conductance ( $dI/dV$ ) as a function of voltage bias ( $V_b$ ) of an empty gap. (b) Schematic representation of the asymmetry in the proximity induced gaps of the left and right leads. (c)  $dI/dV$  vs.  $V_b$  showing the Kondo peak in the normal state (200 mT). The inset shows the temperature dependence which corresponds to a Kondo temperature of 4.4 K. (d)  $dI/dV$  as a function of  $V_b$  and magnetic field showing the splitting of the Kondo peak.

scopically, these states arise from the interaction of Andreev pairs at finite energy in the proximity-induced lead and the unpaired spin of the radical molecule. The weakly coupled gold lead on the right side essentially probes the hybridization of the molecule with the left electrode. This results in conductance peaks in fig. 5.3(a) at energies of  $\pm(E_b + \delta_2)$  where  $E_b$  is the excited state energy and  $\delta_2$  is the proximity-induced gap of the probe electrode. In addition to these peaks, side shoulders are visible at lower bias voltage which we interpret as Shiba replicas. Shiba replicas are visible for a sufficient density of quasiparticles in the mini-gap of the probe electrode which is reasonable considering the soft proximity-induced gap of our empty junctions (see fig. 5.2(a)). With an increase in temperature we furthermore observe the emergence of an anomalous zero-bias peak (dashed curve in Fig. 5.2(a)) which we interpret as a mini-Kondo due to increased quasiparticle filling (see section 5.7.4 for a discussion).

A comparison of the characteristic energies ( $\delta_{avg}$  vs.  $k_B T_K$ ) for device D allows us to determine the ground state of the coupled system. The edge of the dips in fig. 5.3(a) roughly correspond to  $\delta_1 + \delta_2$  from which we calculate an average induced gap of  $\delta_{avg} = (\delta_1 + \delta_2)/2 = 0.8$  meV. Compared with the Kondo energy extracted from the normal state temperature dependence of the Kondo peak ( $k_B T_K = 0.2$  meV), we find that the average induced gap is 4 times larger. In this device, the larger finite Andreev pair energy results in a doublet ground state where the radical's spin is not sufficiently screened by quasiparticle states near the Fermi energy in the superconducting state to allow the Kondo singlet.

By applying a perpendicular magnetic field (see inset of fig. 5.3(a)), the ground state of the system can be tuned from the doublet ground state to the Kondo singlet. As the field is increased the Shiba peaks move to lower bias voltages, following the closure of the proximity-induced gaps. At a field of  $\approx 130$  mT the gap completely closes leaving a zero bias peak due to Kondo screening of the radical's spin and a phase transition to the Kondo-like singlet ground state.

Our low temperature measurements are further supported by calculations. Starting with a modified Anderson impurity model (Anderson Hamiltonian coupled to leads modeled by BCS Hamiltonians) we calculate the differential conductance as a function of bias voltage using the non-crossing approximation[3, 43, 44]. The broadening of the DOS due to the proximity effect is handled by introducing the Dynes function which is taken as a phenomenological broadening term that softens the BCS DOS of the bulk reservoirs[3, 45]. Fig. 5.3(b) shows a conductance curve from this calculation where the main features of the experimental curve can be reproduced. A zero-bias peak is present when the order parameter in the leads is set to zero (red curve). In the superconducting state with  $\delta = 4T_K$  and broadening ( $0.15\delta$ ), two peaks can be seen with accompanying side dips and shoulders at higher and lower bias, respectively (black curve). Quantitative differences are primarily due to an asymmetry in the couplings ( $\Gamma_L/\Gamma_R$ ) discussed previously which reduces the Kondo peak from  $2e^2/h$  and the exact shape of the DOS for each gold lead. Differences in the lengths of the two gold leads (see section 5.7.1 for details) means the broadening for the two leads would be different.

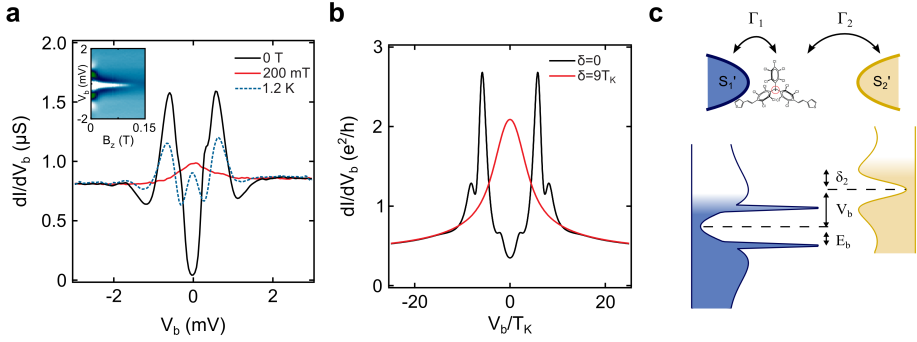


Figure 5.3: **Characterization and calculations of a molecular junction in the superconducting state.** (a) Low temperature (100 mK) measurement of the differential conductance ( $dI/dV_b$ ) as a function of voltage bias ( $V_b$ ) of a radical molecular junction at zero magnetic field (superconducting state) and 200 mT (normal state). The blue dashed curve shows the same measurement at 1.2 K ( $B = 0$  T). The inset shows the magnetic field dependence of the Shiba peaks. (b) Theoretical calculations of the modeled system taking into account the proximity-induced DOS of the leads. (c) Schematic representation of the probing of the Shiba excited state as a result of the coupling of the radical molecule with the proximity-induced superconducting Au electrode.

5

## 5.5. GROUND STATE SPECTROSCOPY IN THE SUPERCONDUCTING STATE

Depending on the relative energies of the proximity-induced gap and the Kondo energy, the ground state of the system, even in the superconducting state, can take the form of a doublet for weak coupling ( $k_b T_K < \delta$ ) or a Kondo-like singlet for strong coupling ( $k_b T_K > \delta$ ). By virtue of a variable molecule-electrode coupling, we probe a large range of Kondo energies relative to the average induced gap energy. In section 5.7.2 we show an overview of the 7 devices (A-G) having similar characteristics ordered by increasing Kondo energy. The Kondo temperature ranges from ( $\approx 1$  K to 18 K) for the seven devices.

In fig. 5.4 we show the weakest and strongest Kondo energy devices (junctions A and G). For junction A a Kondo peak cannot be discerned in the normal state (red curve fig. 5.4(a)) but a splitting ( $g = 2.1$ ) of the background is observed at higher magnetic fields fig. 5.4(b)). We estimate a Kondo temperature of  $\approx 1$  K from the critical field ( $B_c \approx 0.5 k_b T_K / (g \mu_B)$ ) at which the background begins to split in fig. 4(b) ( $B_c \approx 0.36$  T). Following the analysis for device D above we estimate an average induced gap of 0.8 meV. Comparing the two energy scales (0.8 meV vs. 0.09 meV), this device is similar to device D in which the doublet ground state wins over the Kondo singlet. The inset of fig. 5.4(a) shows the calculations for this regime where we have taken  $\delta = 9T_K$  and built in an asymmetry of  $\Gamma_L/\Gamma_R = 20$  to better simulate the results. Shiba peaks in this regime correspond to singlet excitations of the doublet ground state. This situation is depicted in fig. 5.4(c) in the excitation picture where a thick barrier and reduced quasiparticle states near the Fermi energy prevent the Kondo singlet from claiming the ground state of the coupled system. Here we signify the ground state and the excited state by occupancies of the molecule and the leads,  $|n_{mole}, n_{lead}\rangle$ . The Shiba excited state for this ground state,  $|\downarrow, \uparrow\rangle$ , is a singlet composed of the molecule's unpaired spin and an electron from a



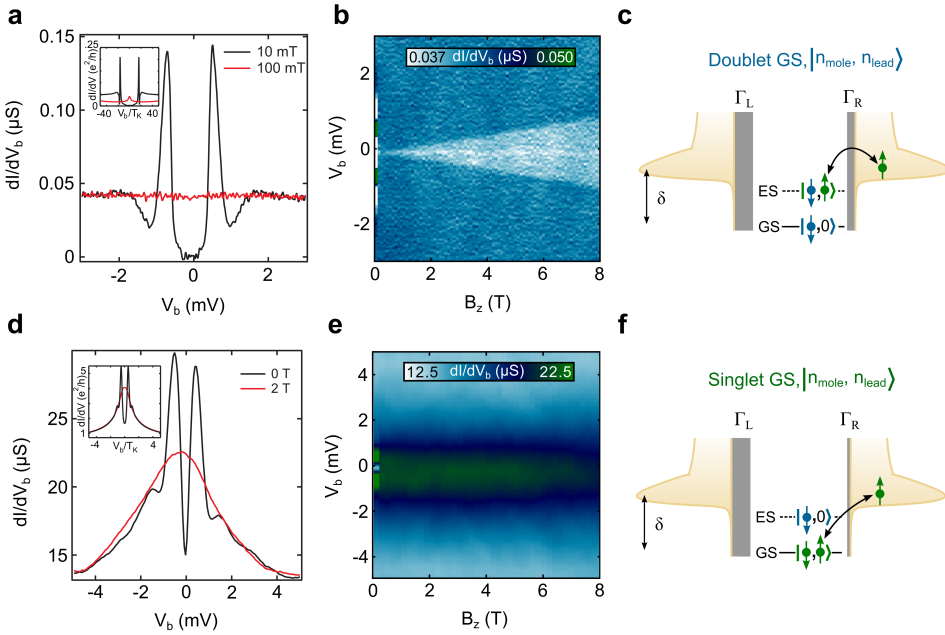


**Figure 5.4: Ground state spectroscopy of the hybrid radical system.** (a) The differential conductance ( $dI/dV_b$ ) as a function of voltage bias ( $V_b$ ) of a radical molecular junction at zero magnetic field (superconducting state) and 200 mT (normal state) in the doublet ground state regime ( $T_K < \delta$ ). Inset shows calculations for this regime ( $\delta = 9T_K$ ). (b) Color plot of the differential conductance ( $dI/dV_b$ ) as a function of voltage bias and magnetic field for the junction in panel (a). (c) Excitation picture of the ground and excited states in the doublet ground state regime. (d) The differential conductance ( $dI/dV_b$ ) as a function of voltage bias ( $V_b$ ) of a radical molecular junction at zero magnetic field (superconducting state) and 2 T (normal state) in the singlet ground state regime ( $T_K > \delta$ ). Inset shows calculations for this regime ( $\delta = 0.5T_K$ ). (e) Color plot of the differential conductance ( $dI/dV_b$ ) as a function of voltage bias and magnetic field for the junction in panel (d). (f) Excitation picture of the ground and excited states in the singlet ground state regime.

correlated Andreev pair in the leads (signified by the black arrow).

In fig. 5.4(d) we present the device with the largest Kondo temperature observed (18 K, estimated from the peak width). Comparing the characteristic energies for this device ( $\delta_{avg} = 0.7$  meV,  $k_b T_K = 1.6$  meV) we find that the large Kondo energy allows for screening of the radical's spin even in the superconducting state. This results in a singlet ground state at  $B = 0$  T. Calculations for this regime are shown in the inset of fig. 5.4(d) where we have taken  $\delta = 0.5 T_K$  and a broadening of  $0.25\delta$ . Excitations of this ground state are the magnetic doublet. This is depicted in fig. 5.4(f) in the excitation picture. A weak barrier allows for screening from electrons in the proximity-induced leads and a singlet state is formed by the combination of the radical's spin and an electron in the leads.

## 5.6. CONCLUSION

In conclusion, we have presented an investigation of the large- $U$  superconductor-QD phase diagram in the form of a radical molecule coupled to a proximity induced superconductor. In the superconducting state, we observe excitations which are characteristic of Shiba states as a result of the coupling between the radical and a proximity-induced superconductor. By applying a finite magnetic field, the proximity effect can be suppressed which allows a spin 1/2 Kondo effect. For the devices with the weakest and strongest Kondo energies we are able to probe both the doublet and singlet ground states which give rise to the singlet and doublet Shiba excited states, respectively. Our measurements are supported by calculations of the Anderson impurity model modified to account for the proximity-induced superconducting electrodes. Hybrid molecular junctions offer a unique investigation of the superconductor-QD system. In particular, with a suitable choice of molecule, an *in-situ* tunable Kondo effect would allow direct driving of the singlet to doublet quantum phase transition for a spin 1/2 impurity and the exact energies at which it occurs which is still an open question[2, 46, 47].

## 5.7. APPENDIX

### 5.7.1. LOW TEMPERATURE CHARACTERISTICS OF EMPTY GAPS

Figure 5.5 shows low-temperature characteristics for another empty gap in addition to the one presented in the main text in fig. 5.2(a). Fig. 5.5(a) shows the differential conductance ( $dI/dV$ ) as a function of the voltage bias ( $V_b$ ) in the superconducting state ( $B = 0$  T) and the normal state ( $B = 200$  mT). Fig. 5.5(b) shows  $dI/dV$  as a function of  $V_b$  and magnetic field. The critical field of the proximity induced superconductivity is roughly around 200 mT. Fig. 5.5(c) shows a scanning electron microscopy image of the junction after measurement. The difference in the length of the left and right electrode results in stronger and weaker proximity effects, respectively. Additionally, the shape of the electrode will play a role in the overall density of states of the proximity induced leads. In the normal state however, none of the empty gaps show the presence of a zero-bias peak in the low temperature characteristics that would signify Kondo screening of an impurity.

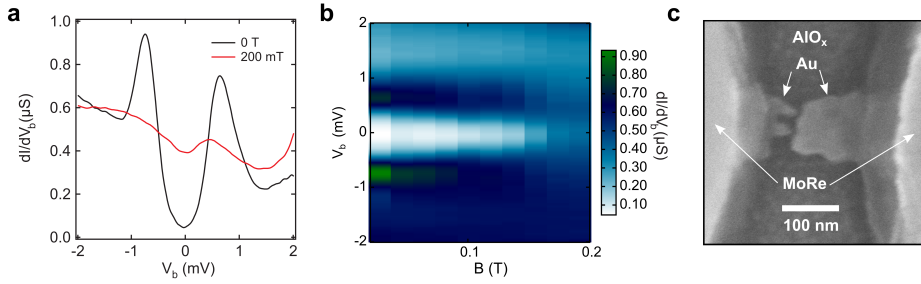


Figure 5.5: **Characteristics of another empty gap measured at low-temperature.** (a) Numerical differential conductance ( $dI/dV_b$ ) as a function of voltage bias ( $V_b$ ). The black curve shows the measurement at zero field and the red curve shows the measurement near the critical field of the proximity induced superconductivity. (b) Color plot of  $dI/dV_b$  as a function of  $V_b$  and perpendicular magnetic field. (c) Scanning electron microscopy image of the junction after measurement.

### 5.7.2. DEVICE OVERVIEW

Figure 5.6 shows an overview of all 7 junctions measured showing symmetric conductance peaks in the superconducting state and a zero-bias peak in the normal state. From the top to the bottom, the devices are arranged according to their critical field  $B_c$  of the Kondo peak except for device G which does not show a splitting because the critical field is larger than our experimental range. All devices were measured at  $\approx 100$  mK except for devices E and F which were measured at 1.8 K. The left side panels in fig. 5.6 shows the differential conductance  $dI/dV_b$  as a function of voltage bias  $V_b$  for each device in the superconducting state (0 T, black curve) and the normal state (200 mT, red curve). The right side panels show  $dI/dV_b$  as a function of  $V_b$  and magnetic field.

### 5.7.3. GATE DEPENDENCE

We observe little modulation of the conductance with back gate voltage due to the sizable (2 eV) SOMO-LUMO gap of the radical molecule. Fig. 5.7(a) shows  $dI/dV$  as a function of  $V_b$  and  $V_g$  for device E. With our accessible gate range, no degeneracy point is reached that would signal a shift to another charge state. The same is true in the normal state (see Fig. 5.7(b)). In fact, very little modulation of the conductance is observed (see Fig. 5.7(c)) overall which supports the robust Kondo effect and stable spin 1/2 nature of the molecule.

### 5.7.4. TEMPERATURE DEPENDENCE OF THE ANOMALOUS ZERO-BIAS PEAKS

At finite temperatures (1 K) a zero-bias peak emerges in the conductance curves which grows with temperature. Devices E and F show the presence of a zero-bias peak (see Device overview section). Zero bias peaks also emerge for devices A and D at higher temperatures (see Fig. 5.8). A plausible explanation for this peak is that a mini Kondo peak emerges in the gap at higher quasiparticle filling. Further supporting this claim is Fig. 5.8(c) which shows calculated curves of the modified Anderson impurity model (see main text for details) as a function of increased quasiparticle broadening in the leads. Similar to an increase of quasiparticles at higher temperatures, increased broadening

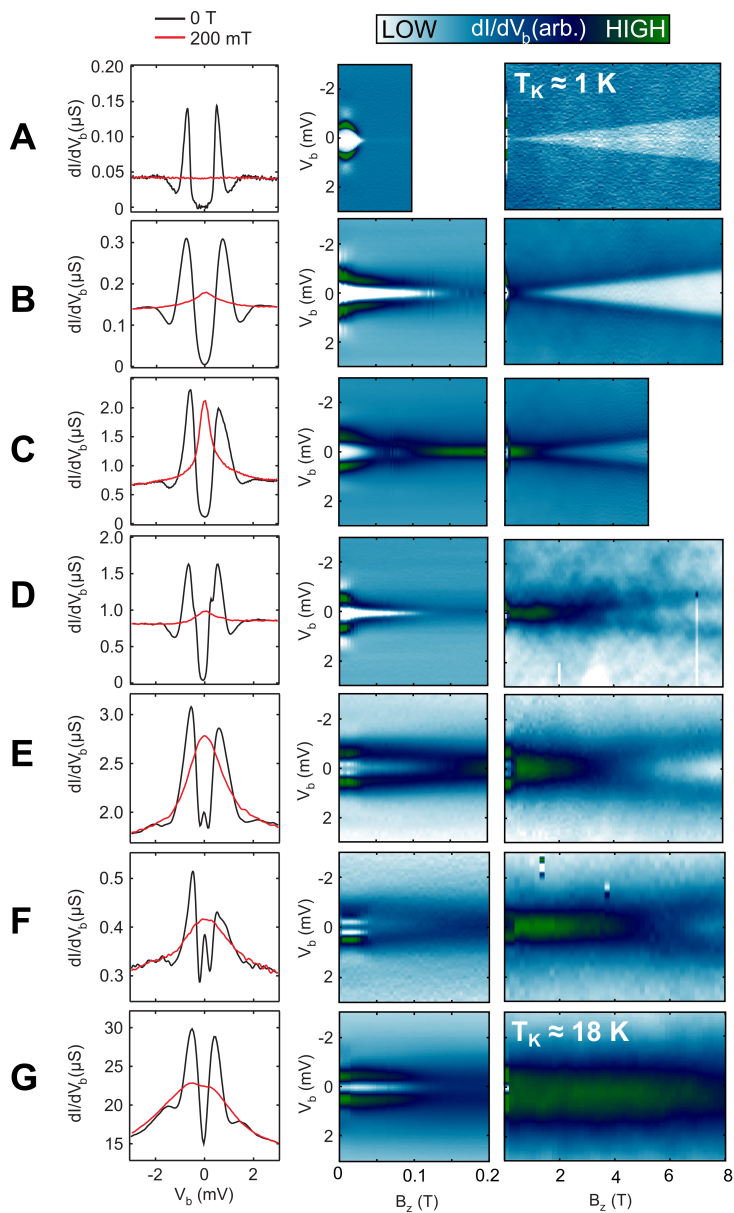


Figure 5.6: **Overview of all 7 devices measured.** The left-side panels show  $dI/dV_b$  as a function of  $V_b$  and the right-side panels show color plots of  $dI/dV_b$  as a function of  $V_b$  and magnetic field applied perpendicular to the junction.

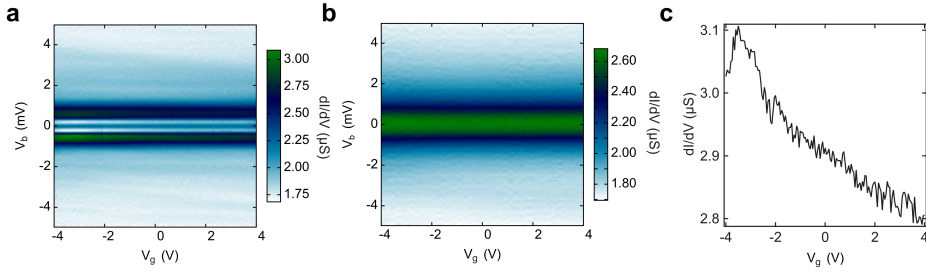


Figure 5.7: **Gate dependence** (a) A color plot of the  $dI/dV$  as a function of  $V_b$  and  $V_g$  in the superconducting state ( $B = 0$  T). (b) A color plot of the  $dI/dV$  as a function of  $V_b$  and  $V_g$  in the normal state ( $B = 300$  mT). (c) Line cut from panel (a) at a voltage of  $V_b = -0.5$  mV showing a small modulation with gate voltage.

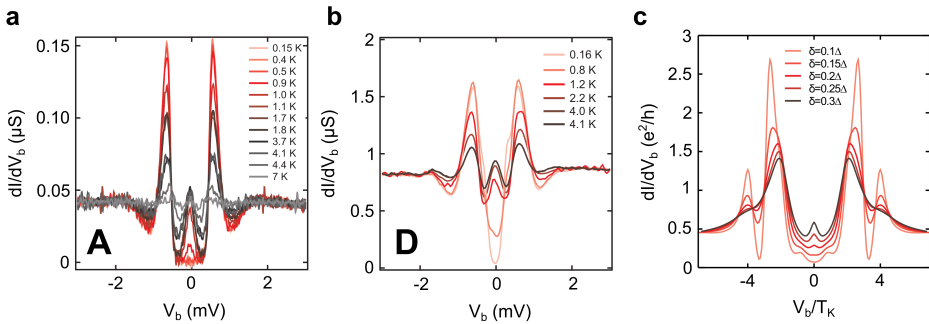


Figure 5.8: **Temperature dependence of the anomalous zero-bias peak** (a)  $dI/dV$  as a function of  $V_b$  for sample A as a function of temperature. (b)  $dI/dV$  as a function of  $V_b$  for sample D as a function of temperature. (c) Calculations of conductance as a function of  $V_b$  for increasing phenomenological broadening ( $\delta$ ) of the BCS gap.

leads to a zero-bias peak.

## REFERENCES

- [1] S. De Franceschi, L. Kouwenhoven, C. Schönenberger, and W. Wernsdorfer, *Hybrid superconductor-quantum dot devices*, *Nature Nanotechnology* **5**, 703 (2010).
- [2] K. J. Franke, G. Schulze, and J. I. Pascual, *Competition of superconducting phenomena and Kondo screening at the nanoscale*, *Science* **332**, 940 (2011).
- [3] E. J. H. Lee, X. Jiang, R. Aguado, G. Katsaros, C. M. Lieber, and S. De Franceschi, *Zero-bias anomaly in a nanowire quantum dot coupled to superconductors*, *Physical Review Letters* **109**, 186802 (2012).
- [4] W. Chang, V. E. Manucharyan, T. S. Jespersen, J. Nygård, and C. M. Marcus, *Tunneling spectroscopy of quasiparticle bound states in a spinful Josephson junction*, *Physical Review Letters* **110**, 217005 (2013).
- [5] E. J. H. Lee, X. Jiang, M. Houzet, R. Aguado, C. M. Lieber, and S. De Franceschi, *Spin-resolved Andreev levels and parity crossings in hybrid superconductor-semiconductor nanostructures*, *Nature Nanotechnology* **9**, 79 (2014).
- [6] J. S. Lim, R. López, R. Aguado, *et al.*, *Shiba states and zero-bias anomalies in the hybrid normal-superconductor Anderson model*, *Physical Review B* **91**, 045441 (2015).
- [7] N. Hatter, B. W. Heinrich, M. Ruby, J. I. Pascual, and K. J. Franke, *Magnetic anisotropy in Shiba bound states across a quantum phase transition*, *Nature Communications* **6**, 8988 (2015).
- [8] M. Žonda, V. Pokorný, V. Janiš, and T. Novotný, *Perturbation theory for an Anderson quantum dot asymmetrically attached to two superconducting leads*, *Physical Review B* **93**, 024523 (2016).
- [9] M. Ruby, F. Pientka, Y. Peng, F. von Oppen, B. W. Heinrich, and K. J. Franke, *Tunneling processes into localized subgap states in superconductors*, *Physical Review Letters* **115**, 087001 (2015).
- [10] J. D. Pillet, C. H. L. Quay, P. Morfin, C. Bena, A. L. Yeyati, and P. Joyez, *Andreev bound states in supercurrent-carrying carbon nanotubes revealed*, *Nature Physics* **6**, 965 (2010).
- [11] J.-D. Pillet, P. Joyez, M. F. Goffman, *et al.*, *Tunneling spectroscopy of a single quantum dot coupled to a superconductor: From Kondo ridge to Andreev bound states*, *Physical Review B* **88**, 045101 (2013).
- [12] V. Mourik, K. Zuo, S. M. Frolov, S. R. Plissard, E. P. A. M. Bakkers, and L. P. Kouwenhoven, *Signatures of Majorana fermions in hybrid superconductor-semiconductor nanowire devices*, *Science* **336**, 1003 (2012).
- [13] W. Chang, S. M. Albrecht, T. S. Jespersen, F. Kuemmeth, P. Krogstrup, J. Nygård, and C. M. Marcus, *Hard gap in epitaxial semiconductor-superconductor nanowires*, *Nature Nanotechnology* **10**, 232 (2015).

- [14] T. Meng, S. Florens, and P. Simon, *Self-consistent description of Andreev bound states in Josephson quantum dot devices*, Physical Review B **79**, 224521 (2009).
- [15] L. Yu, *Bound state in superconductors with paramagnetic impurities*, Acta Physica Sinica **21**, 75 (1965).
- [16] H. Shiba, *Classical spins in superconductors*, Progress of theoretical Physics **40**, 435 (1968).
- [17] A. I. Rusinov, *Superconductivity near a paramagnetic impurity*, Soviet Journal of Experimental and Theoretical Physics Letters **9**, 85 (1969).
- [18] A. V. Balatsky, I. Vekhter, and J.-X. Zhu, *Impurity-induced states in conventional and unconventional superconductors*, Reviews of Modern Physics **78**, 373 (2006).
- [19] A. Yazdani, B. A. Jones, C. P. Lutz, M. F. Crommie, and D. M. Eigler, *Probing the local effects of magnetic impurities on superconductivity*, Science **275**, 1767 (1997).
- [20] S. Nadj-Perge, I. K. Drozdov, B. A. Bernevig, and A. Yazdani, *Proposal for realizing Majorana fermions in chains of magnetic atoms on a superconductor*, Physical Review B **88**, 020407 (2013).
- [21] F. Pientka, L. I. Glazman, and F. von Oppen, *Topological superconducting phase in helical Shiba chains*, Physical Review B **88**, 15420 (2013).
- [22] S. Nadj-Perge, I. K. Drozdov, J. Li, H. Chen, S. Jeon, J. Seo, A. H. MacDonald, B. A. Bernevig, and A. Yazdani, *Observation of Majorana fermions in ferromagnetic atomic chains on a superconductor*, Science **346**, 602 (2014).
- [23] L. Dumoulin, E. Guyon, and P. Nedellec, *Tunneling study of localized bands in superconductors with magnetic impurities (normal Kondo alloys in the superconducting proximity)*, Physical Review B **16**, 1086 (1977).
- [24] G. C. Ménard, S. Guissart, C. Brun, S. Pons, V. S. Stolyarov, F. Debontridder, M. V. Leclerc, E. Janod, L. Cario, D. Roditchev, *et al.*, *Coherent long-range magnetic bound states in a superconductor*, Nature Physics **11**, 1013 (2015).
- [25] B. M. Andersen, K. Flensberg, V. Koerting, and J. Paaske, *Nonequilibrium transport through a spinful quantum dot with superconducting leads*, Physical Review Letters **107**, 256802 (2011).
- [26] B.-K. Kim, Y.-H. Ahn, J.-J. Kim, M.-S. Choi, M.-H. Bae, K. Kang, J. S. Lim, R. López, and N. Kim, *Transport measurement of Andreev bound states in a Kondo-correlated quantum dot*, Physical Review Letters **110**, 076803 (2013).
- [27] A. Kumar, M. Gaim, D. Steininger, A. L. Yeyati, A. Martín-Rodero, A. K. Hüttel, and C. Strunk, *Temperature dependence of Andreev spectra in a superconducting carbon nanotube quantum dot*, Physical Review B **89**, 075428 (2014).
- [28] A. Y. Kitaev, *Unpaired Majorana fermions in quantum wires*, Physics-Uspekhi **44**, 131 (2001).

- [29] J. Alicea, *Majorana fermions in a tunable semiconductor device*, Physical Review B **81**, 125318 (2010).
- [30] J. D. Sau, R. M. Lutchyn, S. Tewari, and S. D. Sarma, *Generic new platform for topological quantum computation using semiconductor heterostructures*, Physical Review Letters **104**, 040502 (2010).
- [31] Y. Oreg, G. Refael, and F. von Oppen, *Helical liquids and Majorana bound states in quantum wires*, Physical Review Letters **105**, 177002 (2010).
- [32] J. Alicea, *New directions in the pursuit of Majorana fermions in solid state systems*, Reports on Progress in Physics **75**, 076501 (2012).
- [33] S. M. Albrecht, A. P. Higginbotham, M. Madsen, F. Kuemmeth, T. S. Jespersen, J. Nygård, P. Krogstrup, and C. M. Marcus, *Exponential protection of zero modes in Majorana islands*, Nature **531**, 206 (2016).
- [34] C. B. Winkelmann, N. Roch, W. Wernsdorfer, V. Bouchiat, and F. Balestro, *Superconductivity in a single-C<sub>60</sub> transistor*, Nature Physics **5**, 876 (2009).
- [35] K. Luo and Z. Yao, *Fabrication of nanometer-spaced superconducting Pb electrodes*, Applied Physics Letters **95**, 113115 (2009).
- [36] A. F. Andreev, *The thermal conductivity of the intermediate state in superconductors*, Soviet Physics JETP **19**, 1823 (1964).
- [37] R. Frisenda, R. Gaudenzi, C. Franco, M. Mas-Torrent, C. Rovira, J. Veciana, I. Alcon, S. T. Bromley, E. Burzurí, and H. S. J. van der Zant, *Kondo effect in a neutral and stable all organic radical single molecule break junction*, Nano Letters **15**, 3109 (2015).
- [38] M. Ballester, *Inert free radicals (IFR): a unique trivalent carbon species*, Accounts of Chemical Research **18**, 380 (1985).
- [39] R. Gaudenzi, J. O. Island, J. De Bruijckere, E. Burzurí, T. M. Klapwijk, and H. S. J. Van der Zant, *Superconducting molybdenum-rhenium electrodes for single-molecule transport studies*, Applied Physics Letters **106**, 222602 (2015).
- [40] K. O'Neill, E. A. Osorio, and H. S. J. Van der Zant, *Self-breaking in planar few-atom Au constrictions for nanometer-spaced electrodes*, Applied Physics Letters **90**, 133109 (2007).
- [41] M. Wolz, C. Debuschewitz, W. Belzig, and E. Scheer, *Evidence for attractive pair interaction in diffusive gold films deduced from studies of the superconducting proximity effect with aluminum*, Physical Review B **84**, 104516 (2011).
- [42] W. Belzig, C. Bruder, and G. Schön, *Local density of states in a dirty normal metal connected to a superconductor*, Physical Review B **54**, 9443 (1996).
- [43] A. A. Clerk and V. Ambegaokar, *Loss of  $\pi$ -junction behavior in an interacting impurity Josephson junction*, Physical Review B **61**, 9109 (2000).



- [44] G. Sellier, T. Kopp, J. Kroha, and Y. S. Barash,  *$\pi$  junction behavior and Andreev bound states in Kondo quantum dots with superconducting leads*, Physical Review B **72**, 174502 (2005).
- [45] R. C. Dynes, V. Narayanamurti, and J. P. Garno, *Direct measurement of quasiparticle-lifetime broadening in a strong-coupled superconductor*, Physical Review Letters **41**, 1509 (1978).
- [46] T. Matsuura, *The effects of impurities on superconductors with Kondo effect*, Progress of Theoretical Physics **57**, 1823 (1977).
- [47] O. Sakai, Y. Shimizu, H. Shiba, and K. Satori, *Numerical renormalization group study of magnetic impurities in superconductors. II. dynamical excitation spectra and spatial variation of the order parameter*, Journal of the Physical Society of Japan **62**, 3181 (1993).



# 6

## THICKNESS DEPENDENT INTERLAYER TRANSPORT IN VERTICAL $\text{MoS}_2$ JOSEPHSON JUNCTIONS

*In this chapter we investigate hybrid devices consisting of a completely different material system, namely, layered van der Waals materials. Specifically, we present observations of thickness dependent Josephson coupling and multiple Andreev reflections (MAR) in vertically stacked molybdenum disulfide ( $\text{MoS}_2$ ) - molybdenum rhenium (MoRe) Josephson junctions. MoRe, a chemically inert superconductor, allows for oxide free fabrication of high transparency vertical  $\text{MoS}_2$  devices. Single and bilayer  $\text{MoS}_2$  junctions display relatively large critical currents (up to  $2.5 \mu\text{A}$ ) and the appearance of sub-gap structure given by MAR. In three and four layer thick devices we observe orders of magnitude lower critical currents (sub-nA) and reduced quasiparticle gaps due to proximitized  $\text{MoS}_2$  layers in contact with MoRe. We anticipate that this device architecture could be easily extended to other 2D materials.*

## 6.1. INTRODUCTION

TRANSITION-METAL dichalcogenides (TMDC), and in particular  $\text{MoS}_2$ , have gained increased attention in the wake of the rise of graphene [2–4]. In contrast with graphene, single-layer  $\text{MoS}_2$  is a semiconductor with a sizable, direct band gap of 1.8 eV [5]. Among the unique attributes of  $\text{MoS}_2$ , perhaps one of its most intriguing features is that the electronic band structure gradually changes with layer number [5–10]. Besides the recent attention on heterostructures [11–15], transport measurements of the layer dependent properties of van der Waals materials have been limited to basal plane transport. Few works study c-axis (across layers) transport [16–19] and the dependence on flake thickness [20]. An interesting direction is the use of the well-known Josephson effect, whereby a supercurrent can flow between two superconductors connected by a tunnel barrier [21, 22], as a probe of the layer dependent electronic properties of  $\text{MoS}_2$  flakes. The Josephson effect is not only uniquely sensitive to the type of weak link (metallic, insulating, and recent van der Waals junctions [23]) but also on the distance between two coupled superconductors. Recent theoretical works predict supercurrent reversal ( $0-\pi$  transition) with back gate doping in planar, monolayer,  $\text{MoS}_2$  Josephson junctions [24] but an experimental observation of Josephson coupling in  $\text{MoS}_2$  junctions has not been reported.

In this chapter we probe the thickness dependence of the interlayer electrical transport in  $\text{MoS}_2$  flakes using the Josephson effect between two coupled molybdenum-rhenium (MoRe) superconductors. In addition to slow oxide growth of MoRe thin films [25], molybdenum itself has been shown to be an excellent contact metal for Schottky barrier-free contact to  $\text{MoS}_2$  [26, 27]. Using this alloy, we fabricate high transparency vertical junctions with 1-4  $\text{MoS}_2$  layers. In single and bilayer devices we observe high critical currents (up to  $2.5 \mu\text{A}$ ) and multiple Andreev reflections (MAR). In trilayer and four layer devices we observe orders of magnitude lower critical currents and the appearance of a reduced quasiparticle gap in the voltage carrying states. We attribute the metallic weak link behavior of the single and bilayer devices to strong hybridization between the MoRe contact and  $\text{MoS}_2$  which leads to metallic  $\text{MoS}_2$  layers [26, 27]. For thicker flakes, transport occurs through first the proximitized layers due to hybridization and then by tunneling through non-hybridized (uncoupled)  $\text{MoS}_2$  layers.

Fabrication of the vertical junctions is accomplished by first exfoliating commercially available  $\text{MoS}_2$  onto a flexible polydimethylsiloxane (PDMS) substrate. Figure 6.1(a) shows a transmission mode optical image of an exfoliated flake on a PDMS stamp. The flake is then transferred onto a Si/SiO<sub>2</sub> substrate with prepatterned MoRe electrodes using an all dry viscoelastic stamping method [28]. The flake lies on top of the MoRe electrode and partially overlaps the SiO<sub>2</sub> substrate below (see Figure 6.1(b)). After transfer, top electrodes are patterned overlapping the flake and the bottom MoRe electrode. Figure 6.1(b) shows the final device after creating the top electrodes with e-beam lithography, sputtering of MoRe, and liftoff in warm acetone. The insets of Figures 6.1(a) and (b) shows a cartoon of the cross section of the device where MoRe electrodes sandwich layers of  $\text{MoS}_2$ . After fabrication, the thickness of the devices is verified using photoluminescence spectroscopy and atomic force microscopy (AFM) measurements on the portion of the flake on the SiO<sub>2</sub> substrate (see section 6.5.1 of the Appendix). We measured nine devices in detail and present transport measurements on junctions having

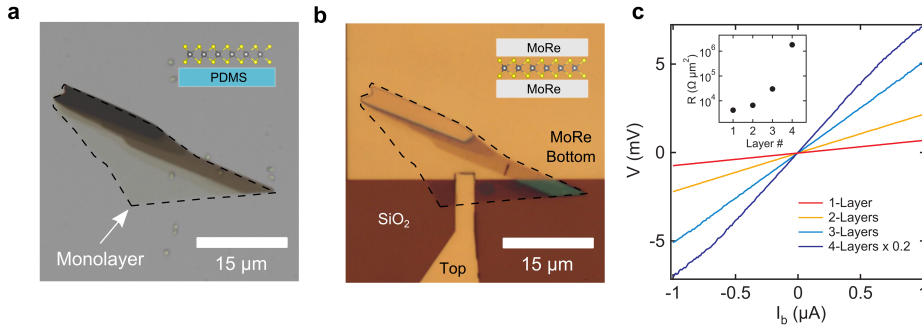


Figure 6.1: **Fabrication of molybdenum-rhenium (MoRe) - molybdenum disulfide ( $\text{MoS}_2$ ) vertical Josephson junctions.** (a) Transmission mode optical image of an exfoliated  $\text{MoS}_2$  flake on a PDMS stamp. (b) Optical image of the same  $\text{MoS}_2$  flake transferred onto a Si/SiO<sub>2</sub> substrate with a prepatterned MoRe bottom electrode. After transfer, a top electrode is patterned to sandwich the  $\text{MoS}_2$  flake (see inset). (c) Room temperature voltage ( $V$ ) as a function of current bias ( $I_b$ ) for junctions with 1-4 layers of  $\text{MoS}_2$  (devices A-D, respectively).

1-4 layers of  $\text{MoS}_2$ . All low temperature (30 mK - 1.2 K) measurements were performed using four terminal current bias configuration in a dilution fridge equipped with copper powder and RC filters. Figure 6.1(c) shows the room temperature characteristics of four devices after fabrication having 1 to 4 layers (henceforth named devices A through D, respectively). The measured voltage ( $V$ ) is plotted as a function of current bias ( $I_b$ ). In the inset we plot the zero bias resistance at room temperature (normalized to the area) as a function the number of layers. The data do not follow a simple exponential dependence as would be expected for pure tunneling through a barrier. The Josephson effect, being sensitive to the type of weak link (metallic or tunnel barrier), provides us with a clear explanation of the layer dependence below.

## 6.2. SINGLE-LAYER $\text{MoS}_2$ JOSEPHSON JUNCTIONS

We now turn to the low temperature characteristics of the vertical MoRe- $\text{MoS}_2$  junctions. Figure 6.2 shows transport measurements for a junction with a monolayer  $\text{MoS}_2$  flake (Device E) at 30 mK. A measurement of the voltage ( $V$ ) across the junction as a function of  $I_b$  (Figure 6.2(a)) reveals a supercurrent that switches to the normal state at  $2.5 \mu\text{A}$ . By irradiating the junction with an RF field, we observe the appearance of Shapiro steps signaling the coupling of the Josephson junction to the RF field [22, 29]. The inset of Figure 6.2(a) shows a color map of the differential resistance ( $dV/dI$ ) as a function of  $I_b$  (vertical axis) and RF power (horizontal axis). As the power is increased, more Shapiro steps enter the bias window. Additionally, we measure the junction response to an external magnetic field up to 12 T applied parallel to the junction sandwich (see section 6.5.2 of the Appendix). An overall decrease of the critical current is distinguished for fields parallel to the sandwich but the magnetic field dependence for all devices studied shows stochastic switching of the critical current. As the experiments are performed far above the first critical field of MoRe, the presences of pinned vortices in the disordered superconducting leads could be responsible for such strong switching behavior in the critical

current. We further conjecture that flux focusing and corrugations in the surface texture of the MoRe electrodes further complicate the magnetic field response.

Now turning to the voltage carrying state, in Figure 6.2(b) we plot  $V$  vs.  $I_b$  at higher bias currents for device A (at 30 mK). The curve becomes nonlinear below voltages of  $\pm \approx 3$  mV. These nonlinear features are more clearly resolved in the differential conductance plotted in Figure 6.2(c) as a function of  $V$ . Symmetric peaks are observed at  $\pm 2.6$  mV marking the onset of quasiparticle transport. Additionally, sub-gap conductance peaks are observed symmetric in voltage (see black arrows in Figure 6.2(c)). We attribute these sub-gap peaks to the well-known Andreev reflection process that takes place at the interface between a superconductor and a metal[30, 31]. The positions of the peaks in energy for multiple Andreev reflections (MAR) are given by  $eV_n = 2\Delta/n$ , where  $n$  is a positive integer. In Figure 6.2(d) we plot the peak positions as a function of  $1/n$ . A linear fit to the average peak position results in a bulk superconducting gap estimate of  $\Delta = 1.3$  meV. Assuming MoRe is a BCS superconductor ( $\Delta = 1.76k_B T_c$ )[22], this estimate corresponds to a  $T_c$  of 8.6 K which agrees closely with reported values for MoRe thin films [32–34]. MAR up to  $n = 4$  suggests relatively transparent transport barriers (transparencies between  $\approx 10\%$  and  $100\%$ ). We estimate the transparency of the interfaces given the excess current of the junction[35]. The excess current is the extrapolated current at  $V = 0$  V from a fit to the normal state current vs. voltage (see dotted line in Figure 6.2(b), here the fit is between 5 and 10 mV). For this single layer device we extract an excess current of  $4.6 \mu\text{A}$  which corresponds to a contact transparency of  $\approx 80\%$  [35]. Similar high transparencies have been observed in Ge/Si[36] and InAs[37] Josephson junctions where Schottky barrier-free contact could be achieved.

### 6.3. THICKNESS DEPENDENCE

In Figure 6.3 we present the low temperature layer dependence of the Josephson coupling for devices A-D having 1-4 layers. Figure 3(a-d) shows the  $V - I_b$  curves for four devices measured at 1.2 K. The critical current decreases with increasing thickness but more importantly, we distinguish between relatively high critical currents for the single and bilayer devices and several orders of magnitude lower critical currents for the three and four layer junctions (see section 6.5.3 of the Appendix for critical current densities following the same trend and  $I_c R_n$  products as a function of layer number). The voltage carrying state provides further insight on the layer dependence. In Figure 6.3(e-h) we plot  $dI/dV$  for higher current biases measured at 30 mK for devices A-D. The dotted lines mark the bulk superconducting gap edge ( $2\Delta = 2.6$  mV). While the single and bilayer junctions present high transparencies that give rise to MAR, the three and four layer junctions present opaque barriers resulting in the appearance of more well-defined quasiparticle gaps. We now discuss each regime in detail.

Starting with the single layer device (Figures 6.3(e)), the sharp coherence peaks that align well with the bulk superconducting gap and the presence of MAR indicate a high transparency, metallic weak link. A possible explanation for this metallic behavior is doping of the  $\text{MoS}_2$  flakes due to direct contact with the MoRe electrodes. Recently, Kang et al. have shown that molybdenum contacts provide tunnel barrier-free and Schottky barrier-free contact to  $\text{MoS}_2$  flakes [26]. In particular, DFT calculations show that due to the strong orbital overlap between Mo atoms in the electrode and the  $\text{MoS}_2$  flake,

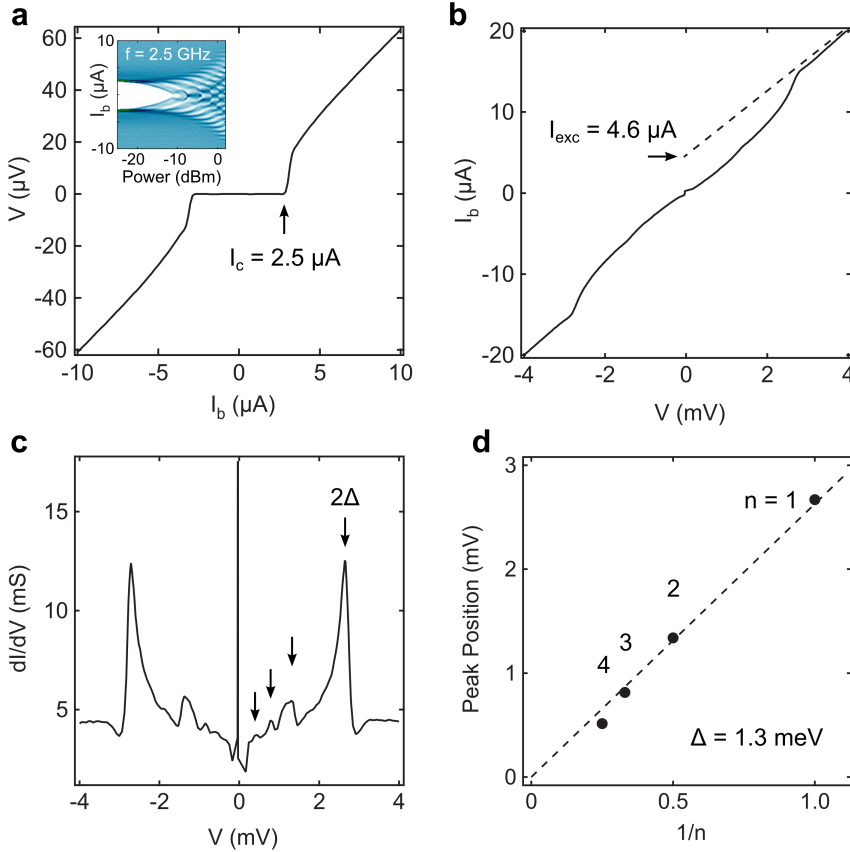


Figure 6.2: **Single-layer MoS<sub>2</sub> Josephson junctions.** (a) Plot of the measured voltage ( $V$ ) as a function of current bias ( $I_b$ ) for a single layer device (device E). Critical current of the junction is  $2.5 \mu\text{A}$ . The inset shows the Shapiro steps ( $dV/dI$  vs.  $I_b$ ) as a function of RF power signaling the Josephson nature of the junction. The frequency of the irradiated field is  $2.5 \text{ GHz}$ . (b)  $I_b$  vs.  $V$  for device A. The excess current ( $I_{\text{exc}} = 4.6 \mu\text{A}$ ) is extrapolated from a fit (red dotted line) to the curve from  $5 - 10 \text{ mV}$  in the normal state. (c) Calculated differential conductance ( $dI/dV$ ) as a function of  $V$  for device A from data in panel (b). The arrows mark the conductance peaks arising from MAR. (d) The average peak position as a function of  $1/n$  for device A, where  $n$  is an integer and corresponds to the number of Andreev reflections. The dotted line is a linear fit to the data which estimates a superconducting gap of  $\Delta = 1.3 \text{ meV}$ . All measurements taken at  $30 \text{ mK}$

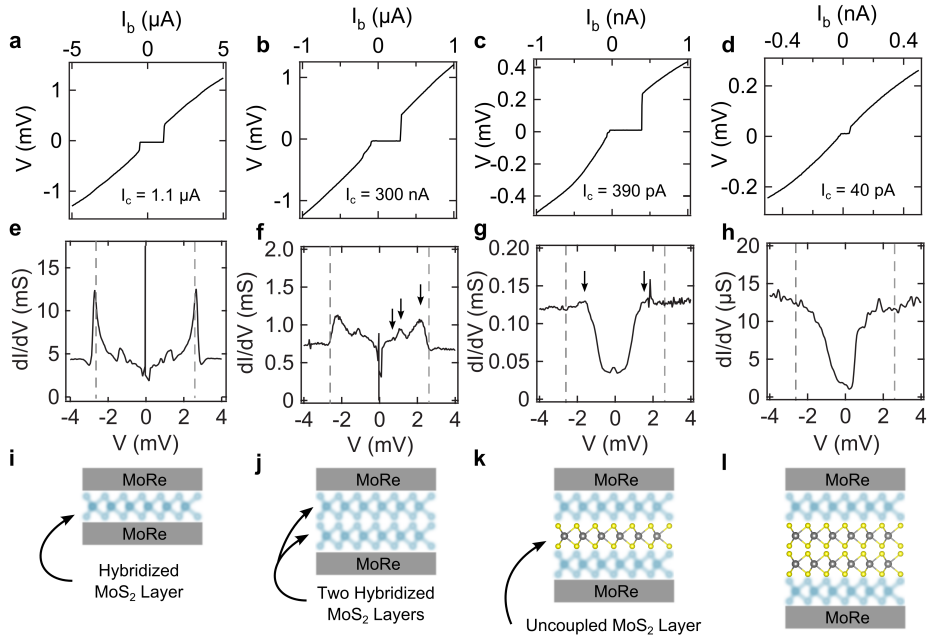


Figure 6.3: **Thickness dependent Josephson coupling.** (a-d) Current bias sweeps at 1.2 K for devices A-D having 1-4 layers of  $\text{MoS}_2$ , respectively. (e-h) Differential conductance ( $dI/dV$ ) vs.  $V$  for devices A-D having 1-4 layers of  $\text{MoS}_2$ , respectively, taken at 30 mK. Panel (e) is the same data in Figure 2(c) plotted here for comparison. (i-l) Simple models explaining the layer dependence for each junction having 1-4 layers, respectively. The blurry blue  $\text{MoS}_2$  layers represent the hybridization with the  $\text{MoRe}$  contacts suggested in the text.



the nearest single layer in top contacted devices becomes metallic [26, 27]. Subsequent layers below the top contacted layer remain semiconducting. A model of this scenario for the single layer device is shown in Figure 6.3(i) where the hybridized layer is colored blue. This is a reasonable explanation for the metallic behavior we observe which is supported below for the thicker devices as well. Additionally however, it should be noted that the presence of defects[38–40] in the MoS<sub>2</sub> layers could give rise to metallic pinholes that would provide high transparency transport through the junction. A simple estimate for the size of a prospective pinhole can be made from the Sharvin resistance, the resistance of a metallic point contact:  $R_s = 4\rho l/3\pi a^2$ , where  $\rho$  is the resistivity of the metal,  $l$  is the mean free path of carriers, and  $a$  is the radius of the point contact[41, 42]. If we assume the single layer devices are undoped semiconducting layers with pinholes, for our single layer devices (A and E), we estimate point contact radii of 1 nm and 2.5 nm, respectively (taking, for simplicity, a resistivity and mean free path of  $\rho \approx 5 \Omega\mu\text{m}$  and  $l \approx 10$  nm for molybdenum[43]). These estimates are possible given the size of reported defects in exfoliated MoS<sub>2</sub>[40]. Further investigation (junction statistics and cross sectional TEM) is required to determine the presence of pinholes in the high transparency junctions.

The bilayer device (Figures 6.3(b, f, j)), also presenting high transparency ( $\approx 80\%$ ), indicates metallic weak link behavior. From the MAR conductance peaks (Figure 6.3(f)), following the analysis for device A in Figure 6.2(d), we estimate a reduced superconducting gap of  $\Delta' = 1.1$  meV, slightly lower than the bulk value of  $\Delta = 1.3$  meV from the single layer device. This indicates a thicker metallic link between the superconducting banks as compared with the single layer devices. Additionally, the magnetic field dependence shows better resolved oscillations of  $I_c$  which point to more homogeneous current distributions (see section 6.5.2 of the Appendix). In the bilayer case, each layer is coupled to the nearest MoRe electrode providing transport through two hybridized MoS<sub>2</sub> layers (Figure 6.3(j)).

Finally, the trilayer and four layer devices show the expected tunneling behavior through an undoped semiconductor. The formation of a reduced quasiparticle gap (black arrows in Figure 6.3(g)) adds support to the hybridization model above. Quasiparticles tunnel from the reduced gap in the hybridized layer through a central undoped semiconducting layer (see Figure 6.3(k) for a simple model) which provides the tunnel barrier. This is reminiscent of earlier niobium junctions with a thin aluminum layer resulting in a reduced gap[44]. The four layer device (Figures 6.3(d, h, i)) follows this trend with a deeper quasiparticle gap. These simple models qualitatively explain the layer dependence of the presented junctions.

## 6.4. CONCLUSION

In conclusion, we have presented interlayer transport measurements on vertical MoRe-MoS<sub>2</sub>-MoRe Josephson junctions. We found that the transport characteristics are dependent on the number of MoS<sub>2</sub> layers between the MoRe electrodes and, in particular, we observe a threshold between metallic-like weak link behavior and tunneling-like weak link behavior occurring between the bilayer and trilayer flake thicknesses. We propose that the metallic characteristics (appearance of MAR) of the single and bilayer devices are due to hybridization with the electrodes, as suggested in literature, that results in metalized MoS<sub>2</sub> layers. In the three and four layer devices the uncoupled layers (not

directly in contact with the MoRe contacts) provide a tunnel barrier which reduces the critical current densities and results in more well-defined quasiparticle transport gaps. We anticipate the extension of this device architecture to other 2D materials and an interesting technological direction would be the use of insulating boron-nitride layers as uniform tunnel barriers replacing the standard  $\text{AlO}_x$  barrier where less than 10% of the barrier area is active in transport [45].

## 6.5. APPENDIX

### 6.5.1. PHOTOLUMINESCENCE (PL) AND ATOMIC FORCE MICROSCOPY (AFM) DETERMINATION OF FLAKE THICKNESS

Figure 6.4 shows optical images, AFM profile scans, and PL spectra for devices having thicknesses of 1-4  $\text{MoS}_2$  layers. Figure 6.4(a) shows three junctions fabricated using a flake having a single layer and bi layer region. The AFM line scans (take at the location of the dotted white lines in Figure 6.4(a)) are shown in Figure 6.4(c) and correspond to single and bilayer flakes. Additionally, Raman normalized PL spectra taken at the same approximate locations of the AFM scans in Figure 6.4(a) are shown in Figure S1(d). The monolayer flake has a much stronger PL spectra due to the direct band gap nature as reported in literature. Adding more layers results in a more indirect band gap and weaker PL response. Figure 6.4(b) shows two junctions fabricated using a flake with three and four layers. The corresponding AFM scans and PL spectra are shown in Figure 6.4(c) and 6.4(d) respectively.

### 6.5.2. MAGNETIC FIELD DEPENDENCE OF THE CRITICAL CURRENT

Figure 6.5 shows the magnetic field dependence for devices E, A and B, two single layer and one bilayer  $\text{MoS}_2$  junction. The field is applied parallel to the sandwich, allowing flux to penetrate the  $\text{MoS}_2$  flake. Ideally, such measurements could reveal information about the spatial uniformity of the critical current in the junctions. However, all three devices show a stochastic switching of the critical current as a function of magnetic field, which we attribute to motions of pinned vortices in the disordered superconducting MoRe leads at fields far above the first critical field ( $H_{c1}$ ) of the type-II superconductor.

### 6.5.3. CRITICAL CURRENT DENSITIES AND $I_c R_n$ PRODUCTS AS A FUNCTION OF LAYER NUMBER

The critical current densities, like the critical currents, for each junction decrease with increasing layer number (see Figure 6.6(a)). The single and bilayer devices are orders of magnitude higher than the trilayer device indicating the crossover to tunneling suggested in the main text. The  $I_c R_n$  products for each device are shown in Figure 6.6(b) scaled by the superconducting gaps where we have used the bulk value for the single layer device and the proximity induced values for the 2, 3, and 4 layer devices ( $\Delta = 1.3$  meV, 1.1 meV,  $\Delta = 0.75$  meV, 0.6 meV for devices A-D respectively).

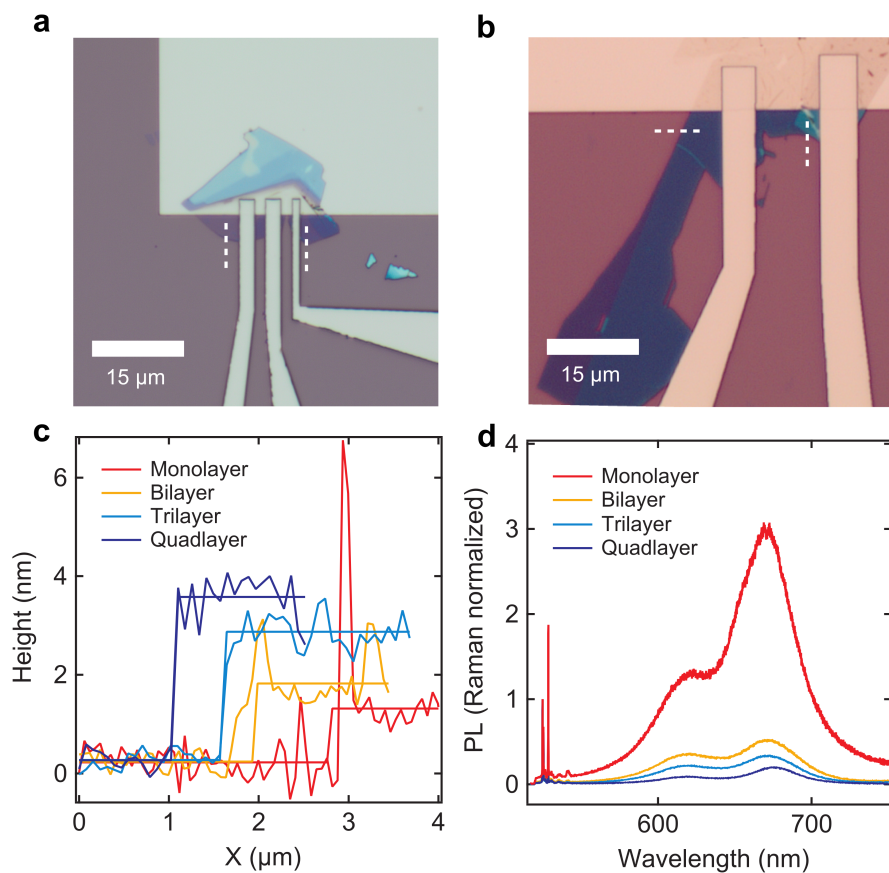


Figure 6.4: (a) Optical image of three junctions made from an MoS<sub>2</sub> flake having a single layer (left junction) and bilayer regions (right junction). (b) Optical image of two junctions fabricated with MoS<sub>2</sub> flakes having three (left junction) and four layers (right junction). (c) AFM line profiles taken at the positions of the dotted lines in panels (a) and (b). (d) PL spectra recorded at the approximate locations of the AFM scans in panel (a) and (b).

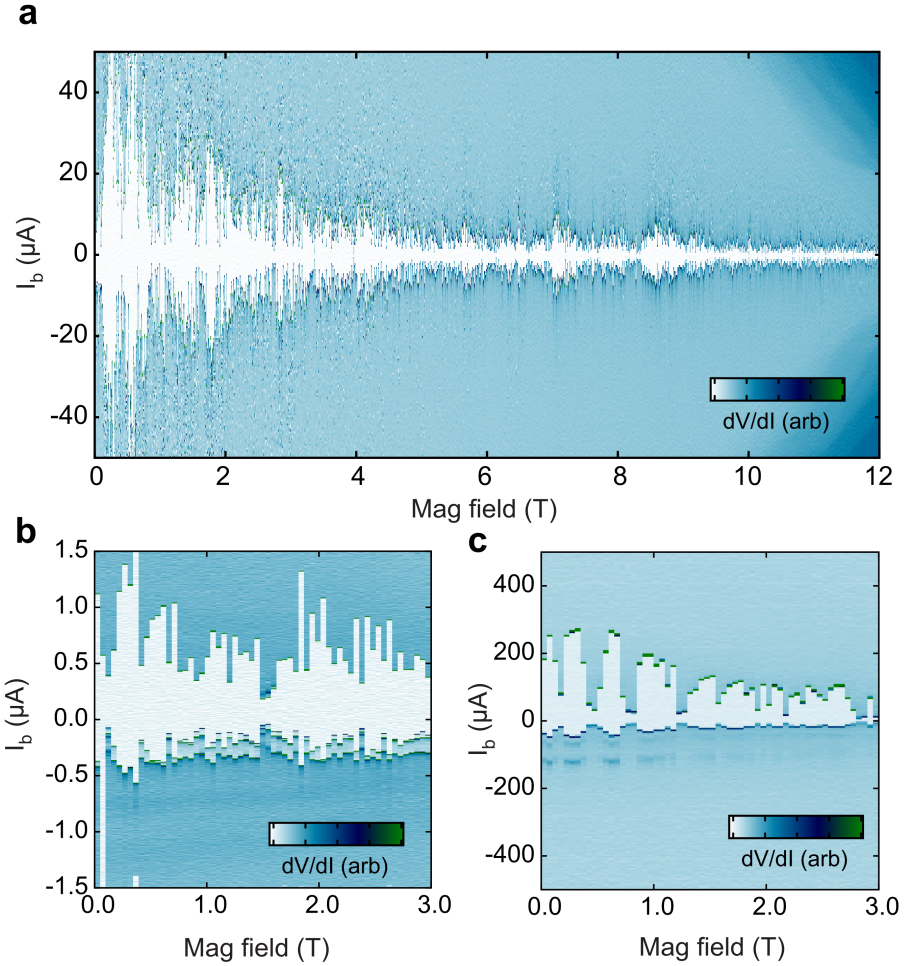


Figure 6.5: (a) Color plot of the magnetic field dependence of device E with field applied parallel to the junction sandwich. The differential conductance ( $dI/dV$ ) is plotted as a function of current bias and magnetic field. (b) Same plot for device A. (c) Same plot for device B.

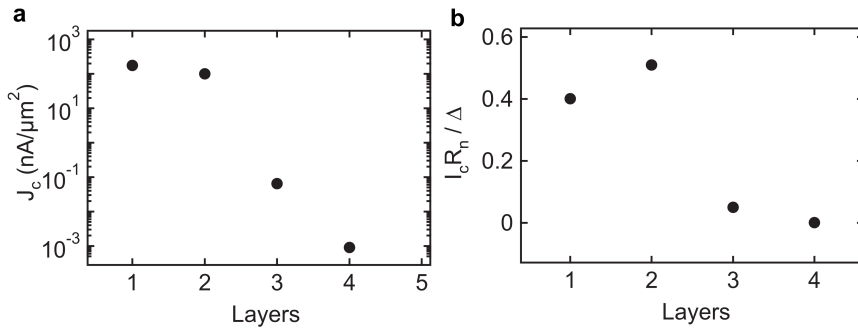


Figure 6.6: (a) Critical current densities for devices A-D having 1-4 layers respectively. (b)  $I_c R_n$  products normalized by the superconducting gap as a function of layer number for devices A-D.

## REFERENCES

- [1] J. O. Island, G. A. Steele, H. S. J. van der Zant, and A. Castellanos-Gomez, *Thickness dependent interlayer transport in vertical MoS<sub>2</sub> Josephson junctions*, *2D Materials* **3**, 031002 (2016).
- [2] Q. H. Wang, K. Kalantar-Zadeh, A. Kis, J. N. Coleman, and M. S. Strano, *Electronics and optoelectronics of two-dimensional transition metal dichalcogenides*, *Nature Nanotechnology* **7**, 699 (2012).
- [3] S. Z. Butler, S. M. Hollen, L. Cao, Y. Cui, J. A. Gupta, H. R. Gutierrez, T. F. Heinz, S. S. Hong, J. Huang, and A. F. Ismach, *Progress, challenges, and opportunities in two-dimensional materials beyond graphene*, *ACS Nano* **7**, 2898 (2013).
- [4] M. Buscema, J. O. Island, D. J. Groenendijk, S. I. Blanter, G. A. Steele, H. S. J. van der Zant, and A. Castellanos-Gomez, *Photocurrent generation with two-dimensional van der Waals semiconductors*, *Chemical Society Reviews* **44**, 3691 (2015).
- [5] K. F. Mak, C. Lee, J. Hone, J. Shan, and T. F. Heinz, *Atomically thin MoS<sub>2</sub>: a new direct-gap semiconductor*, *Physical Review Letters* **105**, 136805 (2010).
- [6] A. Splendiani, L. Sun, Y. Zhang, T. Li, J. Kim, C.-Y. Chim, G. Galli, and F. Wang, *Emerging photoluminescence in monolayer MoS<sub>2</sub>*, *Nano Letters* **10**, 1271 (2010).
- [7] G. Eda, H. Yamaguchi, D. Voiry, T. Fujita, M. Chen, and M. Chhowalla, *Photoluminescence from chemically exfoliated MoS<sub>2</sub>*, *Nano Letters* **11**, 5111 (2011).
- [8] W. Jin, P.-C. Yeh, N. Zaki, D. Zhang, J. T. Sadowski, A. Al-Mahboob, A. M. van Der Zande, D. A. Chenet, J. I. Dadap, and I. P. Herman, *Direct measurement of the thickness-dependent electronic band structure of MoS<sub>2</sub> using angle-resolved photoemission spectroscopy*, *Physical Review Letters* **111**, 106801 (2013).
- [9] H. S. Lee, S.-W. Min, Y.-G. Chang, M. K. Park, T. Nam, H. Kim, J. H. Kim, S. Ryu, and S. Im, *MoS<sub>2</sub> nanosheet phototransistors with thickness-modulated optical energy gap*, *Nano Letters* **12**, 3695 (2012).
- [10] D. Lembke, A. Allain, and A. Kis, *Thickness-dependent mobility in two-dimensional MoS<sub>2</sub> transistors*, *Nanoscale* **7**, 6255 (2015).
- [11] L. Britnell, R. V. Gorbachev, R. Jalil, B. D. Belle, F. Schedin, A. Mishchenko, T. Georgiou, M. I. Katsnelson, L. Eaves, S. Morozov, *et al.*, *Field-effect tunneling transistor based on vertical graphene heterostructures*, *Science* **335**, 947 (2012).
- [12] S. J. Haigh, A. Gholinia, R. Jalil, S. Romani, L. Britnell, D. C. Elias, K. S. Novoselov, L. A. Ponomarenko, A. K. Geim, and R. Gorbachev, *Cross-sectional imaging of individual layers and buried interfaces of graphene-based heterostructures and superlattices*, *Nature Materials* **11**, 764 (2012).
- [13] T. Georgiou, R. Jalil, B. D. Belle, L. Britnell, R. V. Gorbachev, S. V. Morozov, Y.-J. Kim, A. Gholinia, S. J. Haigh, O. Makarovskiy, *et al.*, *Vertical field-effect transistor based*

- on graphene-WS<sub>2</sub> heterostructures for flexible and transparent electronics*, Nature Nanotechnology **8**, 100 (2013).
- [14] W. J. Yu, Z. Li, H. Zhou, Y. Chen, Y. Wang, Y. Huang, and X. Duan, *Vertically stacked multi-heterostructures of layered materials for logic transistors and complementary inverters*, Nature Materials **12**, 246 (2013).
- [15] A. K. Geim and I. V. Grigorieva, *Van der Waals heterostructures*, Nature **499**, 419 (2013).
- [16] Y.-H. Lee, Y.-J. Kim, and J.-H. Lee, *Vertical conduction behavior through atomic graphene device under transverse electric field*, Applied Physics Letters **98**, 133112 (2011).
- [17] G.-H. Lee and H.-J. Lee, *Josephson coupling realized in graphite-based vertical junction*, Applied Physics Express **6**, 025102 (2013).
- [18] L.-N. Nguyen, Y.-W. Lan, J.-H. Chen, T.-R. Chang, Y.-L. Zhong, H.-T. Jeng, L.-J. Li, and C.-D. Chen, *Resonant tunneling through discrete quantum states in stacked atomic-layered MoS<sub>2</sub>*, Nano Letters **14**, 2381 (2014).
- [19] G.-H. Lee, S. Kim, S.-H. Jhi, and H.-J. Lee, *Ultimately short ballistic vertical graphene josephson junctions*, Nature Communications **6**, 6181 (2015).
- [20] R. Moriya, T. Yamaguchi, Y. Inoue, S. Morikawa, Y. Sata, S. Masubuchi, and T. Machida, *Large current modulation in exfoliated-graphene/MoS<sub>2</sub>/metal vertical heterostructures*, Applied Physics Letters **105**, 083119 (2014).
- [21] B. D. Josephson, *Possible new effects in superconductive tunnelling*, Physics Letters **1**, 251 (1962).
- [22] M. Tinkham, *Introduction to superconductivity* (Dover, 2004).
- [23] N. Yabuki, R. Moriya, M. Arai, Y. Sata, S. Morikawa, S. Masubuchi, and T. Machida, *Supercurrent in van der Waals Josephson junction*, Nature Communications **7**, 10616 (2016).
- [24] B. Z. Rameshti, A. G. Moghaddam, and M. Zareyan, *Gate-controlled supercurrent reversal in MoS<sub>2</sub>-based Josephson junctions*, Europhysics Letters **108**, 37002 (2014).
- [25] V. A. Seleznev, M. A. Tarkhov, B. M. Voronov, I. I. Milostnaya, V. Y. Lyakhno, A. Garbuz, M. Y. Mikhailov, O. M. Zhigalina, and G. N. Gol'tsman, *Deposition and characterization of few-nanometers-thick superconducting Mo-Re films*, Superconductor Science and Technology **21**, 115006 (2008).
- [26] J. Kang, W. Liu, and K. Banerjee, *High-performance MoS<sub>2</sub> transistors with low-resistance molybdenum contacts*, Applied Physics Letters **104**, 093106 (2014).
- [27] J. Kang, W. Liu, D. Sarkar, D. Jena, and K. Banerjee, *Computational study of metal contacts to monolayer transition-metal dichalcogenide semiconductors*, Physical Review X **4**, 031005 (2014).

- [28] A. Castellanos-Gomez, M. Buscema, R. Molenaar, V. Singh, L. Janssen, H. S. J. van der Zant, and G. A. Steele, *Deterministic transfer of two-dimensional materials by all-dry viscoelastic stamping*, *2D Materials* **1**, 011002 (2014).
- [29] S. Shapiro, *Josephson currents in superconducting tunneling: the effect of microwaves and other observations*, *Physical Review Letters* **11**, 80 (1963).
- [30] A. F. Andreev, *Thermal conductivity of the intermediate state of superconductors*, *Soviet Physics JETP* **19**, 1228 (1964).
- [31] T. M. Klapwijk, G. E. Blonder, and M. Tinkham, *Explanation of subharmonic energy gap structure in superconducting contacts*, *Physica B+ C* **109**, 1657 (1982).
- [32] M. J. Witcomb and D. Dew-Hughes, *The  $\sigma$ -phase in molybdenum-rhenium; microstructure and superconducting hysteresis*, *Journal of the Less Common Metals* **31**, 197 (1973).
- [33] V. A. Seleznev, M. A. Tarkhov, B. M. Voronov, I. I. Milostnaya, V. Y. Lyakhno, A. S. Garbuz, M. Y. Mikhailov, O. M. Zhigalina, and G. N. Gol'tsman, *Deposition and characterization of few-nanometers-thick superconducting Mo-Re films*, *Superconductor Science and Technology* **21**, 115006 (2008).
- [34] V. Singh, B. H. Schneider, S. J. Bosman, E. P. J. Merks, and G. A. Steele, *Molybdenum-rhenium alloy based high-Q superconducting microwave resonators*, *Applied Physics Letters* **105**, 222601 (2014).
- [35] G. E. Blonder, M. Tinkham, and T. M. Klapwijk, *Transition from metallic to tunneling regimes in superconducting microconstrictions: Excess current, charge imbalance, and supercurrent conversion*, *Physical Review B* **25**, 4515 (1982).
- [36] J. Xiang, A. Vidan, M. Tinkham, R. M. Westervelt, and C. M. Lieber, *Ge/Si nanowire mesoscopic Josephson junctions*, *Nature Nanotechnology* **1**, 208 (2006).
- [37] Y.-J. Doh, J. A. van Dam, A. L. Roest, E. P. A. M. Bakkers, L. P. Kouwenhoven, and S. De Franceschi, *Tunable supercurrent through semiconductor nanowires*, *Science* **309**, 272 (2005).
- [38] W. Zhou, X. Zou, S. Najmaei, Z. Liu, Y. Shi, J. Kong, J. Lou, P. M. Ajayan, B. I. Yakobson, and J.-C. Idrobo, *Intrinsic structural defects in monolayer molybdenum disulfide*, *Nano Letters* **13**, 2615 (2013).
- [39] J. Hong, Z. Hu, M. Probert, K. Li, D. Lv, X. Yang, L. Gu, N. Mao, Q. Feng, and L. Xie, *Exploring atomic defects in molybdenum disulphide monolayers*, *Nature Communications* **6**, 6293 (2015).
- [40] R. Addou, L. Colombo, and R. M. Wallace, *Surface defects on natural MoS<sub>2</sub>*, *ACS Applied Materials & Interfaces* **7**, 11921 (2015).
- [41] Y. V. Sharvin, *On the possible method for studying fermi surfaces*, *Soviet Physics JETP* **48**, 984 (1965).



- [42] A. G. M. Jansen, A. P. Van Gelder, and P. Wyder, *Point-contact spectroscopy in metals*, Journal of Physics C: Solid State Physics **13**, 6073 (1980).
- [43] J. Yamashita and S. Asano, *Electrical resistivity of transition metals. I*, Progress of Theoretical Physics **51**, 317 (1974).
- [44] M. Gurvitch, M. A. Washington, and H. A. Huggins, *High quality refractory Josephson tunnel junctions utilizing thin aluminum layers*, Applied Physics Letters **42**, 472 (1983).
- [45] L. J. Zeng, S. Nik, T. Greibe, C. M. Wilson, P. Delsing, and E. Olsson, *Direct observation of the thickness distribution of ultra thin  $AlO_x$  barrier in  $Al/AlO_x/Al$  Josephson junctions*, Journal of Physics D: Applied Physics **48**, 395308 (2015).



# 7

## ENHANCED SUPERCONDUCTIVITY IN ATOMICALLY-THIN $\text{TaS}_2$

*The ability to exfoliate layered materials down to the single layer limit has opened the opportunity to understand how a gradual reduction in dimensionality affects the properties of bulk materials. Here we use this top-down approach to address the problem of superconductivity in the two-dimensional limit. The transport properties of electronic devices based on 2H tantalum disulfide flakes of different thicknesses are presented. We observe that superconductivity persists down to the thinnest layer investigated (3.5 nm), and interestingly, we find a pronounced enhancement in the critical temperature from 0.5 K to 2.2 K as the layers are thinned down. In addition, we propose a tight-binding model, which allows us to attribute this phenomenon to an enhancement of the effective electron-phonon coupling constant. This work provides evidence that reducing dimensionality can strengthen superconductivity as opposed to the weakening that has been reported in other 2D materials so far.*

---

Parts of this chapter have been published in Nature Communications 7, 11043 (2016)[\[1\]](#)

## 7.1. INTRODUCTION

THE behavior of superconductors in the two-dimensional (2D) limit is a long-standing interest in physics that has been the focus of extensive research in the field[2–7]. The bottom-up approach has provided signs of the existence of superconductivity at the 2D limit in experiments performed on in situ grown, ultrathin lead films fabricated by evaporation[8, 9]. However, for films grown in this way, it is difficult to avoid the strong influence from the substrate lattice, yielding typically highly disordered films. A different approach takes advantage of the ability of certain van der Waals materials to be separated into individual layers, which may later be isolated as defect-free 2D crystals on a substrate of choice[10]. This top-down approach permits overcoming the lattice and chemical restrictions imposed by the substrate in the bottom-up strategy in such a way that the coupling may be minimized by an appropriate choice of surface[11–13].

Although graphene is not an intrinsic superconductor, recent studies have brought forward the possibility of inducing superconductivity in this 2D material by garnishing its surface with the right species of dopant atoms or, alternatively, by using ionic liquid gating[14, 15]. However, reported experiments have failed to show direct evidence of superconducting behavior in exfoliated graphene, leaving out the archetypal material from studies of 2D superconductivity[16].

An even more attractive family of 2D materials is provided by the transition metal dichalcogenides (TMDCs) as some of its members exhibit superconductivity in bulk[17, 18]. Just as in graphene, TMDCs present a strong in-plane covalency and weak inter-layer van der Waals interactions which allow exfoliation of the bulk[19]. This has given rise to a very rich chemistry of hybrid multifunctional materials based on the restacking of TMDC nanolayer sols with functional counterparts[20, 21]. In a different approach, all-dry exfoliation methodologies have allowed for the deposition of TMDC flakes on a variety of surfaces[10, 22]. These micromechanical exfoliation techniques allow access to nearly defect-free, large surface area flakes of virtually any TMDC, opening the door to the study of how a reduction in dimensionality affects the properties of these materials[23–26]. Surprisingly, despite the works reported in the literature searching for intrinsic superconductivity in atomically-thin 2D crystals[27–29] for a long time the sole examples came from iron selenide (FeSe) thin films grown in situ on a substrate[30–33]. Very recently, several studies of niobium diselenide ( $\text{NbSe}_2$ ) flakes have yielded the first clear evidence of the existence of superconductivity in freshly cleaved specimens of less than three layers in thickness[34–37].

Tantalum disulfide ( $\text{TaS}_2$ ) is another member of the TMDC family. In its bulk state,  $\text{TaS}_2$  is composed of robust covalently bonded S-Ta-S planes that stack upon each other. A variety of polytypic phases originate from the distinct in-plane Ta coordination spheres described by the S<sub>2</sub>-ligands and by the stacking periodicity of the individual planes. For instance, the 2H and 1T polytypes present unit cells with two trigonal bipyramidal and one octahedral Ta coordinated layers, respectively. Though extensively explored in the 1960s[38], 1T and 2H polytypes are once again attracting major attention since they constitute ideal case studies for the investigation of competing orders, namely, superconductivity, charge density waves (CDW)[39, 40], and hidden phases[41]. In this scenario, the study of decoupled or isolated  $\text{TaS}_2$  layers may provide new insights into these exotic phenomena[42]. Transport measurements of few-layer  $\text{TaS}_2$  flakes have been reported

in flakes as thin as 2 nm, but superconductivity in TaS<sub>2</sub> layers thinner than 8 nm has not been observed, probably due to the environmental degradation of the samples[43].

Here, we explore 2D superconductivity in few-molecular-layer tantalum disulfide flakes of different thicknesses, which have been mechanically exfoliated onto Si/SiO<sub>2</sub> substrates. Interestingly, we observe that superconductivity persists down to the thinnest layer investigated (3.5 nm, ca. 5 covalent planes), with a pronounced increase in the critical temperature ( $T_c$ ) from 0.5 K (bulk crystal) to approximately 2.2 K when the thickness of the layer is decreased. In search of the origin of these observations, we perform Density Functional Theory (DFT) calculations and construct a simple tight binding model to study the change in the electronic band structure and density of states (DOS) at the Fermi level as a function of reduced thickness. We ascribe the enhancement to an increase in the effective coupling constant ( $\lambda_{eff}$ ) for reduced thicknesses, which ultimately determines  $T_c$ .

## 7.2. GROWTH AND FABRICATION

While the exfoliation of other TMDC members has been extensively studied, little has been reported on the controlled isolation of atomically thin TaS<sub>2</sub> flakes. This layered material appears to be difficult to exfoliate and is also particularly susceptible to oxidation in atmospheric conditions[44], hindering the manipulation of very thin flakes in open moist air. Though complex encapsulation techniques help in preserving samples from oxidation[36], we find that a rapid integration of freshly exfoliated flakes into final devices and their immediate transfer to vacuum conditions for measurement also permits retaining the pristine properties of most TaS<sub>2</sub> samples.

The experimental process begins with the chemical vapor transport growth of bulk TaS<sub>2</sub> crystals. Polycrystalline 2H-TaS<sub>2</sub> is synthesized by heating stoichiometric quantities of Ta and S in an evacuated quartz ampule at 900 °C for 9 days. The growth of large single crystals from the polycrystalline sample was achieved by employing a three-zone furnace. The powder sample is placed in the leftmost zone of the furnace and the other two zones are initially brought to 875 °C and kept at that temperature for 1 day. Following this, the temperature of the source zone is risen to 800 °C during the course of 3 hours. The temperature of the center zone is then gradually cooled down at a speed of 1 °C min<sup>-1</sup> until a gradient of 125 °C is finally established between the leftmost (875 °C) and centre (750 °C) zones. A gradient of 50 °C was also set between the rightmost and growth zones. This temperature gradient was maintained for 120 hours and the furnace was then switched off and left to cool down naturally. The crystals were then thoroughly rinsed with diethyl ether and stored under in a nitrogen gas atmosphere.

Subsequently the bulk material is exfoliated onto Si/SiO<sub>2</sub> substrates. To ensure high-quality material, optical, Raman, and atomic force microscopy (AFM) characterization was performed on varying thicknesses of exfoliated flakes (see sections 7.5.1-7.5.2 in the Appendix). As already established for graphene and other TMDCs, inspection of the substrate surface by optical microscopy permits identifying the presence of nanometer thin TaS<sub>2</sub> flakes. In an attempt to access flakes with a reduced number of atomic layers we developed a modification of the micromechanical exfoliation method and optimized it for the controlled isolation of few-layer 2H-TaS<sub>2</sub> flakes[45, 46]. The method relies on precisely controlling a uniaxial pressure applied directly with a single crystal over the ac-

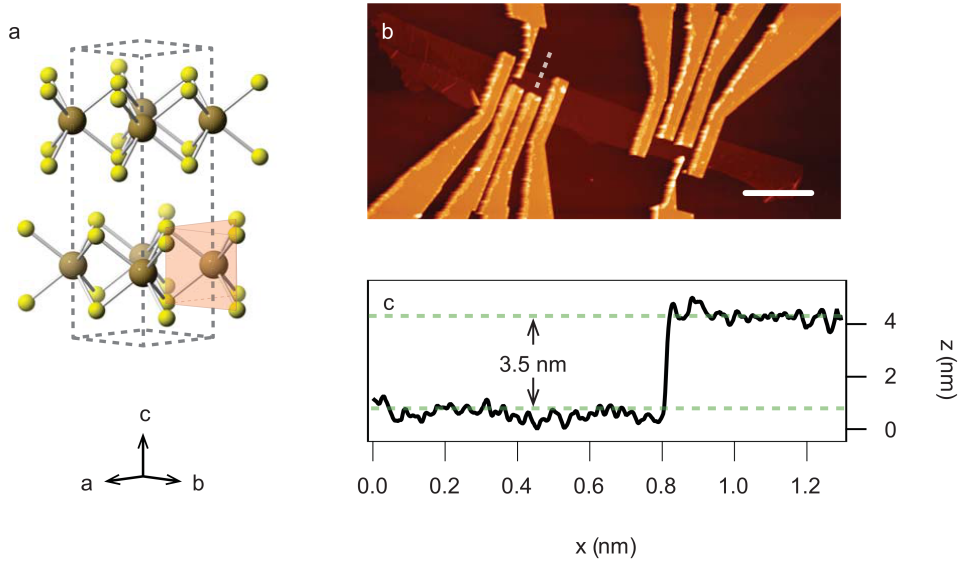


Figure 7.1: **Atomically-thin  $\text{TaS}_2$  devices.** (a) Ball and stick model of the crystal structure of the 2H polytype of  $\text{TaS}_2$ . The dashed prism encloses the content of a single unit cell and the metal coordination geometry is highlighted by the red polyhedron. (b) Atomic force microscopy (AFM) image of two devices fabricated on a 3.5 nm 2H- $\text{TaS}_2$  flake. The scale bar is 4  $\mu\text{m}$  in length. The full color scale of the topograph corresponds to a height of 100 nm. (c) Line profile of the flake taken at the location of the white dotted line in (b).

## 7

cepting substrate and in combination with a shearing cleavage movement. This allows for the cleavage of very thin flakes, down to 1.2 nm thick (see section 7.5.1 in the Appendix), corresponding to a single 2H- $\text{TaS}_2$  unit-cell (see Figure 7.1(a)) formed by two individual layers. Unfortunately, all attempts to contact these flakes and measure transport properties were unsuccessful, likely due to their instability in ambient conditions.

To avoid the oxidation of few layer flakes, freshly exfoliated samples designated for device fabrication and transport measurements are immediately covered with an MMA/PMMA double layer resist in preparation for subsequent device nanofabrication steps. Before exfoliation, contact pads and optical markers are created on the surface of the Si/SiO<sub>2</sub> substrates to locate and design contacts to the transferred flakes. After exfoliation, the contacts (chromium-5 nm/ gold-70 nm) are patterned with standard e-beam lithography (Vistec, EBPG5000PLUS HR 100), metal deposition (AJA International), and subsequent lift-off in warm acetone. In order to preserve the sample integrity, it is crucial to exfoliate, pattern the electrodes, and load into the dilution fridge within a few hours. In that respect and even after minimizing the fabrication time, all attempts to contact flakes with thicknesses below 3.5 nm were unsuccessful due to sample degradation. Figure 7.1(b) shows an example of a fabricated device incorporating the thinnest flake measured with a thickness of 3.5 nm (corresponding to about 5 layers) and lateral dimensions of the order of a few microns as imaged by AFM. All transport measurements are made using a four terminal current bias configuration in a temperature range of 20 mK to 4 K in a dilution fridge.

### 7.3. LOW TEMPERATURE CHARACTERIZATION OF $T_c$ AND $B_{c2}$

In total, we present measurements on twelve flakes of varying thicknesses in the  $\approx 3$ -30 nm range, integrated in the described four-terminal devices, with the aim of studying the effect of dimensionality reduction on the superconducting properties of TaS<sub>2</sub>. All devices show a superconducting transition observed by four terminal current bias measurements as a function of temperature. Figure 7.2 shows the current-voltage ( $I - V$ ) and resistance-temperature ( $R - T$ ) characteristics for three representative devices having thicknesses of 14.9 nm (Figure 7.2(a) - (b)), 5.8 nm (Figure 7.2(c) - (d)), and 4.2 nm (Figure 7.2(e) - (f)). The transport data for the thinnest 3.5 nm flake can be found in the Appendix, section 7.5.3. The zero bias, numerical derivatives ( $dV/dI$ ) as a function of temperature show a clear superconducting transition for each device (Figures 7.2(b), (d), and (f)). From these (interpolated) curves we estimate  $T_c$ , taken at 50% of the normal-state resistance. For the 14.9 nm flake, and despite the fact that the sample does not attain a zero resistive state, one may still appreciate that there is a phase transition centered at  $540 \pm 230$  mK. This is in rough agreement with previously reported  $T_c$  values of 600 mK for bulk 2H-TaS<sub>2</sub> material[47]. Interestingly, and in contrast with studies on other 2D superconductors, the  $T_c$  values show a marked increase for the thinner flakes of 5.8 nm ( $1.45 \pm 0.13$  K) and 4.2 nm ( $1.79 \pm 0.20$  K). This peculiar result is discussed in detail below. Additionally, critical current densities increase by orders of magnitude as the devices become thinner (14.9 nm,  $J_c \approx 700$  Acm<sup>-2</sup>, 5.8 nm,  $J_c \approx 7 \times 10^4$  Acm<sup>-2</sup>, and 4.2 nm,  $J_c \approx 5 \times 10^5$  Acm<sup>-2</sup>). In thin film superconductors with high critical current densities, as those measured in our thinnest flakes, Joule self-heating starts to play a role[48]. This explains the pronounced asymmetry in the I-V characteristics for thinner flakes (Figure 7.2(a) versus Figure 7.2(e)). As the current bias is swept from high negative values through zero, non-equilibrium Joule heating pushes the superconducting transition to a lower current value. This asymmetry decreases as the temperature approaches  $T_c$  where Joule heating effects become less significant (Figure 7.2(e)).

To further characterize the devices at 50 mK, the upper critical field ( $B_{c2}$ ) of these type II superconductors is determined by applying an external magnetic field, perpendicular to the surface of the flake. Figure 7.3 shows color scale plots of  $dI/dV - I$  curves as a function of external field for the same three devices as in Figure 7.2. Figure 7.3(b) shows the zero-bias differential resistance as a function of external field. From these curves we estimate the  $B_{c2}$  as the external field at which the device returns to the normal-state resistance. Once again in accordance with the upper critical field reported for the bulk material (110 mT), we measure a  $B_{c2}$  of  $\approx 130$  mT for the bulk-like 14.9 nm flake[49]. The thinner flakes present higher upper critical fields of  $\approx 0.9$  T (5.8 nm) and  $\approx 1.7$  T (4.2 nm) following the interesting trend for  $T_c$ . The critical fields at 50 mK allow estimation of the superconducting Ginzburg-Landau (GL) coherence lengths given by:  $B_{c2}(50mK) = \phi_0/2\pi\xi(50mK)^2$ . The coherence lengths for the 4.2 nm and 5.8 nm flakes are 13.9 nm and 19.1 nm, respectively, suggesting that these flakes are well in the 2D limit. To further qualify the 2D nature of the thinnest flakes, we analyze the  $I - V$  and  $R - T$  curves (such as those in Figure 7.2) of selected devices at zero external field in order to infer the typical signature of 2D superconductivity: the Berezinskii-Kosterlitz-Thouless (BKT) transition (see section in the Appendix). Note that this study can only be carried out for selected thinner samples for which sufficient data is available. We find that the transport data is

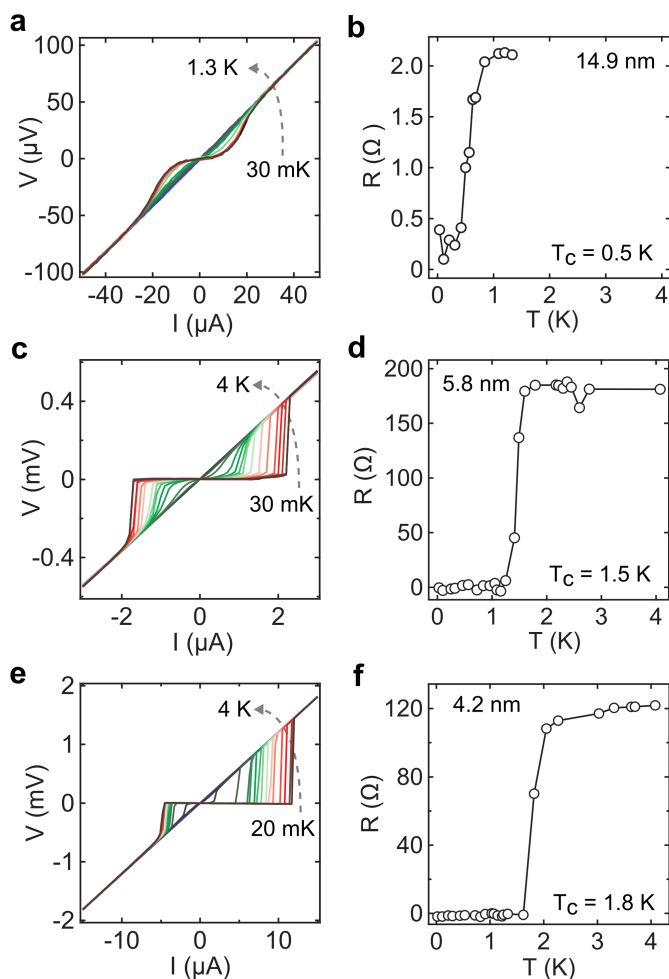


Figure 7.2: **Superconductivity in atomically thin crystals.** Temperature dependence of three selected devices spanning the range of thicknesses studied. (a) Current-voltage (I-V) characteristics as a function of temperature for a bulk-like 14.9 nm device. (b) Resistance (zero bias numerical derivative) vs. temperature for the 14.9 nm device. (c) I-V characteristics as a function of temperature for a 5.8 nm device. (d) Resistance vs. temperature for the 5.8 nm device. (e) I-V characteristics as a function of temperature for a 4.2 nm device. (f) Resistance vs. temperature for the 4.2 nm device.



consistent with a BKT superconducting transition, further supporting the 2D nature of the thinnest TaS<sub>2</sub> flakes.

## 7.4. THICKNESS DEPENDENCE

We now turn our attention to the collective behavior of our twelve devices and the effect of reduced dimensionality on the superconducting properties of TaS<sub>2</sub>. Figure 7.4 illustrates the measured  $T_c$  and  $B_{c2}$  for the devices reported. A bulk limit is found for samples over 10 nm in thickness, such as the one in figures 2(a - b) and 3(a - b), for which the superconducting properties were consistent with bulk crystals and did not depend on the number of layers. It is interesting to note that these types of flakes exhibit a non-zero residual resistance (red data points in Figure 7.4) at base temperature, indicating a certain degree of crystalline inhomogeneity and providing a plausible explanation to the slight variation of  $T_c$ , similar to the variation in reported bulk values (0.6 K and 0.8 K)[47, 50]. The bulk-limit devices approach the edge of the 2D limit set by the GL coherence length ( $\xi = 55$  nm) estimated from the bulk  $B_{c2}$  (see Figure 7.4(b)).

In addition to thicker flakes that behave in a way consistent with bulk properties, we also observe the superconducting transition in devices made out of thinner TaS<sub>2</sub> flakes, down to 3.5 nm (about 5 layers). Interestingly, we observe a strong enhancement of  $T_c$  and  $B_{c2}$  for thinner flakes, up to more than a factor of four larger than in the bulk material. The  $T_c$  enhancement with decreasing number of layers exhibited by the TaS<sub>2</sub> samples is in strict contrast to the  $T_c$  suppression previously reported in elemental materials[8], binary systems[51], and even the closely related dichalcogenide family member, NbSe<sub>2</sub>[27, 28]. A common theme in these studies is that as the material is thinned down, substrate interactions, either from induced strain or increased Coulomb interactions, suppress the formation of Cooper pairs. In NbSe<sub>2</sub> devices, a clear correspondence can be made with a decrease in the residual resistance ratio (RRR) giving an indication of increased substrate interactions or more probable that flake degradation is more prevalent in thinner flakes[28]. This agrees with our attempts to contact flakes thinner than 3.5 nm showing a complete insulating state at room temperature. Correspondingly, the RRR values (see section 7.5.5 in the Appendix) for our TaS<sub>2</sub> sample set show a significant reduction for the two thinnest flakes. However, devices as thin as 4.5 nm still maintain an RRR of 10 indicating pristine thin samples even below the bulk limit set at 10 nm.

An initial consideration in interpreting the  $T_c$  enhancement is the possibility of electrochemical doping coming from either the original crystals, or through fabrication processes (lithography resists). Although it is well understood that the  $T_c$  of TaS<sub>2</sub> crystals is particularly sensitive to intrinsic non-stoichiometric doping[52], we may rule out this effect coming from the original crystals by having measured a bulk  $T_c$  of approximately 0.5 K. Now considering the potential doping coming from environmental or intercalation interactions, Raman spectroscopy provides us with strong evidence of the absence of such processes. In contrast with the remarkable peak shifts displayed by intercalated crystals of 2H-MX<sub>2</sub>, the Raman spectra of exfoliated flakes presented in the supplement (see section 7.5.2 in the Appendix) show no significant change in crystal structure for flakes of only 4 layers. Given that the flakes are not undergoing intercalation through exfoliation or fabrication, there could indeed be some doping coming from surface contami-

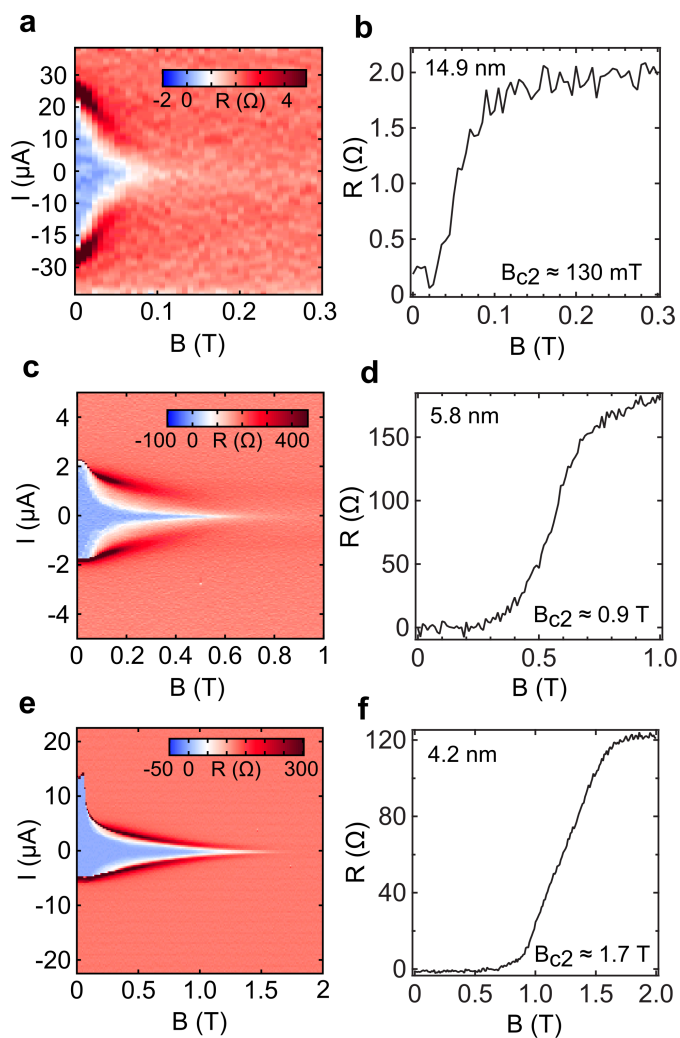


Figure 7.3: **Enhanced critical magnetic field in thin flakes.** Perpendicular external magnetic field dependence for three selected devices spanning the range of thicknesses studied. (a) Resistance (zero bias numerical derivative) vs. applied field for a bulk-like, 14.9 nm device. (b) Zero bias resistance vs. applied field for the 14.9 nm device. (c) Resistance (zero bias numerical derivative) vs. applied field for the 5.8 nm device. (d) Zero bias resistance vs. applied field for the 5.8 nm device. (e) Resistance vs. applied field for the 4.2 nm device. (f) Zero bias resistance vs. applied field for the 4.2 nm device.

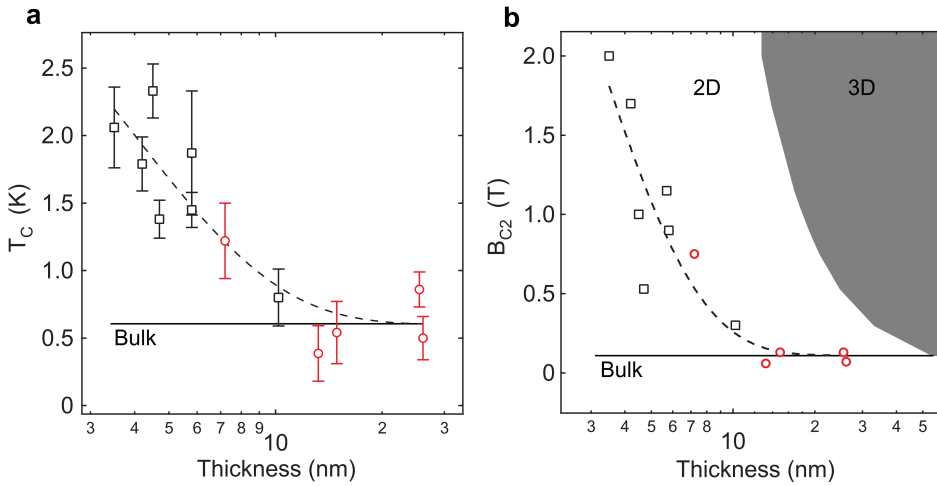


Figure 7.4: **2D superconductivity and enhanced  $T_c$  and  $B_{c2}$  in atomically thin TaS<sub>2</sub>.** (a) Variation of  $T_c$  as a function of the thickness of the TaS<sub>2</sub> flakes. Devices exhibiting a non-zero residual resistance below  $T_c$  are plotted in red. The error bars are given by the temperatures at 10% and 90% of the normal state resistance. The solid black line marks the bulk  $T_c$  of 600 mK. The black dotted line is an exponential trend line, fit to the data starting at the bulk limit. (b) Variation of  $B_{c2}$  as a function of flake thickness. The red circles mark the same devices in (a) having residual resistance. The black solid line indicates the bulk limit upper critical field of 110 mT. The grey solid line plots the GL coherence lengths, calculated from the y-axis  $B_{c2}$  values, and marks the edge of the 2D limit.

nation or from the oxide substrate. However, previous studies show that gate-induced or surface-induced electrostatic doping allows for a carrier density modulation of maximum  $\approx 10^{12} \text{ cm}^{-2}$  [53], which is at least three orders of magnitude lower than the estimated single layer carrier concentration in these metallic TMDCs ( $\approx 10^{15} \text{ cm}^{-2}$ ) [30, 54]. In this line, these doping effects have shown to modulate  $T_c$  in  $\text{NbSe}_2$  by 8% at most [28]. Finally, while substrate interactions have led to the interesting  $T_c$  enhancements found in epitaxial grown  $\text{FeSe}$  on strontium titanate (STO), we rule out such effects as the  $\text{TaS}_2$  flakes presented here are weakly coupled to the substrate. This suggests a deeper mechanism as opposed to simple substrate interaction, intercalation, or degradation reported in previous studies.

A possible mechanism at work could be the enhancement in superconducting properties with a suppression of the commensurate charge density wave (CCDW) order, which is in direct competition with superconducting pairing. This is consistent with the interpretation presented of the enhanced  $T_c$  and  $B_{c2}$  observed in the studies on intercalation of TMDCs, where it is argued that the in-plane chemical doping leads to the suppression of the charge density order, and in certain TMDCs under pressure where the same claim is made [55–57]. In order to explore the effect of the CDW on the DOS at the Fermi level as a function of reduced thickness, we calculate the DOS from an effective one-orbital tight-binding model and simulate the CDW at a mean field level as a periodic potential that locally shifts the onsite energy (see section 7.5.6 in the Appendix). We find that the DOS at the Fermi level is not appreciably affected by the CDW for reduced thicknesses. Ultimately, to determine if such a competition with CDWs could be playing a role, one could search for direct evidence of such suppression in STM studies of thin flakes below the 10 nm bulk limit observed here.

An alternative explanation of the enhanced  $T_c$  could be a change of the band structure of the material in atomically thin flakes. To explore this possibility, we perform DFT calculations and construct a simplified tight-binding model to study the electronic band structure and density of states (DOS)  $\nu_N(0)$  as a function of the sample thickness. The results of the calculation can be found in sections 7.5.7–7.5.8 in the Appendix. The resulting two-dimensional bands contain hole pockets and show saddle points below the Fermi level. These saddle points give rise to van Hove peaks whose height increases as the number of layers is decreased, and ultimately diverge in the 2D limit. However, the density of states per layer at the Fermi level  $\nu_N(0)$  decreases as the number of layers is decreased (see Figure 7.13). For a simplified model of constant attractive interaction  $V$ , the coupling constant, that ultimately determines the  $T_c$ , takes the usual BCS value  $\lambda = V\nu_N(0)$ . This behavior of the DOS would suggest at first an analogous trend of  $T_c$ , which does not suffice to explain the experiments. The value of the superconducting gap and  $T_c$  can be influenced by the interaction properties of the material. The effective coupling constant [58] determining  $T_c$  is given by  $\lambda_{eff} = \lambda - \mu^*$ , where  $\lambda$  is the electron-phonon coupling constant, and  $\mu^*$ , known as Anderson-Morel pseudo-potential, is a term that represents the renormalized repulsive Coulomb interaction. In usual 3D superconductors characterized by a featureless, hence constant DOS, the projection of the high energy degrees of freedom gives rise to a pseudo-potential of the form  $\mu^* = \mu / (1 + \mu \ln(W/\omega_0))$ , with  $\omega_0$  the characteristic phonon frequency,  $W$  the system bandwidth, and  $\mu$  the bare Coulomb repulsion. In a 2D system, with a DOS character-

ized by a van Hove singularity near the Fermi level, the renormalization of the bare  $\mu$  can be significantly larger than in a 3D material. This effect is strongly dependent on the number of layers. For a generic DOS  $v_N(\epsilon)$ , the pseudo-potential takes the form

$$\mu^* = \frac{\mu}{1 + \mu \int_{\omega_0}^W d\epsilon \tilde{v}_N(\epsilon) / \epsilon} \quad (7.1)$$

with  $v_N(\epsilon)$  the total DOS normalized with its value at the Fermi energy. Assuming a constant repulsive interaction  $U$ , one can estimate  $\mu = Uv_N(0)$ . For a weak repulsion the renormalization is negligible and the effective coupling constant follows the density of states at the Fermi level  $v_N(0)$ . For a relatively strong Coulomb repulsion, the value of the pseudopotential at the Fermi level can be strongly affected by features of the density of states at higher energies, such as van Hove singularities. As the number of layer is decreased, the renormalization of a relatively strong repulsion for the band structure in the model is sufficient to reverse the dependence of  $T_c$  on the number of layers obtained from a simple electron-phonon attractive interaction (see section 7.5.8 in the Appendix). This analysis points to a non-negligible role of the Coulomb repulsive interaction in superconducting 2H-TaS<sub>2</sub>, characterized by a predominant Ta 5d orbital character at the Fermi level. The Coulomb repulsion has also been proposed to be at the origin of superconductivity in MoS<sub>2</sub>[59–61].

In conclusion, we have reported 2D superconductivity in 2H-TaS<sub>2</sub> in atomically thin layers. In contrast to other van der Waals superconductors such as NbSe<sub>2</sub>, we find that the  $T_c$  of this material is strongly enhanced from the bulk value as the thickness is decreased. In addition to a possible charge-density wave origin, we propose a model in which this enhancement arises from an enhancement of the effective coupling constant, which determines the  $T_c$ . Our results provide evidence of an unusual effect of the reduction of dimensionality on the properties of a superconducting 2D crystal and unveil another angle of the exotic manifestation of superconductivity in atomically thin transition metal dichalcogenides.

## 7.5. APPENDIX

### 7.5.1. OPTICAL CHARACTERIZATION OF 2H-TaS<sub>2</sub> FLAKES

The deposition methodology herein described allows for the use of any type of solid substrate as a receiving surface. However, it has already been established how a facile non-destructive detection of atomically thin TMDC layers may be performed by optical microscopy inspection of samples prepared on Si/SiO<sub>2</sub> wafers[62, 63]. Preliminary examination of TaS<sub>2</sub> patches deposited on a Si wafer with a 285 nm thick SiO<sub>2</sub> capping layer permitted the identification of flakes of different thickness flakes as depicted by their different optical contrast (Figure 7.5).

The presence of this thick silicon dioxide layer between the pure silicon and the deposited material yields an apparent color that depends on the flake thickness due to a light interference effect[64]. This effect results in very faintly colored large surface area patches, which correspond to the thinner crystals. In order to quantitatively study the light interference, we measured the thickness dependent optical contrast between

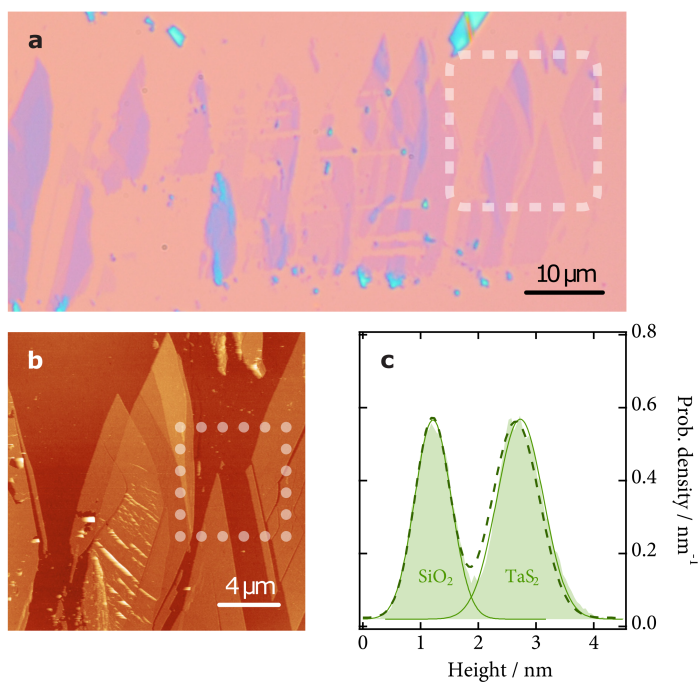


Figure 7.5: Atommally thin  $\text{TaS}_2$  flakes deposited on a Si/285 nm  $\text{SiO}_2$  substrate by the optimized press and shear micromechanical exfoliation method. (a) Optical microscopy image of a region of the substrate displaying a high density of atomically thin flakes. (b) AFM image of the region highlighted in a by the dashed box. (c) Probability density distribution of heights inside the dotted box in (b). In this particular image a flake thickness of  $1.2 \pm 0.5$  nm may be estimated.

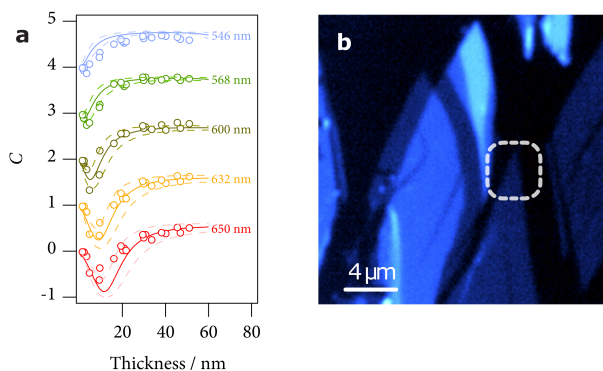


Figure 7.6: Optical contrast study of 2H-TaS<sub>2</sub> flakes. (a) Optical contrast ( $C$ ) of a selection of flakes as a function of flake thickness under five different monochromatic illumination wavelengths ( $\lambda$ ) between 546 nm and 650 nm. The solid lines correspond to the Fresnel-law-model calculation using the refractive index reported in the literature[69]. Note that the sets of contrast measurements for different  $\lambda$  have been shifted vertically by 1, 2, 3, and 4 units for clarity. The uncertainty in  $C$  due to a  $\pm 10\%$  variation in the real and imaginary parts of the refractive index is indicated by the dashed lines. (b) Optical contrast image at  $\lambda = 600$  nm. The flake region marked by the dashed box is 1.2 nm thick, measured by AFM in contact mode, and shows a negative optical contrast of  $-0.03$ .

the flake and the SiO<sub>2</sub> substrate under different illumination wavelengths (see Figure 7.6)[65–68]. For accurate determination of the thickness of the deposited TaS<sub>2</sub> flakes, an AFM operated in contact mode was employed. The optical contrast depends both on the flake thickness and the illumination wavelength (shown in Figure 7.6), and can be calculated using a model based on Fresnel laws using the refractive index of TaS<sub>2</sub> reported in the literature[69]. We found a significant agreement between the measured optical contrast for thin flakes and that obtained from the model using the refractive index of bulk TaS<sub>2</sub>. It is remarkable that the optical contrast is strongly dependent on the illumination wavelength and even changes its sign for flakes thinner than 20 nm. This behavior makes white light illumination inappropriate for the identification of the thinnest flakes by optical microscopy. Oppositely, illumination under certain wavelengths enhances the optical contrast of the thinnest TaS<sub>2</sub> crystals, which allowed the optical identification of layers as thin as 1.2 nm.

### 7.5.2. RAMAN SPECTROSCOPY OF 2H-TAS<sub>2</sub>

The potential relationship between the flake thickness and the Raman scattering intensity was explored. For this reason a  $\mu$ -Raman probe was used to explore different thickness flakes. Figures 7.7 and 7.8 shows the thickness dependence of a selection of Raman features. Whereas the frequency shift and the full-width-at-half-maximum (FWHM) of the A1g and E2g Raman modes do not seem to be at all related to the number of layers, it may be clearly appreciated how the ratio between the intensity of the Si peak (at 521 cm<sup>-1</sup>) and the A1g and E2g peaks both increase upon decreasing the number of layers of the probed flake. The frequency difference between the A1g and E2g Raman modes

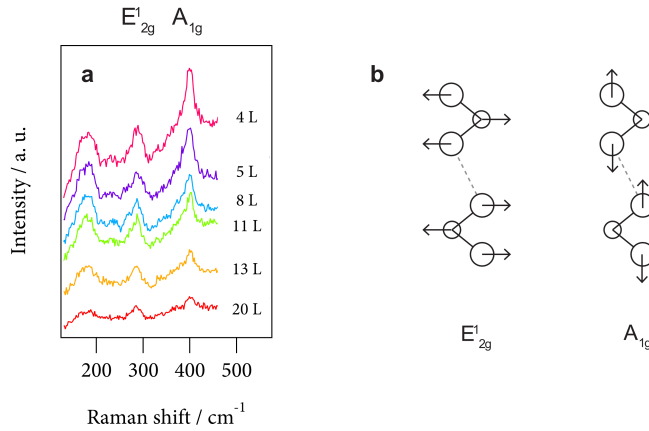


Figure 7.7: Raman spectroscopy of 2H-TaS<sub>2</sub> flakes. (a) Raman spectra measured for 2H-TaS<sub>2</sub> flakes with thickness ranging from four layers to 20 layers. (b) Schematic representation of the vibration modes that correspond to the most prominent peaks at (a).

also exhibit a linear proportionality with the number of layers present in the flakes. It is important to highlight that as for other TMDCs, some sensitivity to the Raman laser beam was also exhibited by the TaS<sub>2</sub> flakes. In this way, upon performing experiments with long exposure times or high irradiation powers, the flakes were irreversibly damaged as seen by a change in the optical contrast in the focus spot of the laser beam. Yet, no apparent change in the height profile as measured by AFM could be detected. By contrast, the appearance of a strong photoluminescence emission band around 555 nm suggested that some oxidation to Ta<sub>2</sub>O<sub>5</sub> had occurred[70].

On a final note, it has been previously observed in other transition metal dichalcogenides how the intensity of the distinct Raman modes may vary as the angle between the linearly polarized incident beam and the scattered signal is modified[71]. This can be used to confirm the origin of the Raman peaks. In the TaS<sub>2</sub> case, it could be observed that while the intensity of the E<sub>2g</sub> mode does not depend on the angle between the excitation and detection, the A<sub>1g</sub> mode presents its maximum intensity for parallel excitation and detection and it vanishes for cross polarized excitation and detection in agreement with that reported for other TMDC flakes[72, 73], confirming that the Raman signal comes from an analogous crystal (see Figure 7.9).

### 7.5.3. THINNEST DEVICE MEASURED

Figure 7.10 shows the low temperature characteristics for the thinnest device investigated with a thickness of 3.5 nm (see Figure 7.1 for the AFM scans). From the transport measurements, following the analysis in the chapter, we estimate a critical temperature of  $\approx 2.1$  K (Figure 7.10(b)) and a critical field of 2 T (Figure 7.10(d)). An intermediate transition can be seen in the  $I - V$  curves in Figure 7.10(a) which is most likely due to



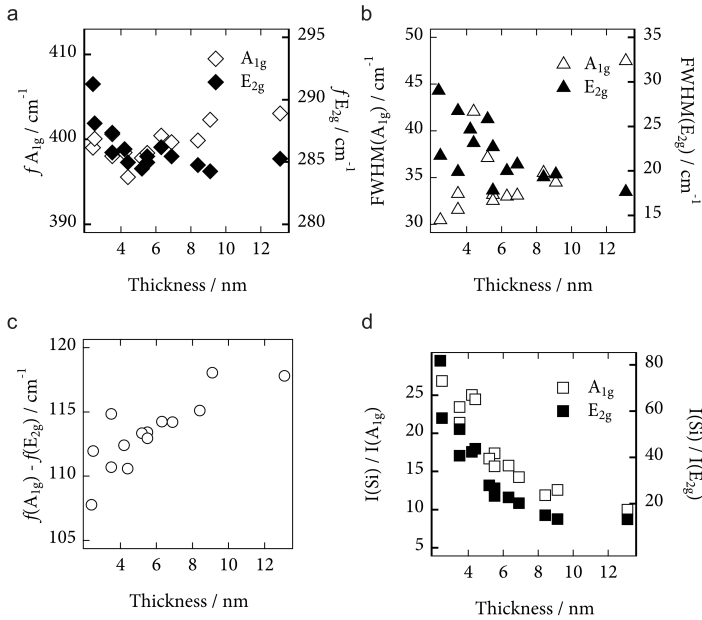


Figure 7.8: Thickness dependence of different Raman features of a selection of 2H-TaS<sub>2</sub> flakes. (a) Frequency shift; (b) FWHM of the A<sub>1g</sub> and E<sub>2g</sub> Raman modes; (c) frequency difference between the A<sub>1g</sub> and E<sub>2g</sub> Raman modes; and (d) Raman intensity ratio between the Si peak (at 521 cm<sup>-1</sup>) and the A<sub>1g</sub> and E<sub>2g</sub> peaks.

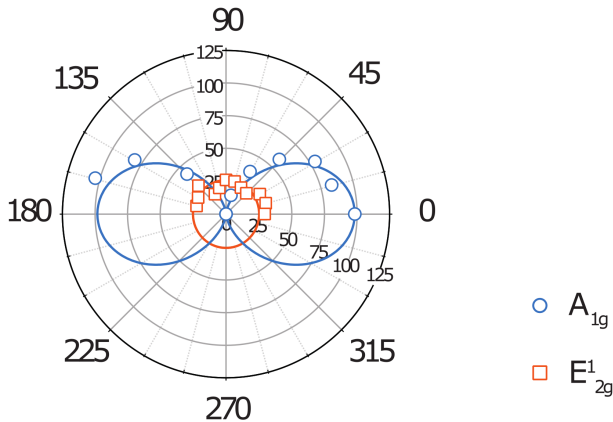


Figure 7.9: Angular dependence of the 2H-TaS<sub>2</sub> signal. (a) Frequency shift; (b) FWHM of the A<sub>1g</sub> and E<sub>2g</sub> Raman modes; (c) frequency difference between the A<sub>1g</sub> and E<sub>2g</sub> Raman modes; and (d) Raman intensity ratio between the Si peak (at 521 cm<sup>-1</sup>) and the A<sub>1g</sub> and E<sub>2g</sub> peaks.

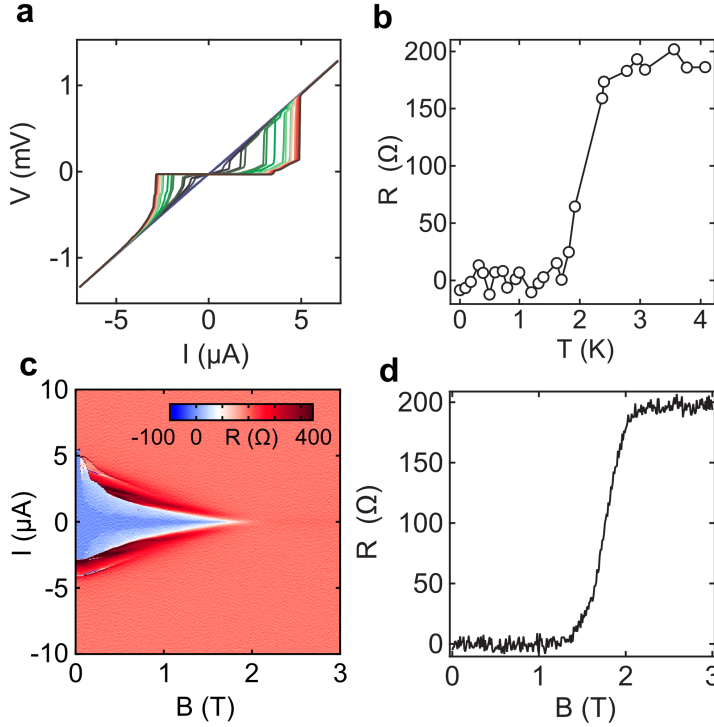


Figure 7.10: Transport properties of a device made out of a 3.5 nm thick  $\text{TaS}_2$  flake. (a) Current-voltage ( $I$ - $V$ ) characteristics as a function of temperature (b) Resistance (zero bias numerical derivative) vs. temperature curve. (c) Resistance vs. applied field and bias current. (d) Zero bias resistance vs. applied field.

two regions or weakly coupled layers turning normal at different current densities.

#### 7.5.4. BEREZINSKII–KOSTERLITZ–THOULESS (BKT) FITS TO SELECTED DEVICES

$I$ - $V$  curves were fit to a power law of the form  $V \propto I^\alpha$ , where  $\alpha$  spans from 1 for temperatures above  $T_{BKT}$ , reaching a value of  $\alpha = 3$  at the BKT transition, and monotonically increasing as temperature is further lowered. The  $R$ - $T$  curves are further fit to the resistance dependence near the BKT temperature,  $R = R_N \exp(-b/(T - T_{BKT})^{1/2})$ . Figure 7.11 shows a set of  $I$ - $V$  and  $R$ - $T$  curves taken for two devices with thicknesses of 4.7 nm (a - c) and 5.8 nm (d - f). It may be appreciated how the data do follow a power law with values of the  $\alpha$  parameter that vary in the expected range typical for 2D superconductivity. From the  $\alpha$ -exponent analysis and  $R$ - $T$  transition we estimate a BKT temperature of 1 K for the 4.7 nm flake and 1.2 K for the 5.8 nm flake.

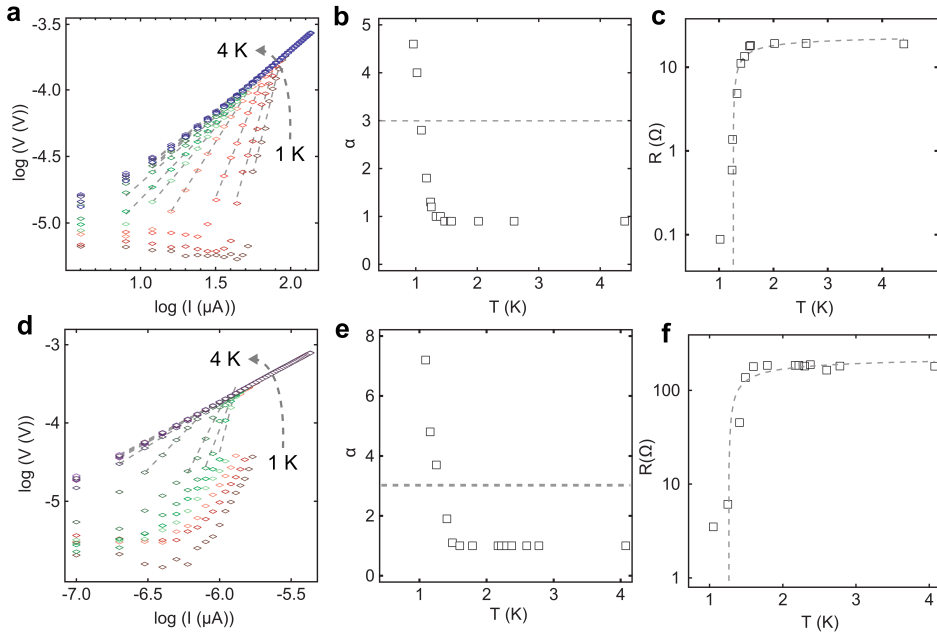


Figure 7.11: Example of a BKT fit performed for a 4.7 nm (a - c) and 5.8 nm (d - e) thick sample. (a, d) I-V curves are displayed in a log-log scale. (b, e) The variation of the  $\alpha$  parameter as a function of temperature, where the  $\alpha = 3$  value is indicated by the black dashed line and corresponds to  $T_{BKT}$ . (c, f) R-T curves as a function of temperature. The black dotted line plots the  $R(T)$  dependence of the BKT model (see text).

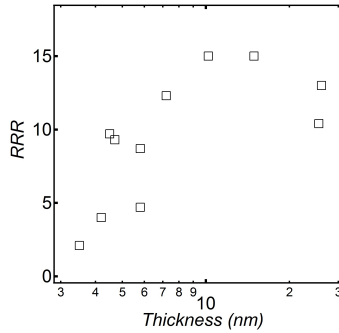


Figure 7.12: Resistance Residual Ratio (RRR) as a function of flake thickness.

### 7.5.5. RESIDUAL RESISTANCE RATIO VS. THICKNESS

Figure 7.12 shows the residual resistance ratio for all the devices measured. The RRR is calculated as the ratio between the room temperature (297 K) resistance and the low temperature resistance at 4 K ( $\text{RRR} = R(297\text{K})/R(4\text{K})$ ). High RRR values (10) are still maintained below the bulk limit thickness of 10 nm indicating pristine flakes and absence of strong substrate interaction or disorder. This is in contrast with similar studies on  $\text{NbSe}_2$  where the RRR is seen to monotonically decrease with flake thickness[28].

### 7.5.6. CHARGE DENSITY WAVE (CDW) CONSIDERATIONS IN 2H- $\text{TaS}_2$

The experimentally observed charge density wave in 2H- $\text{TaS}_2$  has a periodicity of  $3 \times 3$  unit cell in the layer plane. We consider an effective one-orbital tight-binding model and simulate the CDW at mean field level as an onsite potential that locally shift the onsite energy. The effect of the CDW is seen in the DOS at an energy of 0.2 - 0.3 (in units of the tight binding hopping parameters), in the form of small corrugation arising from the gap opening in part of the band structure (Figure 7.13(a)). At the Fermi energy, no gap is opened (again visible in Figure 7.13(a)) and the behavior of the DOS at the Fermi level (Figure 7.13(b)), which is ultimately responsible of the  $T_c$ , is not affected by the presence of the CDW.

### 7.5.7. DFT BAND STRUCTURE AND TIGHT-BINDING MODEL

A crucial starting point for studying the behavior of the critical temperature versus the thickness of the sample is a faithful description of the system in terms of a band structure and wavefunctions. The DFT simulation of the band structure of 2H- $\text{TaS}_2$  is performed using the Siesta code on systems with different number of layers[74]. We use the generalized gradient approximation (GGA), in particular, the functional of Perdew, Burke and Ernzerhoff[75]. In addition, we use a split-valence double- $\zeta$  basis set including polarization functions[76]. The energy cut-off of the real space integration mesh was set to 300 Ry and the Brillouin zone k sampling was set, within the Monkhorst-Pack scheme[77], to  $30 \times 30 \times 1$  in the case of multilayer samples and  $30 \times 30 \times 30$  in the case of the bulk calculation. We use the experimental crystal structure of 2H- $\text{TaS}_2$  for all the calculations[78].

The resulting band structure of our calculations is shown in Figure 7.14. The bands

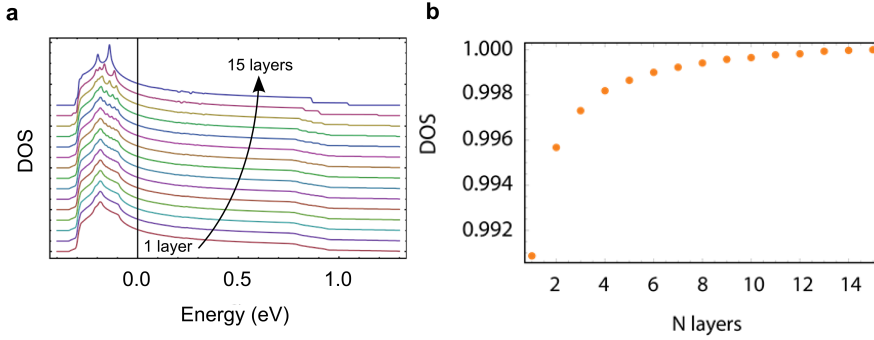


Figure 7.13: (a) Density of states for  $N=1, \dots, 15$  layer 2H-TaS<sub>2</sub> systems in presence of a CDW potential. (b) Density of states (DOS) at the Fermi level versus  $N$  layers of 2H-TaS<sub>2</sub> in presence of the CDW modulation.

crossing at the Fermi level have a strong Ta  $d$  character. The Fermi surface for a system composed by  $N$  layers is constituted by  $N$  pockets around  $\Gamma$ ,  $N$  pockets in  $K$ , and  $N$  pockets in  $K'$ , and in the limit of large  $N$  gives rise to the well known tubular Fermi surfaces.

The calculated total density of states (tot-DOS) is shown in Figure 7.15, where we can see that it presents a large peak slightly below the Fermi level, with a height that increases linearly with increasing number of layers, and whose position does not change when varying the number of layers. The tot-DOS at the Fermi level also presents a linear increase with increasing number of layers. From the band structure we understand the peak as arising from van Hove singularities associated to saddle points in the band structure at the  $M$  point and at an intermediate point between the  $K$  point and  $\Gamma$  point. A van Hove peak is a logarithmic singularity that shows up in the DOS when the system is 2D. As we increase the number of layers the van Hove singularities get smooth and average out when the systems becomes 3D.

The meshing in the DFT simulations, although sufficiently dense for the convergence of the total energy, is not sufficient to resolve the van Hove peak in the DOS. We then construct an effective tight-binding model of a single orbital in a triangular lattice considering in-plane and out-of-plane hopping up to second nearest neighbors,

$$H_0 = - \sum_{n,m=1}^N \sum_{i,j} c_{i,n} * t_j^m c_{i+j,n+m} + H.c. \quad (7.2)$$

and by fitting the DFT band structure we find  $t_1^0 = -0.033$ ,  $t_2^0 = -0.227$ ,  $t_0^1 = -0.039$ ,  $t_1^1 = -0.016$ ,  $t_2^1 = -0.010$ , where  $t_j^n$  is the hopping matrix element between the  $n$ -th out-of-plane and the  $j$ -th in-plane nearest neighbor sites. The 2nd in-plane nearest neighbor hopping  $t_2^0$  comes out to be larger than the 1st nearest neighbor one, a result that has been already discussed in the literature[40], and is due to a phase cancellation mechanism, typical of 2H-TMDCs. The resulting DOS per layer at the Fermi level  $\nu_N(0)$  is shown in Figure 7.16, where we clearly see a monotonic decrease of the DOS as we lower the number of layers.

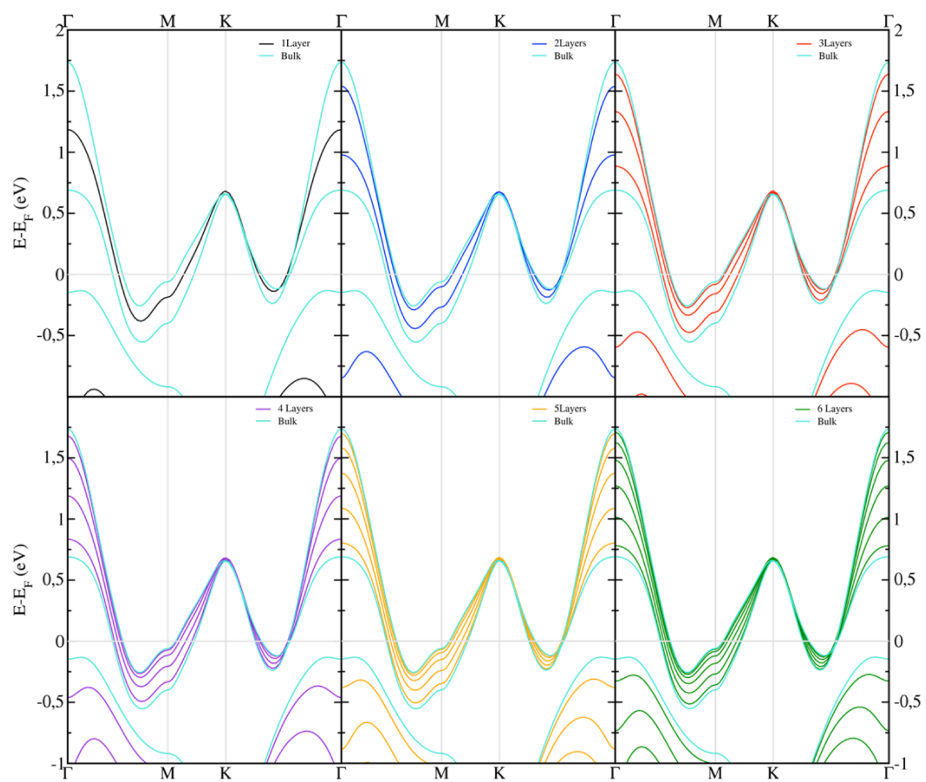


Figure 7.14: DFT band structure of the different systems with varying number of 2H-TaS<sub>2</sub> layers from 1 to 6. The bulk band structure (light blue) is plotted in all charts as a reference.

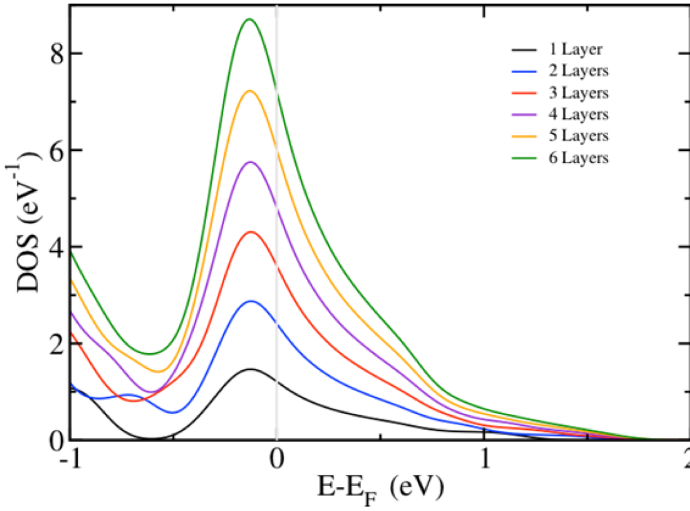


Figure 7.15: Non-normalized DFT calculated density of states (tot-DOS) with varying number of 2H-TaS<sub>2</sub> layers.

### 7.5.8. ANDERSON-MOREL MODEL

The Anderson-Morel model takes into account the effect of a repulsive Coulomb interaction that reduces the effective coupling constant determining the superconducting  $T_c$ . Here, we generalize the Anderson-Morel model to a system with a generic DOS, that allows us to properly account for the van Hove logarithmic singularities appearing as the systems becomes more and more 2D, as is the case when lowering the thickness of the sample. The idea is to correctly project to the low energy sector the contribution of the high energy repulsive tail of the effective electron-electron interaction. The starting point is a generalized gap equation in the framework of the Eliashberg theory that couples the gap at all energies,

$$\Delta(\epsilon) = - \int d\epsilon' V_{eff}(\epsilon, \epsilon') v_N(\epsilon') \frac{\tanh\left(\frac{\epsilon'}{2T}\right)}{2\epsilon'} \Delta(\epsilon') \quad (7.3)$$

where the effective interaction  $V_{eff}(\epsilon, \epsilon')$  is the result of electron-phonon and the electron-electron terms. To keep the problem as simple as possible, we follow the usual treatments and discretize the effective interaction as  $v_N(0)V_{eff}(\epsilon, \epsilon') = -\lambda + \mu$ , for  $-\omega_0 \leq \epsilon, \epsilon' \leq \omega_0$ , and  $v_N(0)V_{eff}(\epsilon, \epsilon') = \mu$ , for  $-W_0 \leq \epsilon, \epsilon' \leq W$ , with  $W$  the bandwidth of the DOS. This way, the bandwidth interval is characterized by two regions with different interactions, attractive at a low energy and repulsive at high energy. The gap function can then be separated in two values in the different two regions,  $\Delta(\epsilon) = \Delta$  for  $|\epsilon| < \omega_0$ , and  $\Delta(\epsilon) = \Delta\xi$ , for  $\omega_0 < |\epsilon| < W$ . By introducing the bulk quantities  $\lambda_B = Vv_{bulk}(0)$ ,  $\mu_B = Uv_{bulk}(0)$ , the gap equation simplifies to the following system of two coupled equations

for  $\Delta$  and  $\xi$ ,

$$1 = (\lambda_B - \mu_B)I_1 - \mu_B \xi I_2 \xi = -\mu_B I_1 - \mu_B \xi I_2 \quad (7.4)$$

where we have defined the following integrals,

$$I_1 = \int_0^{\omega_0} d\epsilon \frac{\tanh(\epsilon/2T)}{\epsilon} \tilde{v}_N(\epsilon), I_2 = \int_{\omega_0}^W d\epsilon \frac{\tanh(\epsilon/2T)}{\epsilon} \tilde{v}_N(\epsilon) \quad (7.5)$$

with  $\tilde{v}_N(\epsilon) = (v_N(\epsilon) + v_N(-\epsilon))/2v_{bulk}(0)$ . As we have seen by the DFT simulations and the tight-binding model, the total DOS normalized by the number of layer is featureless close to the Fermi level, so that the integral  $I_1$  is performed in the usual way and it gives  $I_1 = \ln(1.14\omega_0/T)$ . At the same time, the DOS displays van Hove singularities at higher energies, that become more and more pronounced as we lower the number of layers. In the limit  $T/W_0 \ll 1$ , the integral  $I_2$  can be approximated as

$$I_2 = \int_{\omega_0}^W d\epsilon \frac{\tilde{v}_N(\epsilon)}{\epsilon} \quad (7.6)$$

Using the approximate DOS resulting from the tight-binding model, we checked that the value of  $I_2$  monotonically increases with lowering the number of layers, even if the van Hove peaks are smoothed in the numeric approximations. The effective coupling constant  $\lambda_{eff} = \lambda - \mu^*$  is then written as,

$$\lambda_{eff} = v_N(0) \left( \lambda_B - \frac{\mu_B}{1 + \mu_B I_2} \right) \quad (7.7)$$

where the dependence on the number of layers  $N$  is hidden in  $v_N(0)$  and  $I_2$ . As we pointed out in the main chapter, the renormalization of the pseudo-potential is particularly relevant if the bare Coulomb term is sufficiently strong. In Figure 7.16 we plot the effective coupling constant  $\lambda_{eff}$  for three different values of the bare pseudo-potential,  $\mu_B = 0.1, 0.5, 1.5$ . Since we are interested in the trend of  $\lambda_{eff}$  with lowering  $N$ , we choose  $\lambda_B$  greater than the bulk value of  $1/I_2$ , so to guarantee a positive coupling constant. In the computation of  $I_2$  we choose the phonon frequency  $\omega_0 = 50$  meV and for  $\lambda_B = 0.36$ . For weak value of  $\mu_B$ , the effective coupling constant follows the DOS at the Fermi energy, whereas for stronger repulsion we can clearly see that  $\lambda_{eff}$  increases.



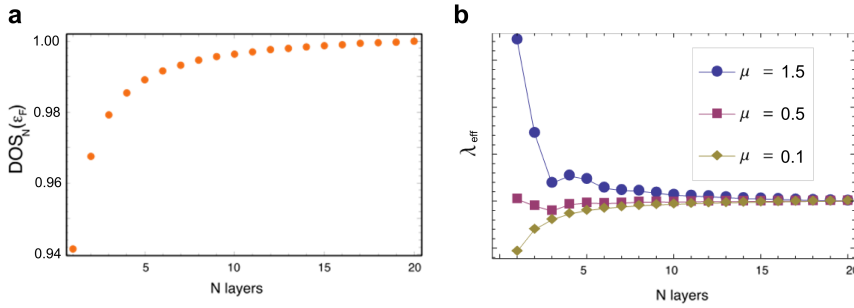


Figure 7.16: (a) Relative change of the DOS per layer at the Fermi level  $v_N(0)$  with varying number of TaS<sub>2</sub> layers. The DOS is obtained from the tight-binding model, and the DOS of the  $N^{\text{th}}$  layer is normalized to the one with 20 layers. (b) Effective coupling constant  $\lambda_{\text{eff}} = \lambda - \mu^*$  as a function of the number of layers  $N$ , for different values of the bare Coulomb pseudo-potential. In the graph, three values of the bare pseudo-potential are explored ( $\mu_B = 0.1, 0.5, 1.5$ ) and  $\lambda_B = 0.36$ .  $\lambda_{\text{eff}}$  is normalized to its bulk value for a given set of  $\lambda_B$  and  $\mu_B$ .

## REFERENCES

- [1] E. Navarro-Moratalla, J. O. Island, S. Mañas-Valero, E. Pinilla-Cienfuegos, A. Castellanos-Gomez, J. Quereda, G. Rubio-Bollinger, L. Chirolli, J. A. Silva-Guillén, N. Agrait, *et al.*, *Enhanced superconductivity in atomically thin TaS<sub>2</sub>*, *Nature Communications* **7**, 11043 (2016).
- [2] M. R. Beasley, J. E. Mooij, and T. P. Orlando, *Possibility of vortex-antivortex pair dissociation in two-dimensional superconductors*, *Physical Review Letters* **42**, 1165 (1979).
- [3] D. B. Haviland, Y. Liu, and A. M. Goldman, *Onset of superconductivity in the two-dimensional limit*, *Physical Review Letters* **62**, 2180 (1989).
- [4] A. Yazdani and A. Kapitulnik, *Superconducting-insulating transition in two-dimensional a-MoGe thin films*, *Physical Review Letters* **74**, 3037 (1995).
- [5] A. M. Goldman, *Superconductor-insulator transitions in the two-dimensional limit*, *Physica E: Low-dimensional Systems and Nanostructures* **18**, 1 (2003).
- [6] Y. Guo, Y.-F. Zhang, X.-Y. Bao, T.-Z. Han, Z. Tang, L.-X. Zhang, W.-G. Zhu, E. Wang, Q. Niu, Z. Qiu, *et al.*, *Superconductivity modulated by quantum size effects*, *Science* **306**, 1915 (2004).
- [7] M. Hermele, G. Refael, M. P. A. Fisher, and P. M. Goldbart, *Fate of the josephson effect in thin-film superconductors*, *Nature Physics* **1**, 117 (2005).
- [8] S. Qin, J. Kim, Q. Niu, and C.-K. Shih, *Superconductivity at the two-dimensional limit*, *Science* **324**, 1314 (2009).
- [9] T. Zhang, P. Cheng, W.-J. Li, Y.-J. Sun, G. Wang, X.-G. Zhu, K. He, L. Wang, X. Ma, X. Chen, *et al.*, *Superconductivity in one-atomic-layer metal films grown on Si(111)*, *Nature Physics* **6**, 104 (2010).
- [10] K. S. Novoselov, D. Jiang, F. Schedin, T. J. Booth, V. V. Khotkevich, S. V. Morozov, and A. K. Geim, *Two-dimensional atomic crystals*, *Proceedings of the National Academy of Sciences* **102**, 10451 (2005).
- [11] C. R. Dean, A. F. Young, I. Meric, C. Lee, L. Wang, S. Sorgenfrei, K. Watanabe, T. Taniguchi, P. Kim, K. Shepard, *et al.*, *Boron nitride substrates for high-quality graphene electronics*, *Nature Nanotechnology* **5**, 722 (2010).
- [12] S. Zhou, G.-H. Gweon, A. V. Fedorov, P. N. First, W. A. De Heer, D.-H. Lee, F. Guinea, A. H. C. Neto, and A. Lanzara, *Substrate-induced bandgap opening in epitaxial graphene*, *Nature Materials* **6**, 770 (2007).
- [13] A. Romero-Bermúdez and A. M. García-García, *Size effects in superconducting thin films coupled to a substrate*, *Physical Review B* **89**, 064508 (2014).
- [14] G. Profeta, M. Calandra, and F. Mauri, *Phonon-mediated superconductivity in graphene by lithium deposition*, *Nature Physics* **8**, 131 (2012).

- [15] R. Nandkishore, L. S. Levitov, and A. V. Chubukov, *Chiral superconductivity from repulsive interactions in doped graphene*, *Nature Physics* **8**, 158 (2012).
- [16] E. Uesugi, H. Goto, R. Eguchi, A. Fujiwara, and Y. Kubozono, *Electric double-layer capacitance between an ionic liquid and few-layer graphene*, *Scientific Reports* **3**, 1595 (2013).
- [17] J. A. Wilson and A. D. Yoffe, *The transition metal dichalcogenides discussion and interpretation of the observed optical, electrical and structural properties*, *Advances in Physics* **18**, 193 (1969).
- [18] R. H. Friend and A. D. Yoffe, *Electronic properties of intercalation complexes of the transition metal dichalcogenides*, *Advances in Physics* **36**, 1 (1987).
- [19] G. Cunningham, M. Lotya, C. S. Cucinotta, S. Sanvito, S. D. Bergin, R. Menzel, M. S. P. Shaffer, and J. N. Coleman, *Solvent exfoliation of transition metal dichalcogenides: dispersibility of exfoliated nanosheets varies only weakly between compounds*, *ACS Nano* **6**, 3468 (2012).
- [20] E. Coronado, C. Martí-Gastaldo, E. Navarro-Moratalla, A. Ribera, S. J. Blundell, and P. J. Baker, *Coexistence of superconductivity and magnetism by chemical design*, *Nature Chemistry* **2**, 1031 (2010).
- [21] E. Coronado, C. Martí-Gastaldo, E. Navarro-Moratalla, E. Burzurí, A. Camón, and F. Luis, *Hybrid magnetic/superconducting materials obtained by insertion of a single-molecule magnet into TaS<sub>2</sub> layers*, *Advanced Materials* **23**, 5021 (2011).
- [22] M. A. Meitl, Z.-T. Zhu, V. Kumar, K. J. Lee, X. Feng, Y. Y. Huang, I. Adesida, R. G. Nuzzo, and J. A. Rogers, *Transfer printing by kinetic control of adhesion to an elastomeric stamp*, *Nature Materials* **5**, 33 (2006).
- [23] C. Lee, Q. Li, W. Kalb, X.-Z. Liu, H. Berger, R. W. Carpick, and J. Hone, *Frictional characteristics of atomically thin sheets*, *Science* **328**, 76 (2010).
- [24] K. F. Mak, C. Lee, J. Hone, J. Shan, and T. F. Heinz, *Atomically thin MoS<sub>2</sub>: a new direct-gap semiconductor*, *Physical Review Letters* **105**, 136805 (2010).
- [25] A. Splendiani, L. Sun, Y. Zhang, T. Li, J. Kim, C.-Y. Chim, G. Galli, and F. Wang, *Emerging photoluminescence in monolayer MoS<sub>2</sub>*, *Nano Letters* **10**, 1271 (2010).
- [26] C. Chiriac, D. G. Cahill, N. Nguyen, D. Johnson, A. Bodapati, P. Keblinski, and P. Zschack, *Ultralow thermal conductivity in disordered, layered WSe<sub>2</sub> crystals*, *Science* **315**, 351 (2007).
- [27] R. F. Frindt, *Superconductivity in ultrathin NbSe<sub>2</sub> layers*, *Physical Review Letters* **28**, 299 (1972).
- [28] N. E. Staley, J. Wu, P. Eklund, Y. Liu, L. Li, and Z. Xu, *Electric field effect on superconductivity in atomically thin flakes of NbSe<sub>2</sub>*, *Physical Review B* **80**, 184505 (2009).

- [29] M. S. El-Bana, D. Wolverson, S. Russo, G. Balakrishnan, D. M. Paul, and S. J. Bending, *Superconductivity in two-dimensional NbSe<sub>2</sub> field effect transistors*, *Superconductor Science and Technology* **26**, 125020 (2013).
- [30] Q. Li, W. Si, and I. K. Dimitrov, *Films of iron chalcogenide superconductors*, *Reports on Progress in Physics* **74**, 124510 (2011).
- [31] D. Liu, W. Zhang, D. Mou, J. He, Y.-B. Ou, Q.-Y. Wang, Z. Li, L. Wang, L. Zhao, S. He, *et al.*, *Electronic origin of high-temperature superconductivity in single-layer FeSe superconductor*, *Nature Communications* **3**, 931 (2012).
- [32] S. He, J. He, W. Zhang, L. Zhao, D. Liu, X. Liu, D. Mou, Y.-B. Ou, Q.-Y. Wang, Z. Li, *et al.*, *Phase diagram and electronic indication of high-temperature superconductivity at 65 K in single-layer FeSe films*, *Nature Materials* **12**, 605 (2013).
- [33] R. Yu, P. Goswami, Q. Si, P. Nikolic, and J.-X. Zhu, *Superconductivity at the border of electron localization and itinerancy*, *Nature Communications* **4**, 2783 (2013).
- [34] Y. Cao, A. Mishchenko, G. Yu, E. Khestanova, A. Rooney, E. Prestat, A. Kretinin, P. Blake, M. Shalom, C. Woods, *et al.*, *Quality heterostructures from two-dimensional crystals unstable in air by their assembly in inert atmosphere*, *Nano Letters* **15**, 4914 (2015).
- [35] X. Xi, L. Zhao, Z. Wang, H. Berger, L. Forró, J. Shan, and K. F. Mak, *Strongly enhanced charge-density-wave order in monolayer NbSe<sub>2</sub>*, *Nature Nanotechnology* **10**, 765 (2015).
- [36] X. Xi, Z. Wang, W. Zhao, J.-H. Park, K. T. Law, H. Berger, L. Forró, J. Shan, and K. F. Mak, *Ising pairing in superconducting NbSe<sub>2</sub> atomic layers*, *Nature Physics* **12**, 139 (2016).
- [37] A. W. Tsien, B. Hunt, Y. D. Kim, Z. J. Yuan, S. Jia, R. J. Cava, J. Hone, P. Kim, C. R. Dean, and A. N. Pasupathy, *Nature of the quantum metal in a two-dimensional crystalline superconductor*, *Nature Physics* **12**, 208 (2016).
- [38] F. Jellinek, *The system tantalum-sulfur*, *Journal of the Less Common Metals* **4**, 9 (1962).
- [39] A. H. C. Neto, *Charge density wave, superconductivity, and anomalous metallic behavior in 2D transition metal dichalcogenides*, *Physical Review Letters* **86**, 4382 (2001).
- [40] I. Guillamon, H. Suderow, J. G. Rodrigo, S. Vieira, P. Rodiere, L. Cario, E. Navarro-Moratalla, C. Marti-Gastaldo, and E. Coronado, *Chiral charge order in the superconductor 2H-TaS<sub>2</sub>*, *New Journal of Physics* **13**, 103020 (2011).
- [41] L. Stojchevska, I. Vaskivskiy, T. Mertelj, P. Kusar, D. Svetin, S. Brazovskii, and D. Mihailovic, *Ultrafast switching to a stable hidden quantum state in an electronic crystal*, *Science* **344**, 177 (2014).

- [42] J. A. Galvis, L. Chirulli, I. Guillamón, S. Vieira, E. Navarro-Moratalla, E. Coronado, H. Suderow, and F. Guinea, *Zero-bias conductance peak in detached flakes of superconducting 2H-TaS<sub>2</sub> probed by scanning tunneling spectroscopy*, *Physical Review B* **89**, 224512 (2014).
- [43] A. Ayari, E. Cobas, O. Ogundadegbe, and M. S. Fuhrer, *Realization and electrical characterization of ultrathin crystals of layered transition-metal dichalcogenides*, *Journal of Applied Physics* **101**, 14507 (2007).
- [44] N. N. Greenwood and A. Earnshaw, *Chemistry of the Elements 2nd Edition* (Butterworth-Heinemann, 1997).
- [45] E. Navarro Moratalla, *Two-dimensional materials: from hybrid magnetic multilayers to superconducting single layers*, Ph.D. thesis, University of Valencia (2013).
- [46] E. Navarro-Moratalla, E. Pinilla-Cienfuegos, and E. Coronado, *Metodo y sistema de exfoliacion micromecanica por via seca de materiales laminares bidimensionales*, (2014).
- [47] P. Garoche, P. Manuel, J. J. Veyssié, and P. Molinié, *Dynamic measurements of the low-temperature specific heat of 2H-TaS<sub>2</sub> single crystals in magnetic fields*, *Journal of Low Temperature Physics* **30**, 323 (1978).
- [48] A. V. Gurevich and R. G. Mints, *Self-heating in normal metals and superconductors*, *Reviews of Modern Physics* **59**, 941 (1987).
- [49] J. L. Vicent, S. J. Hillenius, and R. V. Coleman, *Critical-field enhancement and reduced dimensionality in superconducting layer compounds*, *Physical Review Letters* **44**, 892 (1980).
- [50] F. J. Di Salvo, R. Schwall, T. H. Geballe, F. R. Gamble, and J. H. Osiecki, *Superconductivity in layered compounds with variable interlayer spacings*, *Physical Review Letters* **27**, 310 (1971).
- [51] L. Kang, B. B. Jin, X. Y. Liu, X. Q. Jia, J. Chen, Z. Ji, W. W. Xu, P. H. Wu, S. B. Mi, A. Pimenov, *et al.*, *Suppression of superconductivity in epitaxial NbN ultrathin films*, *Journal of Applied Physics* **109**, 033908 (2011).
- [52] K. E. Wagner, E. Morosan, Y. S. Hor, J. Tao, Y. Zhu, T. Sanders, T. M. McQueen, H. W. Zandbergen, A. J. Williams, D. V. West, *et al.*, *Tuning the charge density wave and superconductivity in Cu<sub>x</sub>TaS<sub>2</sub>*, *Physical Review B* **78**, 104520 (2008).
- [53] M. Hangyo, S.-I. Nakashima, and A. Mitsuishi, *Raman spectroscopic studies of MX<sub>2</sub>-type layered compounds*, *Ferroelectrics* **52**, 151 (1983).
- [54] Y. Zhang, Y.-W. Tan, H. L. Stormer, and P. Kim, *Experimental observation of the quantum Hall effect and Berry's phase in graphene*, *Nature* **438**, 201 (2005).
- [55] M. Naito and S. Tanaka, *Electrical transport properties in 2H-NbS<sub>2</sub>, -NbSe<sub>2</sub>, -TaS<sub>2</sub> and -TaSe<sub>2</sub>*, *Journal of the Physical Society of Japan* **51**, 219 (1982).

- [56] W. Biberacher, A. Lerf, F. Buheitel, T. Butz, and A. Hübler, *On the preparation and characterization of "NaOH-TaS<sub>2</sub>"*, Materials Research Bulletin **17**, 633 (1982).
- [57] Y. Feng, J. Wang, R. Jaramillo, J. Van Wezel, S. Haravifard, G. Srajer, Y. Liu, Z.-A. Xu, P. B. Littlewood, and T. F. Rosenbaum, *Order parameter fluctuations at a buried quantum critical point*, Proceedings of the National Academy of Sciences **109**, 7224 (2012).
- [58] P. Morel and P. W. Anderson, *Calculation of the superconducting state parameters with retarded electron-phonon interaction*, Physical Review **125**, 1263 (1962).
- [59] K. Taniguchi, A. Matsumoto, H. Shimotani, and H. Takagi, *Electric-field-induced superconductivity at 9.4 k in a layered transition metal disulphide MoS<sub>2</sub>*, Applied Physics Letters **101**, 042603 (2012).
- [60] J. T. Ye, Y. J. Zhang, R. Akashi, M. S. Bahramy, R. Arita, and Y. Iwasa, *Superconducting dome in a gate-tuned band insulator*, Science **338**, 1193 (2012).
- [61] R. Roldán, E. Cappelluti, and F. Guinea, *Interactions and superconductivity in heavily doped MoS<sub>2</sub>*, Physical Review B **88**, 054515 (2013).
- [62] H. Li, G. Lu, Z. Yin, Q. He, H. Li, Q. Zhang, and H. Zhang, *Optical identification of single- and few-layer MoS<sub>2</sub> sheets*, Small **8**, 682 (2012).
- [63] A. Castellanos-Gomez, E. Navarro-Moratalla, G. Mokry, J. Queda, E. Pinilla-Cienfuegos, N. Agraït, H. S. J. van der Zant, E. Coronado, G. A. Steele, and G. Rubio-Bollinger, *Fast and reliable identification of atomically thin layers of TaSe<sub>2</sub> crystals*, Nano Research **6**, 191 (2013).
- [64] J. Kivavle, C. Bell, J. Henrie, S. Schultz, and A. Hawkins, *Improvement to reflective dielectric film color pictures*, Optics Express **12**, 5789 (2004).
- [65] P. Blake, E. W. Hill, A. H. C. Neto, K. S. Novoselov, D. Jiang, R. Yang, T. J. Booth, and A. K. Geim, *Making graphene visible*, Applied Physics Letters **91**, 063124 (2007).
- [66] A. Castellanos-Gomez, N. Agraït, and G. Rubio-Bollinger, *Optical identification of atomically thin dichalcogenide crystals*, Applied Physics Letters **96**, 213116 (2010).
- [67] A. Castellanos-Gomez, M. Wojtaszek, N. Tombros, N. Agraït, B. J. van Wees, and G. Rubio-Bollinger, *Atomically thin mica flakes and their application as ultrathin insulating substrates for graphene*, Small **7**, 2491 (2011).
- [68] M. M. Benameur, B. Radisavljevic, J. S. Heron, S. Sahoo, H. Berger, and A. Kis, *Visibility of dichalcogenide nanolayers*, Nanotechnology **22**, 125706 (2011).
- [69] A. R. Beal, H. P. Hughes, and W. Y. Liang, *The reflectivity spectra of some group VA transition metal dichalcogenides*, Journal of Physics C: Solid State Physics **8**, 4236 (1975).
- [70] M. Zhu, Z. Zhang, and W. Miao, *Intense photoluminescence from amorphous tantalum oxide films*, Sensors **5**, 7 (2006).

- [71] Y. Wu, M. An, R. Xiong, J. Shi, and Q. M. Zhang, *Raman scattering spectra in the normal phase of 2H-NbSe<sub>2</sub>*, *Journal of Physics D: Applied Physics* **41**, 175408 (2008).
- [72] G. Plechinger, S. Heydrich, J. Eroms, D. Weiss, C. Schuller, and T. Korn, *Raman spectroscopy of the interlayer shear mode in few-layer MoS<sub>2</sub> flakes*, *Applied Physics Letters* **101**, 101906 (2012).
- [73] G. Plechinger, S. Heydrich, M. Hirmer, F.-X. Schrettenbrunner, D. Weiss, J. Eroms, C. Schüller, and T. Korn, *Scanning raman spectroscopy of few- and single-layer MoS<sub>2</sub> flakes*, in *SPIE NanoScience+ Engineering* (International Society for Optics and Photonics, 2012) pp. 84630N–84630N.
- [74] J. M. Soler, E. Artacho, J. D. Gale, A. García, J. Junquera, P. Ordejón, and D. Sánchez-Portal, *The SIESTA method for ab initio order-N materials simulation*, *Journal of Physics: Condensed Matter* **14**, 2745 (2002).
- [75] J. P. Perdew, K. Burke, and M. Ernzerhof, *Generalized gradient approximation made simple*, *Physical Review Letters* **77**, 3865 (1996).
- [76] E. Artacho, D. Sánchez-Portal, P. Ordejón, A. Garcia, and J. M. Soler, *Linear-scaling ab-initio calculations for large and complex systems*, *Physica Status Solidi B* **215**, 809 (1999).
- [77] H. J. Monkhorst and J. D. Pack, *Special points for Brillouin-zone integrations*, *Physical Review B* **13**, 5188 (1976).
- [78] A. Meetsma, G. A. Wiegers, R. J. Haange, and J. L. De Boer, *Structure of 2H-TaS<sub>2</sub>*, *Acta Crystallographica Section C* **46**, 1598 (1990).





# 8

## CONCLUSION

Concluding, this thesis has presented the recent interest in hybrid superconducting devices and investigated such devices in two material systems. We developed two platforms to study superconducting phenomena in hybrid molecular devices which both rely on the proximity effect to preserve existing bonding chemistries for molecular junctions. In the first one we fabricate few-layer graphene break-junctions with superconducting molybdenum-rhenium (MoRe) electrodes and in the second one we fabricate gold break-junctions with superconducting MoRe electrodes. The second platform is then used to investigate the properties of a hybrid molecular device consisting of an all organic radical in a superconducting junction. In these devices we observe Yu-Shiba-Rusinov (Shiba) excited states as a result of the interaction of the radical's spin with the proximity induced superconducting electrodes.

In the second half of the thesis we investigated the thickness dependent properties of two layered materials. Using molybdenum disulfide ( $\text{MoS}_2$ ) we fabricated hybrid superconducting devices with MoRe electrodes and studied the thickness dependent properties of vertical junctions. We found that the single and bilayer devices present high transparencies and subgap structure given by multiple Andreev reflections (MAR). In thicker devices we observed lower transparencies and mini quasiparticle gaps due to tunneling through a potential barrier. We finally studied the thickness depended superconducting properties of tantalum disulfide ( $\text{TaS}_2$ ). We characterized the critical temperature and critical field of flakes of different thicknesses and found that the superconducting properties became stronger for thinner flakes. This was attributed to an increase in the effective electron-phonon coupling constant in ultra-thin flakes.

### 8.1. IMPROVEMENTS AND OUTLOOK

Here I give suggestions for improvements and future directions for the projects presented in this thesis. As discussed in chapter 3 section 3.4, further investigations of the nature of the proximity effect in few-layer graphene are required before hybrid devices can be studied at low temperatures. Additionally, we met several obstacles that severely

dropped device yields. This is detrimental to the project as molecular device yields are typically less than 10%. We found that several unpatterned devices (roughly 30%) did not present a zero resistive supercurrent at low temperatures. While annealing the samples could alleviate this drop in initial device yield, further complications arose. The supercurrent is gate tunable in unpatterned devices which is not expected in 10 nm thick devices given a screening length of 2-3 layers in multi-layer graphene. This points to a more complicated proximity effect in multi-layer flakes which is not simply proximity induced superconductivity evenly distributed through the whole flake. For further studies of this system I would recommend several improvements. Patterning individual electrodes to single flakes is not only time consuming but also limits the number of junctions on a single chip. Typically we were able to find enough 10 nm thick flakes in order to pattern 15 devices on one chip. If the creation of the constriction is successful in all junctions (this is not always the case as misalignment or over etching will render some junctions unusable) then the expected yield for molecular devices (junctions in which the presence of a gateable entity is present) is roughly 1-2 (given < 10% yields in general).

Instead CVD grown single layer graphene could be employed to alleviate the need to spot-pattern individual devices. Indeed, some groups have moved in this direction[1-3]. Using commercially available CVD graphene on Si/SiO<sub>2</sub> substrates would allow one to pattern more junctions on a single chip. The constriction or bow-tie geometry could then be patterned with a single e-beam lithography step and subsequent oxygen plasma etching. This will improve on the number of junctions available on a single chip. I would then recommend a high temperature anneal to improve the connection to the MoRe electrodes. With improved yields, a systematic study of junctions before and after electroburning should be performed and subsequently investigation into hybrid molecular devices. The device yields are the bottle-neck toward better understanding of the graphene-molecule junction which also requires further investigation.

While progress with the second hybrid molecular device platform advanced faster than the graphene based one, many improvements can be made. The proximity induced gold junctions allowed us to progress quickly because we borrowed existing knowledge of electromigration and self-breaking of gold nanowires and known bonding chemistries. However, the proximity induced gaps resulting from the gold are soft and typically have low critical fields (a few hundred mT). A hard superconducting gap would be more desirable, naturally, so that excitations within the gap are clearly visible. This is a recent advancement in hybrid nanowire devices using epitaxial growth of aluminum instead of direct evaporation[4]. In order to create a hard gap in hybrid molecular devices, a possible solution is the direct electromigration of a superconductor. This presents several obstacles as nanogap formation in superconducting nanowires is relatively unexplored and scarcely little is known about the chemical bonding between conventionally used superconductors and molecule anchoring groups. Electromigration of aluminum and lead has been reported with limited success[5, 6]. Aluminum results in only weakly coupled molecule junctions[5] and lead presents unstable molecular junctions measured at 4.2 K[6].

Alternatively, several improvements can be made to the proximity induced junctions where stable, intermediately coupled junctions can be achieved. The first improvement would be the localization of the nanogap to the center of the nanowire so

as to create a more symmetric proximity induced density of states between the right and left electrodes. This can be achieved by patterning a constriction in the nanowire (a weak point) where the gap will form during electromigration. The second improvement would be bringing the bulk superconducting electrodes closer together to make a shorter nanowire section. This presents problems as the power required to perform the electromigration increases as we reduce the spacing between the bulk electrodes. This could be due to better thermal coupling to the nanowire which reduces the Joule heating induced hot spots necessary for the electromigration process[7]. The bulk superconducting electrodes could be patterned to conform to a bow-tie geometry near the nanowire reducing the amount of material near the center of the nanowire. These improvements would allow for a harder proximity induced gap which is nearly identical for each electrode.

With these improvements, the subgap state energy of the excited Shiba states could be determined directly and the first interesting experiment would be an investigation of the singlet-doublet phase transition in molecular hybrid devices. The bound state energy ( $E_b$ ) evolves gradually as a function of the Kondo energy strength (in other words the coupling). By probing samples with different Kondo energies (as we have done in chapter 5) for the same proximity induced gap energy ( $\Delta$ ), one could map the phase transition from the doublet (weak Kondo,  $T_k < \Delta$ ) to the singlet (strong Kondo,  $T_k > \Delta$ ). This has been extensively researched theoretically but experimental investigations are scarce. Alternatively, this transition could be mapped in-situ by an appropriate choice of a molecule. Some molecules present largely tunable Kondo energies within a single charge state. This would allow for probing the phase transition in a single charge state and in a single device. For example, Figure 8.1 shows stability plots for a hybrid molecular device in the normal and superconducting states. This molecule, a thiolated arylethynylene with a 9,10-dihydroanthracene (AH) core, allows tuning of the Kondo energy for the charge state on the right side of the plot. For comparable energies ( $T_K \approx \Delta$ ), this molecule allows exploration of the singlet to doublet quantum phase transition.

In the experiments on hybrid devices incorporating the layered material MoS<sub>2</sub>, a central consideration is the presence of pinholes. The prevalence of pinholes in the single layer devices could be studied with statistics on junctions with different areas. If pinholes are dominating the transport characteristics, junctions having different contact areas would not alter, significantly, the low temperature measurements. Alternatively however, if pinholes are not present, the current and critical current in the superconducting state should scale with contact area. Additionally, cross-sectional transmission electron microscopy would perhaps also provide direct evidence of such pinholes.

A simple continuation of these hybrid devices is to fabricate junctions with different layered materials as the weak link. Boron nitride is an insulating layered material and could be an interesting replacement to the conventionally employed Al/AlOx Josephson junction. It has been shown that only 10 % of the junction area in an Al/AlOx junctions contributes to the total current through the junction[8, 9] and that electrical properties of the junctions are strongly dependent on local non-uniformities in thickness[10]. A single crystal barrier could present more homogeneous tunnel currents and reproducible electrical characteristics. Figure 8.2(a-b) shows one vertical device in which we used boron nitride as the insulating barrier. The thickness was estimated from the room temperature resistance to be approximately 3 layers. The low temperature transport measure-

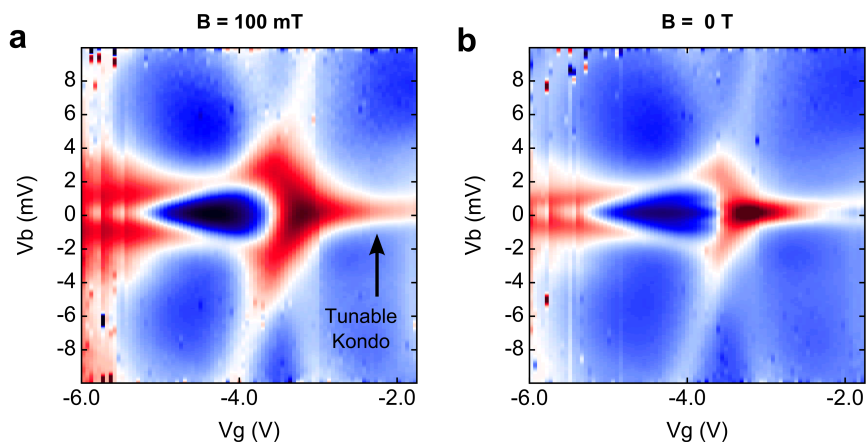


Figure 8.1: (a) Normal state ( $B = 100$  mT) colorplot of the measured conductance as a function of bias and gate voltage for a hybrid molecular device. (b) Superconducting state ( $B = 0$  T) colorplot of the measured conductance as a function of bias and gate voltage for the same device.

ments did not reveal the presence of a supercurrent although a low energy gap seems to be present, Figure 8.2(c).

Regarding the thickness depended superconducting properties of tantalum disulfide, an initial advancement would be the use of recent encapsulation techniques to prevent oxidation of the flakes. It was noted that samples below the thinnest sample studied (3.5 nm) presented insulating characteristics after fabrication. It is most likely that these thinner samples degrade faster in ambient conditions and as a result prevent investigation without some sort of encapsulation. Encapsulation techniques using other 2D materials two sandwich an protect a materials under study have been developed in several studies. The most notable is the use of boron nitride (BN) as a substrate and a

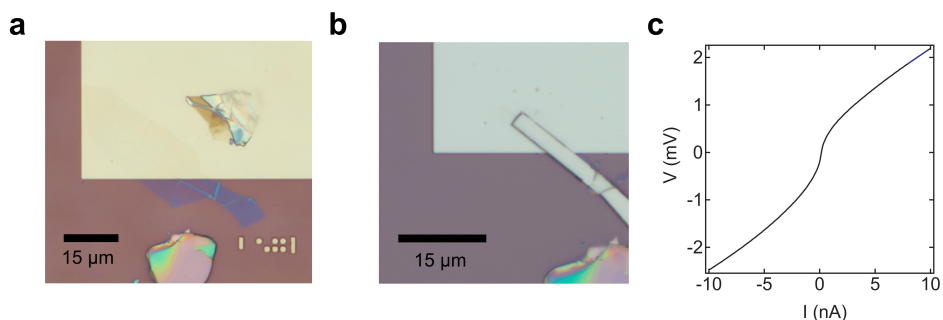


Figure 8.2: (a) Optical image of the flake after being transferred onto prepatterned a MoRe electrode. (b) Optical image after fabrication of the top electrode. (c) Low temperature current bias measurement of the stack.

top encapsulating layer. BN has also been used to prevent degradation of other recently explored 2D materials such as black phosphorus and niobium diselenide. BN encapsulation would allow protection of TaS<sub>2</sub> samples down to a single layer and the limit of the interesting enhancement of the superconducting properties could be discerned.

Another step toward investigating the mechanism responsible for the enhancement in TaS<sub>2</sub> would be ionic liquid gating in order to map (partially) the phase diagram of the material for different thicknesses. This has been explored in recent studies on the sister compound NbSe<sub>2</sub> [11, 12] where the superconducting properties can be modulated. Also mentioned in chapter 7 is the exploration of the charge density wave instability in TaS<sub>2</sub> and its affect on superconductivity. Scanning tunneling microscopy (STM) studies of the CDW in TaS<sub>2</sub> as a function of thickness would corroborate our calculations that suggest the CDW does not appreciably affect the density of states at the Fermi energy.

These suggestions encompass the directions I would take in each of the projects presented in this thesis.

## REFERENCES

- [1] Y. Cao, S. Dong, S. Liu, L. He, L. Gan, X. Yu, M. L. Steigerwald, X. Wu, Z. Liu, and X. Guo, *Building high-throughput molecular junctions using indented graphene point contacts*, *Angewandte Chemie* **124**, 12394 (2012).
- [2] S. Seo, M. Min, S. M. Lee, and H. Lee, *Photo-switchable molecular monolayer anchored between highly transparent and flexible graphene electrodes*, *Nature Communications* **4**, 1920 (2013).
- [3] K. Ullmann, P. B. Coto, S. Leitherer, A. Molina-Ontoria, N. Martín, M. Thoss, and H. B. Weber, *Single-molecule junctions with epitaxial graphene nanoelectrodes*, *Nano Letters* **15**, 3512 (2015).
- [4] W. Chang, S. M. Albrecht, T. S. Jespersen, F. Kueemeth, P. Krogstrup, J. Nygård, and C. M. Marcus, *Hard gap in epitaxial semiconductor-superconductor nanowires*, *Nature Nanotechnology* **10**, 232 (2015).
- [5] C. B. Winkelmann, N. Roch, W. Wernsdorfer, V. Bouchiat, and F. Balestro, *Superconductivity in a single-C<sub>60</sub> transistor*, *Nature Physics* **5**, 876 (2009).
- [6] K. Luo and Z. Yao, *Fabrication of nanometer-spaced superconducting Pb electrodes*, *Applied Physics Letters* **95**, 113115 (2009).
- [7] W. Jeong, K. Kim, Y. Kim, W. Lee, and P. Reddy, *Characterization of nanoscale temperature fields during electromigration of nanowires*, *Scientific Reports* **4** (2014).
- [8] T. Aref, A. Averin, S. van Dijken, A. Ferring, M. Koberidze, V. Maisi, H. Q. Nguyend, R. M. Nieminen, J. P. Pekola, and L. D. Yao, *Characterization of aluminum oxide tunnel barriers by combining transport measurements and transmission electron microscopy imaging*, *Journal of Applied Physics* **116**, 073702 (2014).

- [9] L. J. Zeng, S. Nik, T. Greibe, P. Krantz, C. M. Wilson, P. Delsing, and E. Olsson, *Direct observation of the thickness distribution of ultra thin  $AlO_x$  barriers in  $Al/AlO_x/Al$  Josephson junctions*, *Journal of Physics D: Applied Physics* **48**, 395308 (2015).
- [10] P. Y. Aghdam, H. M. Rashid, A. Pavolotsky, V. Desmaris, and V. Belitsky, *Dependence of the scatter of the electrical properties on local non-uniformities of the tunnel barrier in  $Nb/Al-AlO_x/Nb$  junctions*, *Journal of Applied Physics* **119**, 054502 (2016).
- [11] Z. J. Li, B. F. Gao, J. L. Zhao, X. M. Xie, and M. H. Jiang, *Effect of electrolyte gating on the superconducting properties of thin  $2H-NbSe_2$  platelets*, *Superconductor Science and Technology* **27**, 015004 (2013).
- [12] M. Yoshida, J. Ye, T. Nishizaki, N. Kobayashi, and Y. Iwasa, *Electrostatic and electrochemical tuning of superconductivity in two-dimensional  $NbSe_2$  crystals*, *Applied Physics Letters* **108**, 202602 (2016).

# SUMMARY

In this thesis we investigate superconducting hybrids made from two material systems, namely, molecules and layered materials. For studies of superconducting phenomena in molecular junctions we develop two platforms which rely on the superconducting proximity effect to preserve pre-existing nano-gap formation techniques and bonding chemistries. In the second half of this thesis we investigate the thickness dependent properties of the 2H crystal phase of two layered materials; molybdenum disulfide (2H-MoS<sub>2</sub>) and tantalum disulfide (2H-TaS<sub>2</sub>).

In chapter 1 we introduce the conception of the hybrid superconducting device and review recent progress and interests in these devices. We then introduce the field of molecular electronics and the current status of hybrid devices. We summarize our recent contributions to this newly opening field with the investigation of two types of hybrid devices. In the last part of the chapter we summarize the field of layered materials which has quickly grown from the success of graphene. The current research on quantum confinement effects in layered materials is reviewed and two experiments in this thesis are summarized.

In chapter 2 we review the theoretical background which aids in interpreting the experimental results presented throughout this thesis. We first recall the proposals of tunneling supercurrents by Josephson in the early 1960s. We then derive and calculate the probability of Andreev reflection between a normal metal and a superconductor. This is extended to include multiple Andreev reflections. The modified density of states in long metallic Josephson junctions is discussed which forms the understanding of proximity effect in the experimental system presented in chapter 4. We finish the chapter with a handling of the modified Anderson model which describes the experimental hybrid molecular devices presented in chapter 5. We cover the weakly and strongly interacting regimes in which the Andreev and Shiba bound states can be observed, respectively.

In the next two chapters we present the two experimental systems developed for the study of superconducting phenomena in hybrid molecular devices. In the first platform (chapter 3) we improved on the yield (15 % increase) and stability of multi-layer graphene electrodes with gold electrodes by creating a constriction in the flakes using a helium ion microscope or an oxygen plasma etch. The constriction allowed us to not only localize the formation of a nano-gap created by electroburning but also lower the critical powers required to start the electroburning process. The lower powers proved instrumental in fabricating hybrid devices in which the gold electrodes are replaced by a bulk superconductor. We found that even when using a superconducting alloy with a high melting temperature (estimated to reach 1200 K) on unpatterned flakes (without a constriction), the creation of the nano-gap during electroburning would melt the electrodes which need to be placed within 500 nm of the gap to induce superconducting proximity effects. This made the formation of a constriction essential in fabricating these types of hybrid devices with closely spaced electrodes. As a proof-of-principle, we use

anthracene functionalized copper curcuminoid molecules to fabricate a hybrid device at room temperature.

In the second platform (chapter 4) we built on the knowledge of electromigrated gold nanowires to fabricate hybrid devices using the superconducting alloy molybdenum-rhenium (MoRe). We first demonstrate the proximity induced nature of the gold leads by measuring the low temperature transport characteristics of empty electromigrated gaps. We find that a proximity induced soft gap of 0.7 meV occurs at low temperatures (100 mK). The soft gap persists to temperatures of 4.6 K and fields up to 6 T. Furthermore, we measure the low temperature transport characteristics of a hybrid molecular device consisting of an  $\text{Fe}_4$  single molecule magnet in a proximity induced superconducting junction. We observe the coexistence of Coulomb blockade and a proximity induced superconducting gap and reach the regime of intermediate coupling ( $\Gamma \Delta$ ) necessary to explore the competition between Kondo screening and Cooper pairing.

Using the second platform described in chapter 4, we study a hybrid molecular device created by combining an all organic radical molecule with a superconducting junction in chapter 5. We first present transport measurements that reveal excitations which are characteristic of a spin-induced Shiba state due to the interaction of the radical's unpaired spin with a strongly-coupled, proximity-induced superconductor. Suppressing proximity induced superconductivity with a magnetic field gives rise to a zero bias peak signaling Kondo screening of the radical's unpaired spin coupled to normal leads. We find that by virtue of a variable molecule-electrode coupling, we are able to access both the singlet and doublet ground states of the hybrid system which leads to the doublet and singlet Shiba excited states, respectively. We further corroborate these results through calculations based on the Anderson model while taking into account the proximity-induced nature of the gold leads.

In the second half of this thesis we present experiments involving superconductivity and another material system, namely, layered van der Waals materials. In chapter 6 we fabricate and study the low temperature transport characteristics of hybrid Josephson junctions combining the layered material  $\text{MoS}_2$  and molybdenum rhenium (MoRe). In particular, we present observations of thickness dependent Josephson coupling and multiple Andreev reflections (MAR) in vertically stacked  $\text{MoS}_2$  - MoRe Josephson junctions. MoRe, a chemically inert superconductor, allows for oxide free fabrication of high transparency vertical  $\text{MoS}_2$  devices (transparencies up to 80 %). Single and bilayer  $\text{MoS}_2$  junctions display relatively large critical currents (up to  $2.5 \mu\text{A}$ ) and the appearance of sub-gap structure given by MAR. In three and four layer thick devices we observe orders of magnitude lower critical currents (sub-nA) and reduced quasiparticle gaps due to proximitized  $\text{MoS}_2$  layers in contact with MoRe.

Chapter 7 investigates the thickness dependent properties of the layered materials 2H-TaS<sub>2</sub>. We first present the transport properties of electronic devices based on 2H-TaS<sub>2</sub> flakes of different thicknesses. We observe that superconductivity persists down to the thinnest layer investigated (3.5 nm), and interestingly, we find a pronounced enhancement in the critical temperature from 0.5 K to 2.2 K as the layers are thinned down. We present band structure calculations of few-layer TaS<sub>2</sub> flakes to theoretically investigate the observed enhancement. By generalizing the Anderson-Morel model to account for a generic density of states, we suggest the enhancement is due to an increase in the



effective electron–phonon coupling constant for sufficiently large bare Coulomb repulsion.

In the concluding chapter, 8, we discuss the outcomes of each experiment, providing suggestions for improvement where possible, and summarizing possible directions for advancement.



# SAMENVATTING

In deze scriptie onderzoeken we supergeleidende hybride systemen gemaakt van twee materiaalsystemen, namelijk, moleculen en gelaagde materialen. Voor het bestuderen van supergeleidende verschijnselen in moleculaire juncties ontwikkelen we twee platformen die gebruik maken van het supergeleidende nabijheidseffect om bestaande technieken voor het maken van nanogaps en de bindingschemie te behouden. In de tweede helft van deze scriptie onderzoeken we de dikteafhankelijke eigenschappen van de 2H-kristallijne fase van twee gelaagde materialen; molybdenum disulfide (2H-MoS<sub>2</sub>) en tantaal disulfide (2H-TaS<sub>2</sub>).

In hoofdstuk 1 introduceren wij het concept van een hybride supergeleidend apparaat en bespreken we recente ontwikkelingen en interesses in deze apparaten. Vervolgens introduceren we het veld van moleculaire elektronica en de huidige status van hybride apparaten. We vatten onze recente bijdragen in dit nieuwe veld samen met studies van twee types hybride apparaten. In het laatste deel van dit hoofdstuk geven we een overzicht van het veld van gelaagde materialen, wat snel gegroeid is door behaalde successen met grafeen. Huidig onderzoek naar kwantumopsluiting in gelaagde materialen wordt besproken en twee experimenten worden in deze scriptie samengevat.

In hoofdstuk 2 bespreken we de theoretische achtergrond die als ondersteuning dient voor de interpretatie van de gepresenteerde experimentele resultaten. Eerst behandelen we het concept van tunnel-superstromen, dat door Josephson is geïntroduceerd in het begin van de jaren 60. Daarna berekenen we en leiden we de waarschijnlijkheid van Andreev-reflectie tussen een normaal metaal en een supergeleider af. Dit wordt generaliseerd om meervoudige Andreev-reflectie te beschrijven. Vervolgens bespreken we de aangepaste toestandsdichtheid in lange metallische Josephson-juncties wat als beschrijving dient voor het nabijheidseffect in het experimentele systeem uit hoofdstuk 4. We sluiten het hoofdstuk af met de introductie van een aangepast Anderson model dat de experimentele hybride moleculaire apparaten uit hoofdstuk 5 beschrijft. We behandelen zowel het regime van zwakke interactie, als wel het regime van sterke interactie, waarin respectievelijk gebonden Andreev- en Shiba-toestanden tot uiting komen.

In de twee volgende hoofdstukken presenteren we twee experimentele systemen die ontwikkeld zijn voor het bestuderen van supergeleidende verschijnselen in hybride moleculaire apparaten. In het eerste platform (hoofdstuk 3) hebben we de opbrengst (15 % toename) en de stabiliteit van multilaag-grafeen elektrodes met gouden elektrodes verbeterd door een constrictie in het grafeen te maken met een helium-ion microscoop of een zuurstof-plasma ets. De constrictie stelde ons in staat om zowel de formatie van de nanogap te lokaliseren tijdens het elektrobranden, als wel het benodigde vermogen voor het elektrobranden te verlagen. Lagere vermogens bleken essentieel in de fabricage van hybride apparaten waarin gouden elektrodes zijn vervangen door een bulk supergeleider. Zonder constrictie in het grafeen bleken elektrodes van supergeleidende legeringen met een hogere smelttemperatuur (geschat op 1200 K) te smelten bij de formatie van een

nanogap tijdens het elektrobranden. Deze elektrodes moesten op 500 nm van de nanogap geplaatst om supergeleidende eigenschappen in de junctie te induceren. Hierdoor was een constrictie essentieel in de fabricage van deze hybride apparaten met elektrodes die op korte afstand van elkaar liggen. Als ‘proof of concept’ hebben we een hybride systeem met antraceen-gefunctionaliseerde curcuminoïde moleculen op kamertemperatuur gefabriceerd.

In het tweede platform (hoofdstuk 4) gebruiken we de opgebouwde kennis van het elektromigreren van gouden nanodraden om hybride apparaten te fabriceren met de supergeleidende legering molybdenum-rhenium (MoRe). Eerst demonstreren we de supergeleidende eigenschappen van het nabijheidseffect in gouden elektrodes met transportmetingen bij lage temperaturen van geëlektromigreerde juncties zonder moleculen. Bij 100 mK meten we een geïnduceerde supergeleidende ‘soft gap’ van 0.7 meV. Deze gap blijft bestaan tot een temperatuur van 4.6 K en een magnetisch veld van 6 T. Verder meten we de transportkarakteristieken bij lage temperaturen van een hybride moleculair apparaat bestaande uit een Fe<sub>4</sub> single-molecule magnet in een nabijheidseffect-geïnduceerde supergeleidende junctie. We zien coëxistentie van Coulomb blokkade en nabijheidseffect-geïnduceerde supergeleiding en bereiken het regime van intermediaire koppeling ( $\Gamma \Delta$ ), wat essentieel is voor het bestuderen van de competitie tussen het Kondo effect en de formatie van Cooper-paren.

Met het tweede platform, beschreven in hoofdstuk 4, onderzoeken we in hoofdstuk 5 hybride moleculaire apparaten van volledig-organische radicaalmoleculen in supergeleidende juncties. Eerst presenteren we transportmetingen waarin we karakteristieke excitaties van spin-geïnduceerde Shiba toestanden zien, die een gevolg zijn van de interactie tussen de ongepaarde spin van het radicaalmolecuul en de sterk-gekoppelde, nabijheidseffect-geïnduceerde supergeleider. Het onderdrukken van de supergeleiding met een magnetisch veld heeft een ‘zero-bias’-piek tot gevolg, wat een indicatie is voor Kondo-‘screening’ van de ongepaarde spin die gekoppeld is aan een normale elektrode. Door de variabele koppeling tussen molecuul en elektrode kunnen we zowel de singlet- als de doublet-grondtoestand van het hybride systeem voorkomen, met bijbehorende doublet- en singlet-Shiba-excitaties, respectievelijk. We onderbouwen de resultaten met berekeningen gebaseerd op het Anderson-model, rekening houdend met de nabijheidseffect-geïnduceerde supergeleidende toestand in de gouden elektrodes.

In het tweede deel van deze scriptie presenteren we experimenten met betrekking tot supergeleiding en een ander materiaalsysteem, namelijk, gelaagde vanderwaals-materialen. In hoofdstuk 6 fabriceren we en bestuderen we de transportkarakteristieken bij lage temperaturen van hybride Josephson-juncties, bestaande uit het gelaagde materiaal MoS<sub>2</sub> en molybdenum rhenium (MoRe). We presenteren waarnemingen van de dikteafhankelijke Josephson-koppeling en van meervoudige Andreev-reflectie (MAR) in verticaal-gestapelde MoS<sub>2</sub> - MoRe Josephson-juncties. Het gebruik van MoRe, een chemisch inerte supergeleider, maakt fabricage van hoog transparante verticale MoS<sub>2</sub> apparaten zonder oxidevorming mogelijk (transparantie tot 80 %). Enkel- en dubbellaagse MoS<sub>2</sub> juncties laten relatief grote kritische stromen (tot 2.5  $\mu$ A) zien, als ook een sub-gap structuur, ten gevolge van MAR. In drie- en vierlaagse apparaten zien we kritieke stromen die ordes van grote lager liggen en kleinere quasiparticle-gaps hebben door de nabijheid van de MoS<sub>2</sub>-lagen op het MoRe.

Hoofdstuk 7 onderzoekt de dikteafhankelijke eigenschappen van de gelaagde materialen 2H-TaS<sub>2</sub>. Eerst presenteren we de transporteigenschappen van elektronische apparaten met 2H-TaS<sub>2</sub>-vlokken van verschillende diktes. We zien dat supergeleiding behouden blijft voor de dunste onderzochte laag (3.5 nm). Interessant genoeg nemen we een duidelijke verhoging van de kritieke temperatuur waar van 0.5 K tot 2.2 K naargelang de laag dunner wordt. We presenteren bandstructuurberekeningen van enkel-laagse TaS<sub>2</sub>-vlokken om de waargenomen verhoging theoretisch te onderzoeken. Door het generaliseren van het Anderson-Morel-model voor een algemene toestandsdichtheid, stellen we dat de verhoging wordt veroorzaakt door een toename in de effectieve elektron-fonon-koppelingsconstante, voor grote Coulomb repulsie.

In het laatste hoofdstuk, 8, bespreken we de resultaten van ieder experiment met aanbevelingen voor verbetering waar nodig, en geven we een overzicht van mogelijke richtingen voor verdere ontwikkelingen.



# ACKNOWLEDGMENTS

I have done my best to remember and thank those who have supported and encouraged me throughout my time in Delft and in pursuing a PhD. Inevitably there are many people and memories that escape me currently while I write this. I could write a book about it all but I will restrict myself to this white space near the end of the thesis.

It is without question that I first acknowledge my thesis advisor and mentor Herre. Thinking back nearly four years ago it was you who first gave me the opportunity to come to Delft and visit the city. It was then my first trip to Europe and after the interview you enthusiastically showed me around the city. It was your kindest and our conversation then that convinced me that the Molecular Electronics and Devices (MED) group would be the right place to pursue my PhD. Your mentoring style is, to say the least, unique, but I always greatly appreciated your straightforwardness and critical analysis of anything I put in front of you. You are always willing to help and act selflessly in the process. I hope to take a piece of your *laissez-faire* approach with me because I'm certain it's the secret to longevity!

My Spanish mentoring *amigos* are next. Andres, I could not have found a better mentor as an aspiring scientist. Your drive and ambition are forces to be reckoned with and qualities that have slowly grown in me. I've witnessed you bound over (tunnel through?) obstacles with the greatest of ease. I thank you for the countless opportunities you offered me throughout the last 3+ years. And more than these things, you are a great friend. It seems you do not only excel at science but your social skills are second to none. I appreciate the many gatherings at your place and coffee breaks and trips to Madrid and the list goes on. Although completely superfluous at this point, I wish you great success in the science and students and postdocs to come!

And to my first mentor Enrique, you made me feel like part of the group from the first day I arrived. You seem devoid of all judgment in the working environment which is a priceless attribute. It allows open discussion of ideas and free development of skills. I appreciate your quick reactions to all my dilution fridge "emergencies" throughout the first years of my PhD. And aside from these, keeping in Spanish fashion, you too have been a great friend. There is a significant portion of Europe that Jade and I would not have been able to visit were it not for you and Enrique looking after Jojo. Thanks for all the Mahjong nights, the coffee breaks, and discussions about books, films, politics, and everything else that came up in our many conversions. Good luck to you and Enrique in Madrid and regardless of your apprehension in securing a position in Spain, I have a feeling you will make something work just fine.

Before I get to the long list of group members and friends, I would like to take a few lines to thank several internal and external collaborators that I have had the pleasure of working with. The group formerly known as MED has been a great place to pursue a PhD. The diversity in the specializations of the PIs in the group has prompted collaborations on several projects. In particular, I would like to thank Teun for all the discussions

of data on my various hybrid devices that I brought to you. There is so much experience wrapped up in your words that several "big picture" ideas were made much clearer to me after a short talk with you. And even with such a broad view of science, you are able to zoom into a detail on a plot and investigate its peculiarities without hesitation. I thank you also for accepting to be on my defense committee and look forward to future discussions. Pieter, Holger, Matvey, and Allard thanks for the short excursion into microwave impedance microscopy and good luck with your future research!

To the Materials of Interest in Renewable Energies (MIRE) group at UAM, Carlos, Isabel, Jose Ares, Jose Clamagirand, and Miriam. Thanks for the great materials! I appreciate all your help during the preparation of our papers and I had a great time visiting the group. Even though we have had limited interaction, you have all been very supportive and encouraging. I wish you all the best of success with the future materials to come! Roberto D'Agosta and Robert Biele, you two always responded with the quickest of speed. I'm grateful for your theoretical expertise and wish you both the best in future calculations. Jose Alvarez, thanks for the collaborations and the short visit in Madrid! Aday, thanks for all the laughs and collaborations! I just have one thing to say to you, I like turtles! Ramon Aguado, we have only begun collaborations but I appreciate our discussions on all sorts of excitations in superconducting hybrids.

The van der Zant lab: Just so many people to thank and so many memories to remember, sorry if I miss someone! Michele, I enjoyed very much our discussions and interactions during my first few years. Thanks for the initial collaborations and introducing me to measurements with light and letting me use your set-up whenever I needed. Things have gone so fast in the last few months, Jade and I have not had time to catch up but I hope to visit you and the new addition to the family before we leave! Max-A-Million! You are one of a kind man, thanks for all the laughs and the good times. You really made the lab environment a fun place to be. Thanks also for being my defense bodyguard! Riccardo, it's been real quiet since you left. I appreciated that you were always ready for a discussion at any time (and in most cases ready to vehemently argue your point) and like Enrique you also made me feel like part of the group from day one. Good luck with all your future activities under the Madrid sun! Mickael, my office mate since the beginning of time. You know I was hoping one day I would get your window desk but you never left! Thanks for the discussions and laughs, good luck with your next steps. Rocco, I very much enjoyed our conversions. You have a great way of discussing physical concepts that draws in people's interest. Best of luck with the end of your PhD! Chris, it was really nice having you in the group for the time you were here. The Jazz fest was a great night and the Back to the Future marathon also comes to mind. I hope your just raking in the big bucks now, looking forward to catching up in California! Julien, for the first year I didn't hear you talk but once you did I heard some of the funniest things ever. You've got a great sense of humor, thanks for all the laughs, good luck with future endeavors. Joeri thanks for your help with my thesis and good luck with your PhD, you're really off to a good start! Venkatesh, you're one of the kindest people I've met. Thanks for the collaboration near the end of your PhD, we still haven't grabbed that coffee but hopefully before I leave. Ronald, the quintessential Dutch person in my mind! Thanks for the laughs and conversations at the coffee table. And to some of the older MED group members, Jos, Harold, Samir, and Ferry, thanks for the conversations and encouragement during



the beginning of my PhD. Warner, Alexandra, Anastasia, Vera, Nandini, Davide, Ignacio thank you all for the daily conversations and interactions, you all made the MED group a fun place to be. To all the support and technical staff of the MED group: Maria, Dorine, and Heleen, thanks for all the years of support. I remember many times wondering into your offices and asking administration questions and you all always responding quickly and were very helpful. Thank you all very much! Mascha and Tino, thanks for the technical support!

The Steele lab: Gary, I have learned many things from you, directly and indirectly. Your exclusion of all social pleasantries for an clear understanding of science is refreshing. You are able to survey a particular interest or project with staggering detail and I hope to approach future projects with the same fervor. I appreciate the "cross-over" BEP and MEP students that you gave me the opportunity to supervise with you. I not only learned new things in each project, I gained valuable supervision experience on how to keep scheduled meetings and deadlines which I will carry with me. I also thank you for accepting to be on my committee. I wish the best for you and the group in the projects to come! Vibhor my office mate for most of my PhD, your patient approach to problems was a great thing to witness. Thanks for always being open to my many questions and patiently responding and discussing ideas. I wish you success and happiness as the leader of your new group. Mingyun, thanks for the dinners and discussions, best of luck to you, Ralf, and Felix in Berlin! Jade and I hope to visit in the future. Sal, you have an amazing way of inserting physics into any conversation and an interesting view of the world. In a conversation, you once described the bunching of defense dates in the summer time as a "BCS density of states" and followed the revelation with a big grin. Just great! Thanks for the discussions and best of luck with your future endeavors! Shun thanks for the conversations and best of luck with the end of your PhD. If you end up back in Japan, let me know, I would love to visit! Nikos, I wish we had had more time to work together. Good luck with your future projects. Daniel and Martijn good luck with your projects!

The Otte lab members: Sander, you are without a doubt the best Sinterklaas I have ever seen, maybe even better than Santa Claus but this is debatable. I enjoyed greatly your instances of on-the-spot wit. Best of luck to you with the group and future projects! Ben and Anna, even now I can't separate your names. You two will forever be "Benanna" in my head! But seriously, Ben, thanks for the dinners and conversations. Your birthday party on the tram in Amsterdam was unforgettable. All the best to you and Hina, hope the position in Nijmegen is going well. Anna, I'll never forget the summer school in Les Houches. We had a great time and those views were amazing! Thanks for all the laughs and Jade and I still need to meet your little guy! Ranko, Jan, and Floris, best of luck with your projects!

The Caviglia lab: Andrea, we did not get an extensive amount of time for interaction but I have enjoyed our short discussions. You have a great way of exciting interest in anything you talk about and your capacity for collaboration and cooperation is a wonderful thing. All the best to you and much success in the future! Emre, thanks for the discussions and laughs. Your bachelor extravaganza in Amsterdam is unforgettable and I've always enjoyed our talks. Thanks for accepting to be my defense bodyguard! You are nearly at the end as well, good luck with your next steps in life and I hope we get a chance to meet again. Dirk, Mafalda, Giordano, and Nicola, best of luck with your projects and

thanks for bringing the “MED lunch” back in style.

The Steeneken lab: Peter thanks for the chats, best of luck in the projects to come! Dejan, you have specifically requested a long acknowledgment. I will see what I can do, thanks for everything, best! Santiago, thanks for the laughs and best of luck with the end of your PhD. Robin, Samer good luck with your research! Just kidding Dejan, really, thanks for all the laughs. You have a great sense of humor that spreads throughout all conversation and even into your science. I very much enjoyed your presentations.

The Groeblacher lab: Simon, we didn't get a chance to interact so much but best of luck with the future projects and growth and development of the group. Richard, once I get tired of the sun in California I will ask you for a picture of the raining sky of Holland. Once you get tired of the rain, I can send you a picture of the sun. Joao and Maarten all the best with your projects and PhDs!

And to the committee members I have not yet mentioned, Yaroslav, Jens, and Nacho, thank you very much for accepting to be on my committee, I'm looking forward to discussions during and after the defense.

Alex, my master's supervisor, thanks again for all the experimental skills you taught me and I brought to Delft. I'm very grateful for your continued support and encouragement not only during my master's but even throughout my PhD and in searching for a postdoc position. It was great to meet last March and that second band we saw really wasn't as good as the first! Thanks for accepting to be on my committee!

And finally, I've come to my family. Thanks Mom for the shining example of a lifetime of learning. You always remind me that we are all students in one way or another and we mostly just move from being a student of *this* to a student of *that*. Terry and Grandma, thanks for the support throughout the years. You both have been strong proponents of my education. To all my family whom I have not seen in nearly 10 years, Ahbe and family, Elizabeth, Fred, I'm coming back! I'm looking forward to some family gatherings and good food! Jade, my wife, you have been a constant and continual source of encouragement and motivation. Thank you for taking such great care of me and for being not only a wonderful wife but a great friend. We've had a good time traveling around Europe and I'm so happy we now get the opportunity to go to a another continent with new things to explore together. And finally, Jojo, my best friend, thanks for meeting me at the top of the stairs everyday for the last 2+ years. You don't care if I've had a good day or a bad day, if it's raining or sunny, you're just a constant ball of happiness and I'm grateful for it!

# CURRICULUM VITÆ

## Joshua Olaf ISLAND

29-09-1981 Born in Jacksonville, Oregon, USA.

### EDUCATION

- 1998–2000 Associate's of Arts and Sciences  
Wenatchee Valley College, Omak, Washington, USA
- 2001–2004 B.Sc. in Computer Science  
Santa Fe University of Art and Design, Sante Fe, New Mexico, USA
- 2004–2008 B.Sc. in Mathematics & Physics  
University of New Mexico, Albuquerque, New Mexico, USA
- 2009–2011 M.Sc. in Physics  
Concordia University, Montreal, Quebec, Canada  
*Thesis:* Few-nanometer electro-mechanical nanotube systems  
*Promotor:* Prof. A.R. Champagne
- 2012–2016 Ph.D. in Physics  
Delft University of Technology, Delft, The Netherlands  
*Thesis:* Quantum transport in superconducting hybrids:  
Molecular devices and layered materials  
*Promotor:* Prof. dr. ir. H.S.J. van der Zant



# LIST OF PUBLICATIONS

29. **J. O. Island**, R. Gaudenzi, J. de Bruijckere, E. Burzuri, C. Franco, M. Mas-Torrent, C. Rovira, J. Veciana, T. M. Klapwijk, R. Aguado, H. S. J. van der Zant, *Proximity-induced Shiba states in a molecular junction*, submitted (2016).
28. N. Papadopoulos, **J. O. Island**, H. S. J. van der Zant, G. A. Steele, *Direct patterning of a field-effect transistor by laser induced  $1T/1T'$  to  $2H$  transition in  $MoS_2$* , submitted (2016).
27. A. J. Molina-Mendoza, E. Giovanelli, W. S. Paz, M. A. Nino, **J. O. Island**, C. Evangeli, L. Aballe, M. Foerster, H. S. J. van der Zant, G. Rubio-Bollinger, N. Agrait, J. J. Palacios, E.M. Perez, A. Castellanos-Gomez, *Franckeite: a naturally occurring van der Waals heterostructure*, submitted (2016).
26. **J. O. Island**, G. A. Steele, H. S. J. van der Zant, A. Castellanos-Gomez, *Thickness dependent interlayer transport in vertical  $MoS_2$  Josephson junctions*, [2D Materials 3, 031002 \(2016\)](#).
25. **J. O. Island**, A. Castellanos-Gomez. *Chapter Seven - Black Phosphorus-Based Nanodevices, In: Francesca Iacopi, John J. Boeckl and Chennupati Jagadish, Editor(s), Semiconductors and Semimetals, Elsevier, 95, 279-303 (2016)*.
24. A. J. Molina-Mendoza, J. L. Lado, **J. O. Island**, M. A. Nino, L. Aballe, M. Foerster, F. Y. Bruno, H. S. J. van der Zant, G. Rubio-Bollinger, N. Agrait, E. Perez, J. Fernandez-Rossier, A. Castellanos-Gomez, *Centimeter-scale synthesis of ultrathin layered  $MoO_3$  by van der Waals epitaxy*, [Chemistry of Materials 28, 4042-4051 \(2016\)](#).
23. P. J. de Visser, R. Chua, **J. O. Island**, M. Finkel, A. J. Katan, H. Thierschmann, H. S. J. van der Zant, T. M. Klapwijk, *Spatial conductivity mapping of unprotected and capped black phosphorus using microwave microscopy*, [2D Materials 3, 021002 \(2016\)](#).
22. E. Navarro-Moratalla\*, **J. O. Island**\*, S. Manas-Valero, E. Pinilla-Cienfuegos, A. Castellanos-Gomez, J. Queda, G. Rubio-Bollinger, L. Chirolli, J. A. Silva-Guilln, N. Agrait, G. A. Steele, F. Guinea, H. S. J. van der Zant, E. Coronado, *Enhanced superconductivity in atomically thin  $TaS_2$* , [Nature Communications 15, 7853 \(2016\)](#).
21. **J. O. Island**, R. Biele, M. Barawi, J. M. Clamagirand, J. R. Ares, C. Sanchez, H. S. J. van der Zant, I. J. Ferrer, R. D'Agosta, A. Castellanos-Gomez, *Titanium trisulfide ( $TiS_3$ ): a 2D semiconductor with quasi-1D optical and electronic properties*, [Scientific Reports 6, 22214 \(2016\)](#).
20. E. Burzuri, **J. O. Island**\*, R. Diaz-Torres\*, A. Fursina, A. Gonzalez-Campo, O. Roubeau, S. J. Teat, N. Aliaga-Alcalde, E. Ruiz, H. S. J. van der Zant, *Sequential electron transport and vibrational excitations in an organic molecule coupled to few-layer graphene electrodes*, [ACS Nano 12, 2521 \(2016\)](#).
19. **J. O. Island**, A. Kuc, E. H. Diependaal, H. S. J. van der Zant, T. Heine, A. Castellanos-Gomez, *Precise and reversible band gap tuning in single-layer  $MoSe_2$  by uniaxial strain*, [Nanoscale 8, 2589 \(2016\)](#).

18. **J. O. Island\***, S. I. Blanter\*, M. Buscema, H. S. J. van der Zant, A. Castellanos-Gomez, *Gate controlled photocurrent generation mechanisms in high-gain  $\text{In}_2\text{Se}_3$  phototransistors*, [Nano Letters](#) **15**, 7853 (2015).
17. A. S. Pawbake, **J. O. Island**, E. Flores, J. R. Ares, C. Sanchez, I. J. Ferrer, S. R. Jadhkar, H. S. J. van der Zant, A. Castellanos-Gomez, D. J. Late, *Temperature-dependent Raman spectroscopy of titanium trisulfide ( $\text{TiS}_3$ ) nanoribbons and nanosheets*, [ACS Applied Materials & Interfaces](#) **7**, 24185 (2015).
16. R. S. Velez, D. Ciudad, **J. O. Island**, M. Buscema, O. Txoperena, S. Parui, G. A. Steele, F. Casanova, H. S. J. van der Zant, A. Castellanos-Gomez, L. E. Hueso, *Gate-tunable diode and photovoltaic effect in an organic-2D layered material p-n junction*, [Nanoscale](#) **7**, 15442 (2015).
15. R. Gaudenzi\*, **J. O. Island\***, J. De Bruijkere, E. Burzuri, T. M. Klapwijk, H. S. J. van der Zant, *Superconducting molybdenum-rhenium electrodes for single molecule transport studies*, [Applied Physics Letters](#) **106**, 222602 (2015).
14. M. Buscema, **J. O. Island**, D. J. Groenendijk, S. I. Blanter, G. A. Steele, H. S. J. van der Zant, A. Castellanos-Gomez, *Photocurrent generation with two dimensional van der Waals semiconductors*, [Chemical Society Reviews](#) **44**, 3691 (2015).
13. **J. O. Island**, M. Barawi, R. Biele, A. Almazan, J. M. Clamagirand, J. R. Ares, C. Sanchez, H. S. J. van der Zant, J. V. Alvarez, R. D'Agosta, et al.,  *$\text{TiS}_3$  transistors with tailored morphology and electrical properties*, [Advanced Materials](#) **27**, 2595 (2015).
12. V. Seshan\*, **J. O. Island\***, R. van Leeuwen, W. J Venstra, B. H. Schneider, S. D. Janssens, K. Haenen, E. J. R. Sudholter, L. C. P. M. de Smet, H. S. J. van der Zant, G. A. Steele, A. Castellanos-Gomez *Pick-up and drop transfer of diamond nanosheets*, [Nanotechnology](#) **26**, 125706 (2015).
11. **J. O. Island**, G. A. Steele, H. S. J. van der Zant, A. Castellanos-Gomez, *Mechanical manipulation and exfoliation of boron nitride flakes by micro-plowing with an AFM tip*, [ScienceJet](#) **4**, 163 (2015).
10. **J. O. Island**, G. A. Steele, H. S. J. van der Zant, A. Castellanos-Gomez, *Environmental instability of few-layer black phosphorus*, [2D Materials](#) **2**, 011002 (2015).
9. V. Tayari, A. C. McRae, S. Yigen, **J. O. Island**, J. M. Porter, A. R. Champagne, *Tailoring 10 nm scale suspended graphene junctions and quantum dots*, [Nano Letters](#) **15**, 114 (2014).
8. **J. O. Island**, A. Holovchenko, M. Koole, P. F. A. Alkemade, M. Menelaou, N. Aliaga-Alcalde, E. Burzuri, H. S. J. van der Zant, *Fabrication of hybrid molecular devices using multi-layer graphene break junctions*, [Journal of Physics: Condensed Matter](#) **26**, 474205 (2014).
7. A. Castellanos-Gomez, L. Vicarelli, E. Prada, **J. O. Island**, K. L. Narasimha-Acharya, S. I. Blanter, D. J. Groenendijk, M. Buscema, G. A. Steele, J. V. Alvarez, et al., *Isolation and characterization of few-layer black phosphorus*, [2D Materials](#) **1**, 025001 (2014).
6. **J. O. Island**, M. Buscema, M. Barawi, J. M. Clamagirand, J. R. Ares, C. Sanchez, I. J. Ferrer, G. A. Steele, H. S. J. van der Zant, A. Castellanos-Gomez, *Ultrahigh photoresponse of few-layer  $\text{TiS}_3$  nanoribbon transistors*, [Advanced Optical Materials](#) **2**, 641 (2014).

5. A. J. Molina-Mendoza, J. G. Rodrigo, **J. O. Island**, E. Burzuri, G. Rubio-Bollinger, H. S. J. van der Zant, N. Agrait, *Note: Long-range scanning tunneling microscope for the study of nanostructures on insulating substrates*, [Review of Scientific Instruments](#) **85**, 026105 (2014).
4. S. Yigen, V. Tayari, **J. O. Island**, J. M. Porter, A. R. Champagne, *Electronic thermal conductivity measurements in intrinsic graphene*, [Physical Review B](#) **87**, 241411 (2013).
3. **J. O. Island**, V. Tayari, A. C. McRae, A. R. Champagne, *Few-hundred Ghz carbon nanotube nanoelectromechanical systems (NEMS)*, [Nano Letters](#) **12**, 4564 (2012).
2. **J. O. Island**, V. Tayari, S. Yigen, A. C. McRae, A. R. Champagne, *Ultra-short suspended single-wall carbon nanotube transistors*, [Applied Physics Letters](#) **99**, 243106 (2011).
1. **J. O. Island**, *Few-Nanometer Electro-Mechanical Nanotube Systems*, [Dissertation, Concordia University](#), (2011).